

© 2024 Samuel Frederick

IDEALIZED PARTICLE-RESOLVED LARGE-EDDY SIMULATIONS  
TO EVALUATE THE IMPACT OF EMISSIONS SPATIAL HETEROGENEITY  
ON CCN ACTIVITY

BY

SAMUEL FREDERICK

THESIS

Submitted in partial fulfillment of the requirements  
for the degree of Master of Science in Climate, Meteorology, and Atmospheric Sciences  
in the Graduate College of the  
University of Illinois Urbana-Champaign, 2024

Urbana, Illinois

Master's Committee:

Professor Nicole Riemer  
Professor Matthew West  
Professor Larry Di Girolamo

# Abstract

Aerosol-cloud interactions remain a large source of uncertainty in climate models due to complex, nonlinear processes that alter aerosol properties and the inability to represent the full compositional complexity of aerosol populations within large-scale modeling frameworks. The spatial resolution of these models (typically 10-100 km) is often coarser than the spatially varying emissions in the modeled geographic region. This results in diffuse, uniform emission of primary aerosol and gas-phase species instead of spatially heterogeneous concentrations. Aerosol processes such as gas-particle partitioning and coagulation are concentration-dependent, and thus the representation of spatially heterogeneous emissions impacts aerosol aging and properties. This includes climate-relevant quantities like particle hygroscopicity and cloud condensation nuclei (CCN) activity.

This thesis investigates the impact of emissions spatial heterogeneity on CCN activity by using the particle-resolved model PartMC coupled to the Weather Research and Forecasting model configured for large-eddy simulations (LES). The resulting modeling framework resolves turbulence-chemistry interactions and aerosol aging on a per-particle scale. The sensitivity of CCN activity to emissions spatial heterogeneity is evaluated for primary aerosol and gas-phase emissions typical of urban regions. The pattern of emissions is varied to investigate a range of spatial heterogeneity scenarios. For each scenario, CCN activity is compared against a uniform emissions base case to determine the impact of spatially heterogeneous emissions.

**TODO: update!** We find that CCN concentrations decrease by as much as 10% with increasing emissions spatial heterogeneity, especially for low supersaturations ( $S=0.1, 0.3\%$ ). This work is a first of a kind application of high resolution, particle-resolved LES for quantifying structural uncertainty of CCN activity due to the representation of emissions spatial heterogeneity.

# **Acknowledgments**

# Table of contents

<b>List of Tables</b> . . . . .	<b>vi</b>
<b>List of Figures</b> . . . . .	<b>vii</b>
<b>Chapter 1 Introduction</b> . . . . .	<b>1</b>
1.1 The complexity of atmospheric aerosols . . . . .	1
1.1.1 Particle size . . . . .	1
1.1.2 Production and removal mechanisms . . . . .	2
1.1.3 Aerosol compositional diversity . . . . .	2
1.1.4 Impacts of aerosols on climate . . . . .	3
1.2 Spatial heterogeneity in the atmosphere and its impact on aerosols . . . . .	4
1.2.1 Coupling between surface heterogeneities and atmospheric state . . . . .	4
1.2.2 Coupling between emissions spatial heterogeneity and aerosol processes . . . . .	5
1.2.3 Sub-grid scale variability of aerosols . . . . .	6
1.2.4 Modeling approaches and parameterizations for emissions sub-grid scale variability .	9
1.3 Representation of aerosols across modeling frameworks . . . . .	11
1.3.1 Aerosol modeling treatments . . . . .	11
1.3.2 Joint aerosol-transport models . . . . .	14
1.4 Objectives of this thesis . . . . .	15
<b>Chapter 2 Quantifying emissions spatial heterogeneity and mixing</b> . . . . .	<b>17</b>
2.1 Existing approaches to quantifying spatial heterogeneity . . . . .	17
2.1.1 Spatial autocorrelation and semivariograms . . . . .	18
2.1.2 Fractal dimensions . . . . .	18
2.1.3 Lacunarity . . . . .	18
2.1.4 Information entropy based metrics . . . . .	19
2.1.5 Nearest neighbor statistics for point-based heterogeneity . . . . .	19
2.1.6 Multiscale norms . . . . .	20
2.2 Metrics for quantifying the mixing of reactive compounds . . . . .	20
2.2.1 Segregation intensity . . . . .	20
2.2.2 Damköhler number . . . . .	21
2.3 A novel approach to quantifying spatial heterogeneity . . . . .	23
2.3.1 Metric definition . . . . .	23
2.3.2 Computational methods for computing the spatial heterogeneity metric . . . . .	25
2.3.3 Example calculations for emission patterns . . . . .	28
<b>Chapter 3 Modeling tools</b> . . . . .	<b>30</b>
3.1 Large-eddy simulations . . . . .	30
3.1.1 Sub-grid scale parameterizations . . . . .	31
3.1.2 Computational domain . . . . .	32
3.1.3 Meteorological Initial Conditions . . . . .	33
3.1.4 Simulation spin-up . . . . .	34
3.2 Gas phase simulations . . . . .	35

3.2.1	Chemical mechanism . . . . .	35
3.2.2	Initial conditions and emissions . . . . .	36
3.3	Multiphase simulations . . . . .	37
3.3.1	Chemical mechanism . . . . .	37
3.3.2	Aerosol representation . . . . .	37
3.3.3	Initial conditions and emissions . . . . .	38
<b>Chapter 4</b>	<b>Impacts of emissions spatial heterogeneity on gas-phase reactions</b> . . . . .	<b>41</b>
4.1	Simulated emissions scenarios . . . . .	41
4.2	Results . . . . .	42
4.2.1	Ozone cross sections . . . . .	43
4.2.2	Spatio-temporal trends in ozone and its precursors . . . . .	45
4.2.3	Spatial heterogeneity in the atmosphere of ozone and its precursors . . . . .	48
4.3	Discussion . . . . .	51
<b>Chapter 5</b>	<b>Impacts of emissions spatial heterogeneity on aerosol properties and CCN activity</b> .	<b>54</b>
5.1	Idealized coagulation simulations . . . . .	54
5.1.1	Simulation scenarios . . . . .	54
5.1.2	Results . . . . .	55
5.2	Full multiphase simulations . . . . .	58
5.2.1	Simulated emissions scenarios . . . . .	59
5.2.2	Aerosol size distributions . . . . .	59
5.2.3	Aerosol composition . . . . .	62
5.2.4	Aerosol mixing state . . . . .	72
5.2.5	Impacts of emissions <i>SH</i> on CCN activity . . . . .	75
5.2.6	Influence of ammonia on aerosol composition and CCN activity . . . . .	80
5.3	Implications . . . . .	83
<b>Chapter 6</b>	<b>Conclusions</b> . . . . .	<b>84</b>
6.1	Study limitations and future work . . . . .	84
<b>References</b>		<b>85</b>

# List of Tables

3.1	Gas phase emissions and initial conditions. Table adapted from N. Riemer, M. West, et al. 2009 with permission.	36
3.2	Aerosol emissions and initial conditions. Table adapted from N. Riemer, M. West, et al. 2009 with permission.	39
5.1	Aerosol species and associated hygroscopicities in WRF-PartMC	68

# List of Figures

1.1	Cartoon representations of aerosol modeling treatments, each for the same aerosol population. The following representations are shown: (a) Bulk, (b) Modal, (c) 1-D sectional, (d) Particle-resolved. . . . .	12
1.2	Use of WRF-PartMC-LES as a benchmark against coarser resolved aerosol-transport models for quantifying structural uncertainty in aerosol properties. . . . .	16
2.1	Dependence of the Damköhler number on turbulent and reactive timescales. Figure adapted from Kotamarthi and Feng 2017 . . . . .	22
2.2	Example subsets for $SH$ calculation. (a) Full domain mean. (b-f) Examples of rectangular subsets (highlighted regions) over which the subset mean is computed. . . . .	24
2.3	CPU time for the naive looping $SH$ Fortran subroutine. The x-axis indicates the total number of domain grid cells (elements) in the array passed to the subroutine. A power law regression is plotted as the red dashed line. . . . .	25
2.4	CPU time for the Monte Carlo $SH$ Fortran subroutine. The x-axis indicates the number of domain subsets that are randomly selected to determine the $SH$ estimate. A power law regression is plotted as the red dashed line. . . . .	26
2.5	$SH$ estimate in blue for the Monte Carlo sampling subroutine vs. the number of randomly selected domain subsets (top panel). The true value of $SH$ computed via the naive algorithm is shown as the black line. Absolute relative error between $SH$ estimate and the true value of $SH$ (middle panel). Bias between $SH$ estimate and the true value of $SH$ (bottom panel) . . . . .	27
2.6	Example emission patterns arranged from least heterogeneous (“Uniform Base Case”) to most heterogeneous (“Scenario 5”). For each pattern, the spatial heterogeneity $SH$ is listed alongside the domain mean ( $\bar{f}(S)$ ) and variance ( $\sigma^2$ ). The color of each scenario indicates the emission scaling relative to the uniform base case with red being the highest scaling.) . . . . .	28
3.1	Idealized atmospheric sounding used for domain meteorological initial conditions. Initial conditions for potential temperature (left) and specific humidity (right). . . . .	33
3.2	Resolved-scale vertical heat flux profiles (left) and TKE at intervals of 10 minutes during the first hour of simulation spin-up. . . . .	34
3.3	Aerosol initial condition size distributions. . . . .	40
3.4	Aerosol emission size distributions. . . . .	40
4.1	Emissions scenarios for ozone production simulations. The spatial heterogeneity of each emission scenario is listed in the lower portion of each scenario alongside domain mean and variance. . . . .	42
4.2	Ozone cross sections in the x-y plane at 2 hour intervals in the middle of the PBL ( $z \sim 500$ m) for the uniform base case. . . . .	43
4.3	Ozone cross sections in the x-y plane at 2 hour intervals in the middle of the PBL ( $z \sim 500$ m) for emissions scenario 1. . . . .	44
4.4	Ozone cross sections in the x-y plane at 2 hour intervals in the middle of the PBL ( $z \sim 500$ m) for emissions scenario 2. . . . .	44

4.5	Ozone cross sections in the x-y plane at 2 hour intervals in the middle of the PBL ( $z \sim 500$ m) for emissions scenario 3. . . . .	44
4.6	Vertical profiles at $t = 6$ h for ozone, NO <sub>2</sub> , and HCHO (left to right) for each emissions scenario. Each vertical profile indicates the species mean concentration when horizontally averaged at each vertical level. . . . .	45
4.7	Ozone concentration time-height plots for each emissions scenario. . . . .	46
4.8	Time-height plots of ozone percent difference for each emissions scenario. . . . .	48
4.9	Time-height plot of field $SH$ for O <sub>3</sub> , NO <sub>x</sub> , and HCHO in the uniform base case. $SH$ value contours are shown in grayscale for each subplot. . . . .	49
4.10	Time-height plot of field $SH$ for O <sub>3</sub> , NO <sub>x</sub> , and HCHO in emissions scenario 1. $SH$ value contours are shown in grayscale for each subplot. . . . .	50
4.11	Time-height plot of field $SH$ for O <sub>3</sub> , NO <sub>x</sub> , and HCHO in emissions scenario 2. $SH$ value contours are shown in grayscale for each subplot. . . . .	51
4.12	Time-height plot of field $SH$ for O <sub>3</sub> , NO <sub>x</sub> , and HCHO in emissions scenario 3. $SH$ value contours are shown in grayscale for each subplot. . . . .	52
5.1	$SH$ scenarios for ideal coagulation simulations. . . . .	55
5.2	Total number concentration for each $SH$ scenario normalized by the initial condition total number concentration. Lines indicate normalized number concentration averaged over each vertical level in the domain. (a) Uniform base case. (b–f) Scenarios 1–5 . . . . .	56
5.3	Time required in minutes for the total number concentration in the lowest 200 m of the PBL to be reduced to 75% of the initial value vs. scenario $SH$ . “S0” is the uniform base case, with all other scenarios labeled S1–S5. . . . .	57
5.4	Emissions scenarios for multiphase chemistry simulations. The spatial heterogeneity of each emission scenario is listed in the lower portion of each scenario alongside domain mean and variance. . . . .	58
5.5	Aerosol number distribution plots for each emissions scenario. The distribution initial condition (light blue) is shown alongside the distribution at the end of each simulation ( $t = 6$ h). Scenarios are labeled as the following: (a) uniform base case, (b) scenario 1, (c) scenario 2, (d) scenario 3. . . . .	60
5.6	Aerosol mass distribution plots for each emissions scenario. The distribution initial condition (light blue) is shown alongside the distribution at the end of each simulation ( $t = 6$ h). Scenarios are labeled as the following: (a) uniform base case, (b) scenario 1, (c) scenario 2, (d) scenario 3. . . . .	61
5.7	Time-height plots for aerosol sulfate across each emissions scenario. Isopleths indicate sulfate mixing ratio in ppbv ranging from 3.5–4.75 ppbv. . . . .	63
5.8	Time-height plots for aerosol ammonium across each emissions scenario. Isopleths indicate ammonium mixing ratio in ppbv ranging from 1.3–2.1 ppbv. . . . .	64
5.9	Time-height plots for aerosol nitrate across each emissions scenario. Isopleths indicate nitrate mixing ratio in ppbv ranging from $10^{-3}$ to $10^0$ ppbv. . . . .	65
5.10	Vertical profiles of aerosol ammonia, nitrate, and sulfate at $t = 6$ h. . . . .	65
5.11	Size-resolved mass fraction for the uniform base case at regular 2-hour intervals. . . . .	67
5.12	Size-resolved mass fraction for emissions scenario 3 at regular 2-hour intervals showing species mass fraction as a percent of total aerosol mass vs. particle diameter. . . . .	69
5.13	2-dimensional number distributions $n(D_p, \kappa)$ at regular two-hour intervals for the uniform base case. . . . .	70
5.14	2-dimensional number distributions $n(D_p, \kappa)$ at regular two-hour intervals for scenario 3. . .	71

5.15 Two idealized cases for aerosol populations composed of ammonium sulfate (blue) and organic carbon (beige). Case 1 is fully internally mixed while case 2 is fully externally mixed, yet each case contains the same bulk concentration of each species. . . . .	72
5.16 Vertical profiles for mixing state $\chi$ and diversity measures $D_\alpha$ and $D_\gamma$ for each emissions scenario at $t = 6$ h. . . . .	73
5.17 . . . . .	74
5.18 Vertical profiles ( $t = 6$ h) for each emission scenario of CCN activating at supersaturations $S = 0.1, 0.3, 0.6, 1.0\%$ . . . . .	76
5.19 Time-height plots for the percent difference between CCN concentrations in the uniform base case and scenario 1 for each supersaturation level. Red indicates an increase in CCN relative to the base case while blue indicates a decrease. Isopleths indicate lines of constant percent difference in increments of 5%. . . . .	77
5.20 Time-height plots for the percent difference between CCN concentrations in the uniform base case and scenario 2 for each supersaturation level. Red indicates an increase in CCN relative to the base case while blue indicates a decrease. Isopleths indicate lines of constant percent difference in increments of 5%. . . . .	79
5.21 Time-height plots for the percent difference between CCN concentrations in the uniform base case and scenario 3 for each supersaturation level. Red indicates an increase in CCN relative to the base case while blue indicates a decrease. Isopleths indicate lines of constant percent difference in increments of 5%. . . . .	80
5.22 Vertical profiles ( $t = 6$ h) for ammonium, nitrate, and sulfate comparing uniform base case and scenario 3 both with and without ammonium. . . . .	81
5.23 Vertical profiles ( $t = 6$ h) for CCN concentrations at supersaturations $S = 0.1, 0.3, 0.6, 1.0\%$ for the uniform base case and scenario 3 with and without ammonium. . . . .	82

# **Chapter 1**

## **Introduction**

This chapter discusses key background motivating this thesis, including fundamental properties of aerosols, their feedbacks on the climate, and the role of emissions spatial heterogeneity in altering the aerosol state. A description of the coupling between emissions spatial heterogeneity and aerosol processes is provided, and a brief review of current efforts to quantify and parameterize the sub-grid scale variability of aerosols is presented. Subsequently, the representation of aerosols in modeling frameworks is discussed and the current state of high-resolution joint aerosol-transport models capable of resolving emissions spatial heterogeneity is reviewed. Finally, existing gaps in the literature are outlined and objectives are presented to answer primary avenues of inquiry in this thesis.

### **1.1 The complexity of atmospheric aerosols**

An aerosol is a collection of particles composed of one or more chemical species that are suspended in a fluid or gas. In the atmosphere, aerosol particles vary considerably in terms of their physical properties such as size, composition, and origin. Additionally, the chemical, thermodynamic, and radiative properties of aerosol particles can alter the state of the aerosol and the surrounding environment through numerous feedback mechanisms. In turn, aerosol particles exhibit a complex, non-linear coupling with the environment that spans broad spatial and temporal scales.

#### **1.1.1 Particle size**

Aerosol particles are typically measured by their diameter where spherical morphology is assumed. The smallest particles have diameters on the order of 1 nm and are produced via the nucleation of low-volatility vapors. On the opposite extreme of particle sizes, the largest particle diameters can exceed 100  $\mu\text{m}$ . In total, aerosols span approximately five orders of magnitude (Seinfeld and Pandis 1998). To capture the broad

scale of particle diameters that may be present in a population of aerosol particles, aerosol size distributions often represent the number concentration of particles as a function of the logarithm of particle diameter. The particle size distribution may be represented by multiple modes—lognormal size distributions—that are differentiated by the characteristics of particles within each mode, including growth and removal mechanisms. Typically, three distinct modes are present in a particle size distribution: the nucleation, accumulation, and coarse mode.

### **1.1.2 Production and removal mechanisms**

Nucleation mode particles are up to 20 nm in diameter and undergo rapid growth as gas-phase species condense onto the particle surface or as particles inelastically collide through coagulation. They are removed from the nucleation mode by growth into the accumulation mode, which spans particle diameters from 0.1  $\mu\text{m}$  to 2  $\mu\text{m}$ . In addition to particles that enter the accumulation mode through growth by condensation or coagulation, particles may be released directly into the accumulation mode via primary emissions. Removal mechanisms such as wet and dry deposition are least efficient in the accumulation mode, allowing particles to remain suspended in the atmosphere for days to weeks. Particles in the coarse mode have diameters exceeding 2  $\mu\text{m}$  and are produced by mechanical processes such as abrasion and the resuspension of dust. Due to their size, particles in the coarse mode are rapidly removed by gravitational settling within minutes to hours (Seinfeld and Pandis 1998). This multi-modal description of the aerosol size distribution points to the inherent complexity of aerosol population dynamics—production, growth, and removal mechanisms differ considerably by particle size.

### **1.1.3 Aerosol compositional diversity**

As noted, production mechanisms vary across aerosol modes (e.g., nucleation of low-volatility vapors, emission of primary aerosol into the accumulation mode, resuspension of coarse particles, etc.). These processes involve numerous chemical species. For example, whereas volatile organic compounds (VOCs) such as isoprene and other organic carbon (OC) species may undergo oxidation reactions which lower their volatility and promote particle nucleation, particles released directly into the accumulation or coarse mode as primary aerosol may consist of either organics that are produced during combustion such as black carbon (BC) or inorganics such as sea salt spray and mineral dust. Furthermore, gas-particle partitioning allows inorganic gas phase species such as  $\text{H}_2\text{SO}_4$ ,  $\text{HNO}_3$ , and  $\text{NH}_3$  to enter the aerosol phase. Both the release of

primary aerosol and the partitioning of compounds into the aerosol phase via gas-particle partitioning alter the properties of the aerosol population including hygroscopicity and optical properties which are key to the feedbacks between aerosols and climate.

#### 1.1.4 Impacts of aerosols on climate

Aerosols alter the Earth's radiative budget directly through scattering and absorption of shortwave (solar) radiation. The scattering of solar radiation by aerosols back out to space increases planetary albedo, thereby decreasing the intensity of radiation reaching the Earth's surface (Charlson and Pilat 1969; Charlson, Schwartz, et al. 1992). As a result, scattering generally contributes a net cooling effect. The intensity of scattering depends on the composition of the aerosol, with strongly-scattering species including sulfate and nitrate. Aerosols may also absorb broadband radiation, re-emitting in the form of thermal radiation that results in a net warming effect. Absorption varies by aerosol species; strongly absorbing species include carbonaceous aerosol such as black carbon and elemental carbon. Scattering and absorption of solar radiation due to aerosols alters the stability of the atmosphere due to changes in the vertical profile of temperature (J. Li et al. 2022; Lau and K.-M. Kim 2006).

In addition to direct aerosol-radiative effects, aerosols also alter the climate through indirect effects with clouds commonly referred to as aerosol-cloud interactions. Hygroscopic aerosol particles act as cloud condensation nuclei (CCN), thereby allowing water vapor to condense onto their surface at ambient supersaturations  $S$  typical of the troposphere ( $S \lesssim 1\%$ ). Twomey 1977 was the first to note that higher concentrations of CCN result in a greater abundance of small cloud droplets. This in turn leads to an increase in cloud albedo, causing greater reflection of solar radiation back to space and thus a net cooling effect on climate. In addition to the Twomey effect, the impact of aerosol number concentration on droplet size can delay or prevent the onset of collision-coalescence necessary to initiate precipitation. This effect was first discovered by Albrecht 1989 and enhances the lifetime of clouds, thereby prolonging the reflection of solar radiation.

The global mean effective radiative forcing (ERF) due to the combination of direct and indirect effects is estimated by the Intergovernmental Panel on Climate Change (IPCC) to be in the range of  $-2.0$  to  $-0.6 \text{ W m}^{-2}$  within 95% confidence, with a mean of  $-1.3 \text{ W m}^{-2}$  (Forster et al. 2021). Separating the ERF into forcing due to aerosol-cloud interactions and direct radiative forcing, aerosol-cloud interactions contribute the largest magnitude of forcing in the range  $-1.7$  to  $-0.3 \text{ W m}^{-2}$  with a mean of  $-1.0 \text{ W m}^{-2}$ . Direct effects contribute

$-0.6$  to  $0.0 \text{ W m}^{-2}$  with a mean of  $-0.3 \text{ W m}^{-2}$ .

The magnitude of uncertainty in ERF due to aerosol direct and indirect effects remains large due to a host of factors. As discussed in Section 1.1, aerosol particle size and composition are highly varied and determine climate-relevant properties including a particle's scattering and absorption coefficients and its hygroscopicity. Representing the full range of aerosol composition and properties in a modeling framework is highly computationally expensive and current state-of-the-science global scale climate models use simplified aerosol treatments such as sectional or modal models (aerosol model treatments are discussed in more detail in Section 1.3). Furthermore, estimates for ERF due to aerosol-cloud interactions in particular are poorly constrained due to limited understanding of the coupling between microphysical phenomena and cloud macrophysical structure for deep convective clouds where phase transitions complicate the role of aerosols and thermodynamic feedbacks (Fan et al. 2016). In addition, aerosols are highly spatially heterogeneous due to localized sources, resulting in varied concentrations and properties that determine the local activity of CCN and associated aerosol-cloud interactions.

## 1.2 Spatial heterogeneity in the atmosphere and its impact on aerosols

### 1.2.1 Coupling between surface heterogeneities and atmospheric state

There exists a well established link between surface spatial heterogeneities and their impacts on the evolution of the atmospheric state. For instance, Jerome D. Fast, Berg, et al. 2019 conducted a joint observation and modeling study to evaluate the role of soil moisture heterogeneity in promoting deeply convecting clouds. The authors compared observations collected during the Holistic Interactions of Shallow Clouds, Aerosols, and Land-Ecosystems (HI-SCALE) campaign against a set of large-eddy simulations (LES) where the spatial heterogeneity of soil moisture was varied from a constant distribution to higher variability which closely matched the observed soil moisture spatial heterogeneity. The authors found that under modeling scenarios with smoothly varying soil moisture, clouds did not develop into open cell, deep convective cumulus capable of precipitating and instead were characterized by shallow, uniform non-precipitating clouds. In order to replicate the degree of cloud heterogeneity and the development of deeply convecting clouds observed during the HI-SCALE campaign, realistic spatial variability in the modeled soil moisture distribution was required.

In addition to soil moisture fluxes, spatial heterogeneity in surface heat fluxes has been shown to be critical to the development of atmospheric circulation. Lee, Zhang, and Klein 2019 conducted an idealized

LES study in which surface heat fluxes (including both sensible and latent heat flux) were prescribed by checkerboard patterns of ranging spatial heterogeneity (most heterogeneous being the lowest frequency checkerboard pattern with the largest pattern length scale, and the least heterogeneous being the highest frequency patterns with the smallest pattern length scale). The authors found that secondary circulation developed under scenarios with the highest spatial heterogeneity and minimal background winds (less than 2 m s<sup>-1</sup>). This circulation was responsible for transporting moisture from checkerboard regions with greater latent heat flux to drier regions with lesser latent heat flux.

### 1.2.2 Coupling between emissions spatial heterogeneity and aerosol processes

The spatial distribution of primary aerosol emissions and precursor gas phase emissions results in spatially varying concentrations that span orders of magnitude and complex variability in the composition of aerosols. For example, urban aerosol number concentrations are highly variable; whereas a significant number of nucleation mode particles ( $\sim 10^5$ – $10^6$  cm<sup>-3</sup>) may be found nearby busy highways, the concentration of nucleation mode particles is significantly reduced downwind of the highway due in large part to coagulation (Zhu et al. 2002). By comparison, rural aerosol concentrations are more spatially uniform and lower in number with concentrations ranging between  $\sim 10^3$ – $10^4$  cm<sup>-3</sup>. Whereas urban aerosol are composed of a mixture of primary carbonaceous aerosol released from vehicular and industrial combustion and species resulting from gas-particle partitioning of emitted gas phase compounds such as NO<sub>x</sub> or SO<sub>2</sub>, rural aerosol contain a large fraction of organics resulting from the oxidation of biogenic volatile organic compounds (BVOCs) in the gas phase to form secondary organic aerosol (SOA). In rural regions containing significant amounts of agricultural land use, ammonium may also be present in elevated fractions (Seinfeld and Pandis 1998).

The spatial heterogeneity of both gas phase and aerosol number concentrations impacts how particles age due to concentration dependent processes such as coagulation and gas-particle partitioning. For a number distribution  $n(v, t)$  that is a function of particle volume  $v$  and time  $t$ , the rate of change to the number distribution due to coagulation is defined as

$$\frac{\partial n(v, t)}{\partial t} = \frac{1}{2} \int_0^v K(v - v', v') n(v - v', t) n(v', t) dv' - n(v, t) \int_0^\infty K(v', v) n(v', t) dv', \quad (1.1)$$

where  $K(v_1, v_2)$  is the coagulation kernel between particles of volume  $v_1$  and  $v_2$ . The first term on the right

hand side of Equation 1.1 is coagulation gain while the second term is coagulation loss. Note how each term is proportional to the square of the number distribution. This causes the rate of coagulation to be highly sensitive to changes in aerosol number concentration, whereby highly polluted regions (such as nearby highway emissions) experience elevated rates of coagulation.

In addition to coagulation, the rate of chemical reactions in both the gas phase and gas-particle partitioning are concentration dependent and thus the spatial heterogeneity of emitted compounds determines the effective rate at which such reactions proceed. An extensive body of literature evaluates the effects of chemical segregation (i.e., the degree to which precursor compounds are spatially separated or collocated) on the abundance of reaction products in the atmospheric boundary layer (Schumann 1989; Sykes, Parker, et al. 1994; Molemaker and J. V.-G. d. Arellano 1998; Krol, Molemaker, and J. V. G. d. Arellano 2000; Jean-François Vinuesa and J. V.-G. D. Arellano 2003; Auger and Legras 2007; Pugh et al. 2011; Ouwersloot et al. 2011; Dlugi et al. 2014; S.-W. Kim, Barth, and Trainer 2016; C. W. Y. Li et al. 2021; Y. Wang, Brasseur, and T. Wang 2022). All of these studies focus on second order gas phase reactions which are prevalent in atmospheric chemistry and utilize LES to resolve turbulence-chemistry interactions. Initial studies focused on generic species and a range of imposed reaction rates (Schumann 1989; Sykes, Parker, et al. 1994; Molemaker and J. V.-G. d. Arellano 1998). Subsequently, modeling studies have investigated the production and destruction of ozone and oxidation of generic VOCs (Krol, Molemaker, and J. V. G. d. Arellano 2000; Auger and Legras 2007) and more recently oxidation of isoprene by OH (Pugh et al. 2011; Ouwersloot et al. 2011; Dlugi et al. 2014; S.-W. Kim, Barth, and Trainer 2016). Advances in computing have allowed the use of direct numerical simulations of gas phase reactions in the planetary boundary layer (C. W. Y. Li et al. 2021) and the modeling of entire urban regions with LES to evaluate chemical segregation (Y. Wang, Brasseur, and T. Wang 2022). Note that these studies do not model aerosols, however the coupling between the gas phase and aerosols through gas-particle partitioning suggests chemical segregation due to the spatial heterogeneity of emissions likely influences the aerosol state.

### 1.2.3 Sub-grid scale variability of aerosols

The spatial heterogeneity of emission sources and aerosol processes such as coagulation and gas-particle partitioning vary on scales smaller than the grid resolution of current global climate models (GCMs) and regional scale models. This further complicates calculation of climate relevant properties (optical properties and CCN activity) and their associated ERF due to uncertainty in the sub-grid variability of both gas phase

and aerosol concentrations and properties. Past efforts to quantify the sub-grid variability of aerosols and their associated properties have centered around the comparison of coarse resolution, large-scale observational or modeling domains against higher resolution versions of the same domain. The resulting difference in the aerosol state between coarse and fine resolution domains serves as a measure of structural uncertainty in coarse-resolved models due to the inability to capture the full spatial heterogeneity of aerosols.

Lin et al. 2017 conducted a modeling study to evaluate the sub-grid variability in aerosol number and mass concentrations over the southern Pacific Ocean. The model, WRF-Chem, was run over a 900x900 km region at a grid resolution of 3x3 km and aerosols were modeled using the three-mode MAM3 scheme. A 360x360 km study region in the center of the modeling domain was further divided into various grid boxes representative of GCM resolutions ranging from 180x180 km to 30x30 km. At each resolution, grid cell averages were computed alongside the sub-grid standard deviation at the native model resolution of 3x3 km. The authors found that aerosol number and mass concentrations are highly variable, with the greatest variability in standard deviation found in the free troposphere.

Weigum, Schutgens, and Stier 2016 quantify sub-grid variability in aerosol optical depth (AOD) and CCN concentrations for a modeling region encompassing the United Kingdom and northern France. WRF-Chem modeling runs are conducted first at 10 km resolution and subsequently at coarser resolutions (40, 80, 160 km). Aerosols are modeled using a three mode version of the MADE/SORGAM module, which combines the Modal Aerosol Dynamics model for Europe (MADE) with the Secondary Organic Aerosol Module (SORGAM). When comparing the 80 km resolution case (typical of most GCM resolutions) against results at 10km, the authors find an underestimation of AOD by 20-40% and an underestimation of CCN concentrations by 33% on average<sup>1</sup>. They note that the processes most affected by neglecting aerosol sub-grid variability include gas-phase chemistry and aerosol water uptake. For instance, changes in AOD are linked to the water content of the accumulation mode, which is largely regulated by gas-particle partitioning of the sulfate-nitrate-ammonium system. The authors note that boundary layer nitrate concentrations are up to 20% lower in the 80 km scenario, leading to a reduction in aerosol water content. The impact of aerosol sub-grid variability on nitrate concentrations is particularly meaningful, as recently GCMs have begun to

---

<sup>1</sup>Note that Weigum, Schutgens, and Stier 2016 compare coarse resolution results against the highest resolution scenario for two types of simulations: runs where the resolution of only the aerosols and gasses are lowered (all other environmental variables and dynamics are resolved at the base 10 km resolution), and those in which all model parameters and dynamics are represented on the coarse grid mesh. Results discussed here compare the high and low resolution simulations where the resolution of all model parameters was lowered (these simulations are referred to as “FRA10” for the full-resolution 10 km run and “FRA80” for the full-resolution 80 km run). This approach matches the manner in which past studies have evaluated sub-grid variability across modeling scales and crucially considers the coupled impact of resolution on meteorology and aerosol processes.

include nitrate aerosol in the calculation of direct radiative forcing.

Y. Qian, Gustafson, and J. D. Fast [2010](#) conduct a modeling study to measure sub-grid variability of both gasses and aerosols in a region over central Mexico. The authors use WRF-Chem and compare modeling results at 75x75 km resolution against two higher resolution scenarios (15x15 km and 3x3 km). Aerosols are modeled using the 8-bin sectional MOSAIC model and CBMZ is used for gas phase chemistry. Probability density functions (PDFs) are created for the distribution of trace gases and aerosols captured by the higher resolution simulations over a region of high urban emissions (Mexico City) and indicate that longer-lived compounds (e.g., CO in the gas phase and BC in the aerosol phase) tend to have broader distributions, indicating greater sub-grid variability. Faster reacting species (e.g., ozone in the gas phase and sulfate, nitrate, and ammonium in the aerosol phase) tend to have narrower PDFs, suggesting less sub-grid variability. The daytime vertical profile of sub-grid variability for trace gasses including CO and ozone are nearly uniform within the PBL, indicating they are well mixed, whereas the sub-grid variability of BC, sulfur, nitrate, and ammonium reach a maximum at the top of the PBL. Emissions contribute significantly to sub-grid variability by up to 50%, especially during the daytime for less reactive species in the vicinity of urban regions.

Gustafson Jr., Yun Qian, and Jerome D. Fast [2011](#) extend on the work of Y. Qian, Gustafson, and J. D. Fast [2010](#) by using the same modeling region and simulation setup; however, their analysis focuses on the contribution of sub-grid variability to direct aerosol radiative forcing. The authors find that over the Mexico City metropolitan area, daytime mean bias for top-of-atmosphere direct aerosol radiative forcing is in excess of 30% when comparing modeling results at coarse resolution (75x75 km) against the highest resolution scenario (3x3 km). Furthermore, the depiction of emissions contributes significantly to direct aerosol radiative forcing. This is because emissions rates such as dust are dependent on local wind speeds and higher resolution simulations better resolve local flow heterogeneities that result in a greater concentration of suspended dust.

Crippa et al. [2017](#) conduct a modeling study over eastern North America to measure the effects of resolution of meteorological, gas phase, and aerosol properties including AOD. WRF-Chem is used alongside the three-mode MADE/SORGAM module for representation of aerosols. Simulations are run at both 60 and 12 km resolution. In addition to direct comparison between model runs at each resolution, meteorological outputs are evaluated against reanalysis data while simulated AOD is compared against MODIS satellite observations. The skill of model outputs is measured using Brier skill scores. The authors find that the higher resolution 12 km simulations agree more closely with meteorological reanalysis and AOD observations, however, notable differences are still present at 12 km, especially in comparing AOD measurements to

MODIS observations. The authors note that this discrepancy made be in part due to the choice of a modal aerosol representation, as the geometric standard deviation of each mode is fixed and past studies have shown that modeled AOD is sensitive to the choice of standard deviation (Brock et al. 2016; Mann et al. 2012).

Jerome D. Fast, Bell, et al. 2022 evaluate the sub-grid scale variability of aerosol properties in an observational campaign using aircraft measurements over the Atmospheric Radiation Measurement (ARM) program's Southern Great Plains (SGP) site in north Oklahoma. A 162x162 km study region was divided into gridded domains representative of model resolutions typical of GCMs (81 km), future climate models (27 km), current global forecast models (9 km), and cloud-resolving models (3 km). Aircraft measurements of aerosol number distributions, CCN concentrations, and aerosol composition were averaged within each grid resolution and cell averages were compared against mean values within coarse-resolved 81 km cells. The authors find considerable sub-grid variability in the concentration of aerosol organic matter which comprises much of the aerosol composition due to the abundance of biogenic sources that release precursor BVOCs in the vicinity of the SGP site. 3 km cell averaged size distributions are shown to have much higher variability than their 81 km cell averaged counterpart due to local industrial sources of ultrafine particles and indicate that bi-modal or multi-modal distributions are averaged out at coarse resolution. It is suggested that differences in representation of the size distribution due to spatial averaging of sub-grid variability may lead to errors in CCN concentrations for GCMs.

#### **1.2.4 Modeling approaches and parameterizations for emissions sub-grid scale variability**

Numerous modeling approaches and parameterizations have been developed for incorporating the effects of sub-grid variability resulting from the spatial heterogeneity of both gas phase and aerosol emissions. A straightforward approach to representing sub-grid variability is simply to refine the mesh to sufficient resolution, however global modification to the grid resolution imposes significant computational cost, especially for 3-dimensional domains where a doubling of resolution along each dimension results in an eight-fold increase in the total number of grid cells. Alternatively, adaptive grid modeling allows local refinement of the mesh in regions of high heterogeneity such as near localized emissions sources. The total number of grid cells remains the same under refinement, however this comes at the cost of coarser resolution in regions that are not subject to refinement. Adaptive grid modeling has been applied in numerous regional-scale air quality models in order to improve representation of emissions plume structure and spatial heterogeneity (Karamchandani, Vijayaraghavan, and Yarwood 2011).

While adaptive grid modeling lowers computational cost relative to the approach of global mesh refinement, computational overhead is incurred due to the need to recompute the grid mesh at regular intervals. By contrast, plume-in-grid (PinG) modeling preserves the original, Eulerian mesh resolution while improving representation of emissions plumes at sub-grid scales via the use of an embedded Lagrangian framework. The embedded model is used to track the local dispersion of sub-grid scale emissions plumes until local concentrations are sufficiently diffuse, at which point the plume is handed over to the Eulerian grid. PinG modeling requires a-priori knowledge of the plume morphology in order to accurately represent its dispersion, a fact which hampered early implementations of PinG due to the limited choice of plume geometries (e.g., ellipses, Gaussian distributions, etc.) (Karamchandani, Vijayaraghavan, and Yarwood 2011). In recent years, improved plume models such as SCICHEM have been embedded in numerous chemical transport models, including the U.S. Environmental Protection Agency's CMAQ model, CAMx, and the Weather Research and Forecasting model coupled to chemistry (WRF-Chem).

Galmarini, J.-F. Vinuesa, and Martilli 2008 proposed a parameterization for the sub-grid variability of emitted, non-reactive scalars in the PBL applicable to models ranging from regional to global scale. Their approach required representing the evolution of the scalar concentration variance via a prognostic equation, for which closure of the covariance between emission fluctuations and scalar concentration values was presented. Closure constants were derived via LES and the parameterization was evaluated by comparing Reynolds Averaged Navier Stokes (RANS) simulations with the sub-grid parameterization against LES results.

Cassiani et al. 2010 developed a method for representing the emission, transport, and dispersion of reactive scalars (e.g., reactive gas phase compounds) via an ensemble of stochastic fields. The stochastic fields represent the concentration PDF, where the transport equation solution for the concentration PDF is solved via the ensemble of stochastic field members. Provided an emissions inventory with resolution higher than that of the modeling domain, one can construct an emissions PDF which provides a source term for the evolution of the stochastic fields. By contrast to the method of Galmarini, J.-F. Vinuesa, and Martilli 2008, the stochastic fields method is notable in providing formal closure for an arbitrary number and type of chemical reactions. This aspect is particularly valuable for atmospheric chemistry models given the impacts of chemical segregation due to emissions heterogeneity and turbulence on second order reactions as discussed previously.

In addition to modeling approaches and parameterizations which address the sub-grid scale variability of

emitted scalars such as gas phase species, recent progress has been made in the sub-grid scale representation of aerosol processes such as coagulation. Pierce et al. 2009 developed a parameterization for the coagulation of aerosol particles within sub-grid scale plumes. The parameterization estimates the number of particles that remain after coagulation and which are transferred outside the emitting grid cell. Subsequently, Sakamoto et al. 2016 created a parameterization for growth in aerosol diameter due to sub-grid coagulation in biomass burning plumes. Rammarine et al. 2019 applied the sub-grid coagulation parameterization of Sakamoto et al. 2016 to evaluate its impact on global aerosol size distributions and radiative effects in the GEOS-Chem-TOMAS (Two-Moment Aerosol Sectional) model. The authors found that including sub-grid coagulation led to a 37% reduction in particles 80 nm and larger (a chosen proxy for particles capable of activating as CCN), resulting in a decrease in the magnitude of indirect radiative forcing (-76 to -43  $\text{mW m}^{-2}$ ). Furthermore, the inclusion of sub-grid coagulation shifted the size distribution to more efficient scattering, increasing the all-sky direct radiative effect from -224 to -231  $\text{mW m}^{-2}$ .

## 1.3 Representation of aerosols across modeling frameworks

### 1.3.1 Aerosol modeling treatments

We have shown that the size, composition, and properties of aerosols are highly diverse and contribute to the complexity of their environmental feedbacks including direct and indirect radiative forcing. In turn, modelers must decide how much of the underlying aerosol complexity to represent when conducting aerosol-aware simulations. As an underlying principal, modelers must balance computational expense with aerosol model complexity (and therefore aerosol representability) and these two attributes generally move in tandem (i.e., computational cost increases as the complexity and representability of the aerosol treatment increases).

Thus we may consider an aerosol modeling hierarchy organized from aerosol model treatments with low complexity and computational cost to treatments that possess high complexity and representability alongside increased computational expense. Figure 1.1 shows a series of four aerosol model treatments from across the aerosol modeling hierarchy with low complexity models in the top left and high complexity models in the bottom right. For each subfigure, the model treatment represents the same underlying aerosol population composed of three general species A, B, and C. Moving through this Figure 1.1 sequentially, (a) corresponds to a bulk aerosol model in which only the bulk composition of the population is tracked. The aerosol population is not size-resolved, meaning that the population is monodisperse with a single prescribed

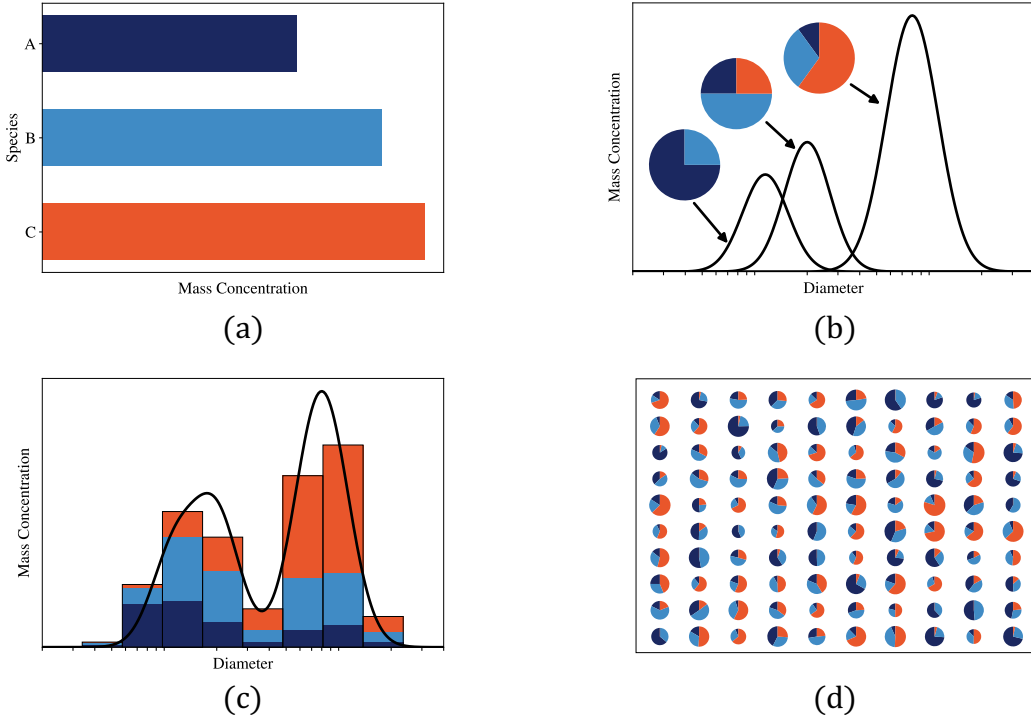


Figure 1.1: Cartoon representations of aerosol modeling treatments, each for the same aerosol population. The following representations are shown: (a) Bulk, (b) Modal, (c) 1-D sectional, (d) Particle-resolved.

particle diameter. Bulk models are the simplest aerosol treatment and require low computational cost.

Figure 1.1 subfigure (b) shows a modal aerosol treatment. In a modal model, the aerosol population is size-resolved and numerous lognormal distributions (“modes”) are used to represent the size distribution. Within each mode, the aerosol composition is the same (i.e., the particles are internally mixed within a mode) and across modes the composition can differ (the aerosol particles are externally mixed across modes). Therefore, the compositional complexity of a modal model is tied to the number of modes represented by the model. The example shown illustrates a three-mode model, which is a common configuration for modal aerosol models. A thorough listing of modal models ranging in configuration from three to 16 modes is provided in N. Riemer, Ault, et al. 2019 Table 5. Note that because modal models must maintain lognormal distribution shapes, this introduces structural uncertainty in the representation of aerosols as the size distribution is artificially altered to ensure lognormal distributions. As discussed previously, this limitation of modal models helped to explain discrepancies found by Crippa et al. 2017 between satellite observed AOD and modeled values.

Moving to higher aerosol model complexity, Figure 1.1 subfigure (c) shows a sectional aerosol treatment. Sectional models represent the aerosol size distribution using a series of adjacent bins (“sections”). Similar to

the modal aerosol treatment, the composition of particles within each bin is the same while the composition is allowed to vary across bins. The example sectional treatment illustrates a 1-D sectional model with eight bins. Higher dimensional sectional models exist such as 2-D and 3-D representations whereby the additional dimension(s) is used to represent additional aerosol properties (e.g., the 3-D sectional framework of Ching et al. 2016 adds dimensions for BC mass fraction and hygroscopicity).

Lastly, Figure 1.1 subfigure (d) shows a representation of a particle-resolved model. Among the aerosol modeling hierarchy, particle-resolved models possess the highest degree of compositional complexity and representability due to the direct representation of aerosol particles via a set of computational particles. The size and composition of each particle is allowed to vary and evolution of the aerosol state is tracked by solving the general dynamic equation describing processes (e.g., transport, coagulation, condensation, emission, deposition, nucleation) that alter and age the aerosol population. In a particle-resolved model, computational particles are represented by an  $A$  dimensional vector  $\vec{\mu}^i \in \mathbb{R}^A$  where  $A$  is equal to the number of aerosol species and the vector magnitude along each dimension  $\vec{\mu}_a^i$  corresponds to the mass of species  $a$  in computational particle  $i$  for  $a = 1, \dots, A$  and  $i = 1, \dots, N_p$ . Changes to aerosol composition due to gas-particle partitioning directly alter the computational particle vector  $\vec{\mu}^i$ . Processes including coagulation, deposition, and dilution are treated in a stochastic manner building off the Monte Carlo algorithm for stochastic collision-coalescence of cloud drops developed by Gillespie 1975. While particle-resolved models represent individual computational particles, it is customary to assign each particle a weighting (i.e., a multiplicity factor) in order for the set of computational particles to accurately resemble the number concentration of typical aerosol populations. This is because the number of particles per unit volume can be quite high and representing each individual particle would be computationally prohibitive as the numerical cost of particle-resolved models tends to scale with the number of computational particles.

Examples of particle-resolved models include the Particle Monte Carlo model (PartMC) (N. Riemer, M. West, et al. 2009). PartMC is a box model, meaning that the relative position of particles within a grid cell are not tracked. PartMC has been used to describe the complex mixing state (i.e., the compositional diversity within and across aerosols) of particles containing BC and their aging alongside quantification of the processes that contribute to aging (N. Riemer, M. West, et al. 2009). This represents a key advantage of particle-resolved models over coarser-resolved aerosol treatments, as the full complexity of the aerosol compositional diversity and the processes contributing to aging can be measured in a manner not possible with coarser-resolved aerosol models. Furthermore, particle-resolved models have been used to quantify error in coarser aerosol

models regarding the prediction of climate-relevant aerosol properties including CCN activity and optical properties. Zaveri, Barnard, et al. 2010 developed a “composition-averaging” post-processing technique for averaging the compositional diversity of particle-resolved output to match that of coarser-grained aerosol models such as sectional treatments. The authors found that when the aerosol population composition was averaged to match that of a 10-bin sectional model, the resulting CCN concentrations were overestimated in the sectional treatment by up to 125%. This illustrate the large degree of structural uncertainty present in coarser-resolved aerosol models regarding the representation of CCN activity. Fierce et al. 2024 directly quantified this structural uncertainty between particle-resolved and modal estimates of CCN activity by comparing PartMC with the four-mode MAM4 model. The authors found that CCN activity diverged between the two models after a couple of hours and that conditions with rapid aging such as in polluted regions with a high rate of coagulation and gas-particle partitioning amplified the model disagreement.

### 1.3.2 Joint aerosol-transport models

Models which jointly represent aerosols, their aging, transport, and feedbacks on the environment alongside broader-scale atmospheric dynamics are typically a coupled system of models, one responsible for the aerosol representation as previously discussed and another model which handles atmospheric transport and evolution of meteorological variables. Global and regional scale models typically represent transport via RANS which models the mean flow and fully parameterizes turbulent transport. As discussed previously, the spatial heterogeneity of emissions and other atmospheric constituents vary on scales smaller than the resolution of large scale models and thus turbulence-chemistry interactions and the impacts of chemical segregation between reactive compounds is not resolved. Joining these considerations with the impact of aerosol modeling treatment on the representation on aerosol properties such as CCN activity, there exists a need for high resolution models which utilize detailed aerosol treatments coupled with transport schemes which explicitly resolve both steady mean state and turbulent flow.

Recently, turbulence-resolving models such as UCLALES-SALSA (Tonttila et al. 2017) and the Dutch Atmospheric Large Eddy Simulation (DALES) model (Bruine et al. 2019) have coupled LES transport schemes along aerosol model treatments. Both models have been used to investigate aerosol-cloud interactions and compare model outputs against field campaign measurements. Although these models have high-resolution transport schemes, they each possess relatively coarse-resolution aerosol treatments. For instance, UCLALES-SALSA uses a 10-bin sectional treatment while DALES implements a modified version of

the seven-mode M7 model to allow two additional hydrometeor modes. To our knowledge, no modeling framework has yet to leverage a high-resolution particle resolved aerosol treatment alongside turbulence resolving transport models such as LES.

## 1.4 Objectives of this thesis

Past research has established a clear link between the spatial heterogeneity of both gas phase and aerosol emissions, the processes by which the aerosol age, and their resulting climate-relevant properties including CCN activity which contribute to indirect radiative forcing. Simultaneously, there exists large uncertainty in the radiative forcing due to aerosols which results in part from the coarse representation of both aerosols and their transport in global scale models and their coupling with non-linear processes that occur at the sub-grid scale such as coagulation and turbulence-chemistry interactions. Past research has led to the development of detailed aerosol model treatments and transport representations, however there has yet to be a direct coupling between particle-resolved aerosol models and turbulence-resolving transport models for use in quantifying the effects of emissions spatial heterogeneity on the aerosol state and CCN activity.

This thesis aims to address this gap in the literature by conducting a series of first-of-a-kind simulations using the coupled model WRF-PartMC-LES which allows particle-resolved large eddy simulations. The impacts of emissions spatial heterogeneity on the aerosol state including CCN activity are investigated by quantifying changes to aerosol size, number concentration, mass fraction, and hygroscopic properties across a variety of emissions scenarios. This thesis serves to answer the following principal scientific questions:

- What is the effect of emissions spatial heterogeneity on aerosol processes (e.g., coagulation, chemistry, etc.)?
- As emissions spatial heterogeneity alters the aerosol processes that occur, how does this change the aerosol properties (e.g., composition, concentration, hygroscopicity) and resulting CCN activity?
- How is the impact of spatial heterogeneity on aerosols modulated by changes to the composition of emissions?

In addition to the primary goals of this thesis, the development of a coupled particle-resolved large eddy simulation modeling framework presents a valuable benchmark against which the representation of aerosols in coarser-resolved models (either in transport treatment or aerosol treatment) can be compared.

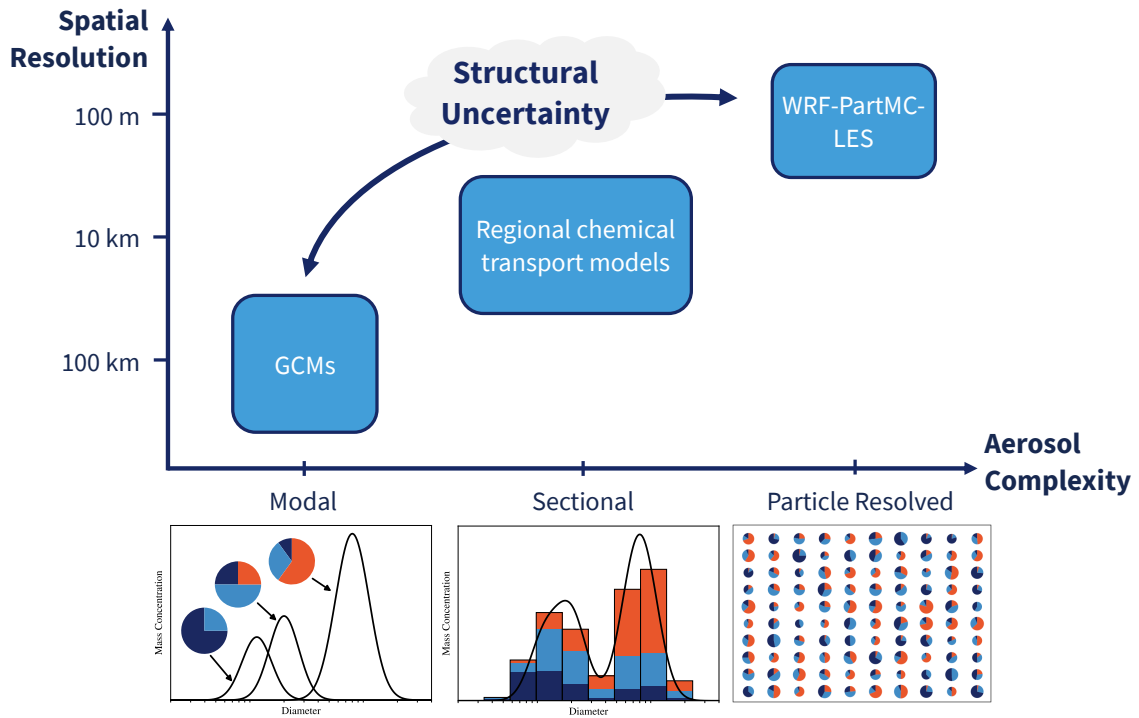


Figure 1.2: Use of WRF-PartMC-LES as a benchmark against coarser resolved aerosol-transport models for quantifying structural uncertainty in aerosol properties.

To illustrate this future role for WRF-PartMC-LES, Figure 1.2 shows a representation of models in a joint aerosol-transport model hierarchy. Models closer to the top right have high resolution in both space and aerosol treatment (here the spatial resolution is treated as a proxy for transport as higher resolution allows explicit depiction of turbulent transport scales). WRF-PartMC-LES serves as a benchmark against which coarser resolved models such as GCMs and regional scale models are evaluated. Structural uncertainty in key climate-relevant aerosol properties including CCN activity and aerosol optical properties could be quantified in a self-consistent manner, thereby improving understanding of uncertainty in direct and indirect radiative forcing due to aerosols.

# **Chapter 2**

## **Quantifying emissions spatial heterogeneity and mixing**

This chapter provides an overview of spatial heterogeneity (SH) and its relevance to quantifying the spatial variability of atmospheric emissions. We begin with a brief discussion of cross-disciplinary efforts to quantify SH. We then narrow our focus to quantifying the heterogeneity and mixing of reactive compounds in the atmosphere and characterize the gap in existing approaches that necessitate the development of a new, generally applicable SH metric that we will use in this thesis. The remainder of this chapter is dedicated to discussing our novel SH metric, the development of a Monte-Carlo based method for efficiently computing the metric over large domains, and its application to measuring the SH of idealized 2D patterns.

### **2.1 Existing approaches to quantifying spatial heterogeneity**

SH is ubiquitous across the natural sciences ranging from ecology to atmospheric sciences. SH plays an important role in biological diversity, human land use and associated environmental feedbacks, and drives changes in atmospheric dynamics through spatially varying surface fluxes of heat, water vapor, and emissions. Despite its importance, quantifying SH is challenging in part because its definition can be highly dependent on the end use case. For instance, a metric used in geostatistics for measuring geographic variability in land use may not be particularly useful to an ecologist concerned with how spatially dependent a species population is on surrounding resources. Furthermore, mathematical assumptions central to the choice of metric such as scale similarity may not be applicable across use cases and thus limit the metrics' applicability. This has prompted the development of numerous metrics across disciplines that quantify SH. Here, we discuss various prominent SH metrics that range in applicability and complexity, and point to limitations in these approaches for use in quantifying emissions spatial heterogeneity.

### **2.1.1 Spatial autocorrelation and semivariograms**

Spatial correlation between measurements can be evaluated using correlograms and semivariograms. Correlograms are created by computing the correlation, measured via Pearson's correlation coefficient, between two measurements separated by a given distance. Once the correlation across all distances and associated measurement pairs is computed, correlation is plotted against distance. A similar approach is employed for semivariograms, where the variance is plotted against distance between measurement pairs. Cooper et al. 1997 apply these techniques to determine the spatial correlation in streams between snail density and algal biomass, which serves as an important microhabitat. The authors show how these metrics can be leveraged to quantify the spatial correlation and variability between measurements. While correlograms and semivariograms are useful for explaining the correlation and variance between spatially distributed measurements, they do not provide a one-point statistical measure of how spatially heterogeneous a region is, nor do they provide information on how variance for a quantity of interest is spatially arranged over a region.

### **2.1.2 Fractal dimensions**

A Fractal dimension, or fractional dimension, is a non-integer dimension (B. Mandelbrot 1967; B. B. Mandelbrot 1983). Surfaces with greater complexity across spatial scales have higher fractal dimensions and vice versa. Fractal dimensions are scale invariant, meaning that it can be used to evaluate heterogeneity across surfaces of varying area. Loke and Chisholm 2022 discuss their use in ecology and point to numerous important limitations and considerations when utilizing fractal dimensions. The authors note that in practice, measuring fractal dimensions is challenging due to the need to quantify the broad range of scales which may be limited by the resolution of measurement techniques. Additionally real-world objects and surfaces are not truly fractal because self-similarity breaks down at certain scales.

### **2.1.3 Lacunarity**

Surfaces with similar fractal dimensions can have dissimilar variations or texture (i.e., their variance can be arranged in different ways). This led Mandelbrot (B. B. Mandelbrot 1983) to introduce Lacunarity as a metric for quantifying the textural variation of surfaces with similar fractal dimension. Lacunarity is related to the distribution of scales of texture in a surface. Surfaces with a broader range of texture, including large and small gaps and variations, will tend to have high lacunarity. For more homogeneous objects, the distribution

of texture scales will be narrower and will result in a lower lacunarity value. Dong 2000 provide an overview of lacunarity and its use in geography and geographic information science (GIS) applications. They note that lacunarity is often quantified using a gliding box algorithm, for which the researcher must choose the gliding box size. Importantly, changes to the gliding box size do not ensure linear scaling of the difference between lacunarity of multiple patches, meaning that, for instance, a patch may have higher lacunarity compared to other patches at small gliding box sizes but may have lower lacunarity than other patches at larger gliding box size. While this may be a useful attribute of lacunarity if one wishes to evaluate the scale dependence of spatial variability and the scales at which patches appear spatially similar or dissimilar (indeed, this is a primary use case as outlined by Dong 2000), gliding box size introduces an additional parameter one must choose when quantifying spatial heterogeneity and could complicate intercomparison of lacunarity measurements.

#### 2.1.4 Information entropy based metrics

In landscape ecology, information entropy based metrics such as Shannon's evenness index are used to quantify the patchiness of topography that is divided among numerous land uses classes. Plexida et al. 2014 evaluate a number of metrics, including Shannon's evenness index, for measuring the topological variability and land use of central Greece. For its use in landscape ecology, Shannon's evenness quantifies how evenly distributed the various land use types in a region are. It is defined as Shannon's diversity index over  $N$  populations (i.e., the Shannon entropy) divided by the maximum diversity index. Shannon's evenness index is useful if evaluating a region with numerous patches that are divided into different categories; however, its use is less apparent for quantifying the spatial heterogeneity of a single scalar field.

#### 2.1.5 Nearest neighbor statistics for point-based heterogeneity

Shu et al. 2019 discuss nearest neighbor distance statistics for use in GIS settings to quantify the spatial heterogeneity of points and apply various metrics to example cases including the spatial distribution of crime events in a city, regional seismic activity in Yutian China, and taxi routes in Beijing China. These examples range from 2D to 4D, illustrating the multidimensional applicability of nearest-neighbor metrics. The authors present a goodness-of-fit metric based on the distribution of nearest neighbor distances called the level of heterogeneity. A normalized version of the metric is proposed to resolve issues that arise when comparing datasets with differing magnitudes due to differences in scale or intensity. The authors note that while

the proposed metric is suitable for capturing point-based spatial heterogeneity, it is quite computationally expensive. It is recommended that alternative nearest-neighbor metrics evaluated alongside the proposed metric should be preferred for computationally intensive datasets.

### 2.1.6 Multiscale norms

Sobolev norms have been used to quantify the mixing and transport of passive scalars in fluids (Thiffeault 2012). Sobolev norms act as a weighted sum of the Fourier coefficients resulting from the Fourier transform of a scalar field (i.e, the passive scalar suspended in either a fluid or the atmosphere). The multiscale nature of Sobolev norms refers to the selection of Sobolev space  $H^q$  over which the norm is defined. Thiffeault 2012 show that the choice of Sobolev norm for  $q < 0$  is valuable for flow mixing applications as the magnitude of the norm decays alongside the mixing of the medium.

## 2.2 Metrics for quantifying the mixing of reactive compounds

Atmospheric constituents that undergo chemical reactions including gas phase and aerosol species are subject to both spatial and temporal constraints that determine the rate at which reactions will proceed. For instance, species must be spatially collocated for reactions to occur, and they must remain in close proximity over the timescale that a given reaction will proceed. This gives rise to two important metrics: (1) segregation intensity, which quantifies the spatial proximity of reactive species and (2) the Damköhler number, which characterizes the dominant timescales governing the reactivity of species.

### 2.2.1 Segregation intensity

The segregation intensity, first theorized by Danckwerts 1952 for use in combustion processes, is a measure of how spatially segregated or mixed two reactive species are that follow a typical second-order reaction of the form



Using Reynolds decomposition to express each species concentration as the sum of a spatial average and local deviation,  $[A] = \overline{[A]} + [A]', [B] = \overline{[B]} + [B]',$  such that the chemical reaction proceeds as

$$\frac{d[A]}{dt} = \frac{d[B]}{dt} = -k \left( \overline{[A]} \cdot \overline{[B]} + \overline{[A']} \overline{[B']} \right). \quad (2.2)$$

The segregation intensity is then

$$I_s = \frac{\overline{[A']} \overline{[B']}}{\overline{[A]} \cdot \overline{[B]}}, \quad (2.3)$$

such that the chemical reaction can be expressed as

$$\frac{d[A]}{dt} = \frac{d[B]}{dt} = -k \left( \overline{[A]} \cdot \overline{[B]} \right) (1 + I_s). \quad (2.4)$$

Thus,  $I_s$  can be thought of as imposing an effective reaction rate  $k^{\text{eff}} = k(1 + I_s).$  When  $I_s = -1,$  species  $A$  and  $B$  are fully spatially separated, such that no reaction occurs. As  $I_s$  approaches zero, the two species become fully mixed and the effective reaction rate matches the ideal rate of reaction.  $I_s$  can also be positive, corresponding to positive covariance between species which effectively increases the rate of reaction.

## 2.2.2 Damköhler number

The Damköhler number (Damköhler 1947) relates the turbulence and chemical reaction timescales via the ratio

$$D_a = \frac{\tau_{\text{turb}}}{\tau_{\text{chem}}}. \quad (2.5)$$

The definition of turbulent and chemical timescales varies by application. For the convective boundary layer, Jean-François Vinuesa and J. V.-G. D. Arellano 2003 adopt the following expression for the Damköhler number,

$$D_a = \frac{z_i}{w_*} k[B], \quad (2.6)$$

where  $w_*$  is the velocity scale in the convective boundary layer and is defined as  $\left[ (g/\Theta_v) \overline{w\theta}_0 z_i \right]^{1/3},$  and where  $g$  is gravitational acceleration,  $\Theta_v$  is virtual potential temperature,  $\overline{w\theta}_0$  is vertical heat flux, and  $z_i$  is the boundary layer height.

Figure 2.1 displays the three primary regimes for the Damköhler number that determine the abundance of precursor concentrations  $[A]$  and  $[B].$  When the turbulent and chemical timescales are balanced,  $D_a = 1.$  If

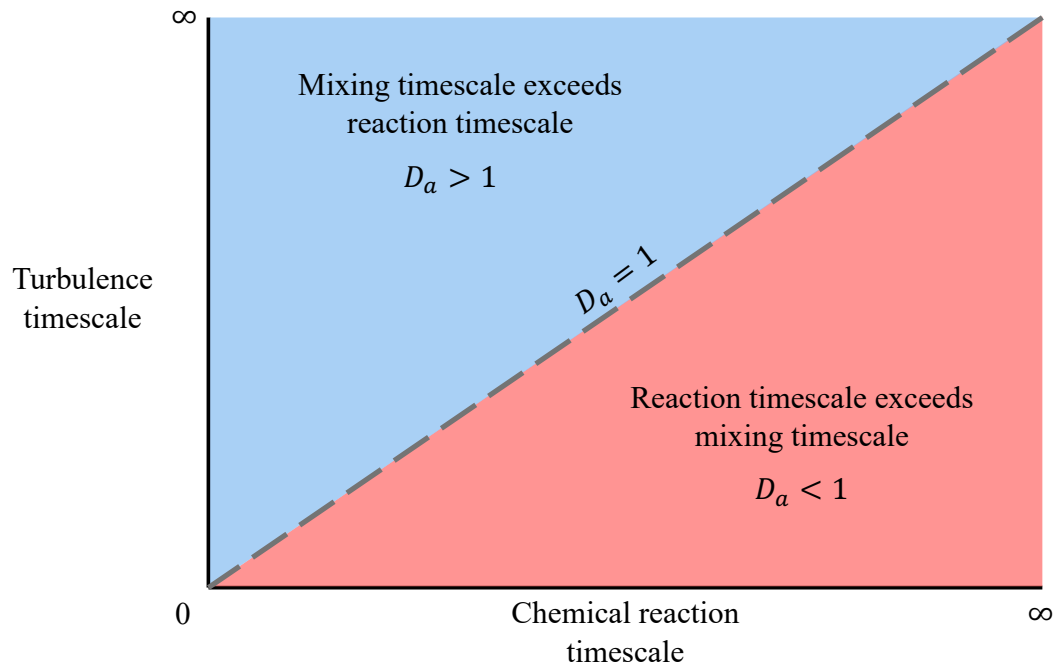


Figure 2.1: Dependence of the Damköhler number on turbulent and reactive timescales. Figure adapted from Kotamarthi and Feng 2017

the chemical reaction timescale is shorter than the turbulence timescale,  $D_a > 1$  and the concentration of the precursors will be determined by the rate at which turbulence mixes the reactive compounds (fast-chemistry regime). Conversely, if the chemical reaction timescale is slower than the turbulent timescale,  $D_a < 1$  such that the concentration of precursors is determined by the rate of chemical reaction (slow-chemistry regime). Thus, the Damköhler number indicates the relative importance of turbulence in chemical reactions – in the fast chemistry regime with reactions with  $D_a > 1$ , turbulent scales responsible for mixing the reactive compounds should be fully resolved. Examples of relevant gas-phase reactions in convective boundary layer that correspond to the fast-chemistry regime include oxidation of volatile organic compounds such as isoprene by OH to produce semi-volatile organic compounds that partition into the aerosol phase to form secondary organic aerosol. Additional fast reactions include the oxidation of  $\text{SO}_2$  by OH, resulting in  $\text{H}_2\text{SO}_4$  which possesses an extremely low volatility and rapidly condenses into the aerosol phase where it forms sulfate ( $\text{SO}_4^{2-}$ ).

## 2.3 A novel approach to quantifying spatial heterogeneity

Existing approaches to quantifying spatial heterogeneity discussed in Section 2.1 and metrics for mixing of reactive compounds in Section 2.2 provide valuable information on the state of a heterogeneously distributed field, however each metric varies in terms of range of applicability, interpretability, and ease of implementation.

For instance, spatial autocorrelation and semivariograms are relatively easy to interpret and are computationally efficient to measure, but they are primarily useful for capturing the correlation and variability at a single point rather than over an entire region. Alternatively, the nearest neighbor metric proposed by Shu et al. 2019 is useful across a broad range of applications as illustrated by the authors, however, their approach is computationally expensive and is not readily interpretable to the same manner as other spatial heterogeneity metrics. Metrics for mixing provide useful information on how spatially colocated reactive compounds are and the relevant timescales that determine the abundance of precursors, however they do not provide information on how the variance in the spatial distribution of each compound is arranged.

Thus, there exists the need for a novel spatial heterogeneity metric for use in atmospheric science applications including quantifying emissions spatial heterogeneity and subsequent atmospheric field heterogeneity once compounds are emitted into the planetary boundary layer. Mohebalhojeh et al. 2024 (in prep) have developed a new approach to measuring spatial heterogeneity with key benefits being that their approach is broadly applicable, straightforward to interpret, and computationally efficient to measure using a Monte Carlo approach discussed in Section 2.3.2.

### 2.3.1 Metric definition

The spatial heterogeneity metric, subsequently  $SH$ , quantifies the level of heterogeneity for single scalar quantity over a 2-dimensional surface. In this thesis, the scalar of interest is either gas phase or aerosol species and the 2-dimensional surface is either the ground level in the case of emissions or a horizontal plane through the computational domain to quantify atmospheric field heterogeneity within the planetary boundary layer.

$SH$  is calculated by summing up the absolute difference between the mean of a scalar quantity over a rectangular subset of the domain and the domain averaged value for all possible subsets. Over a discrete 2-dimensional grid with  $N$  cells along the x-axis and  $M$  along the y-axis, there exist

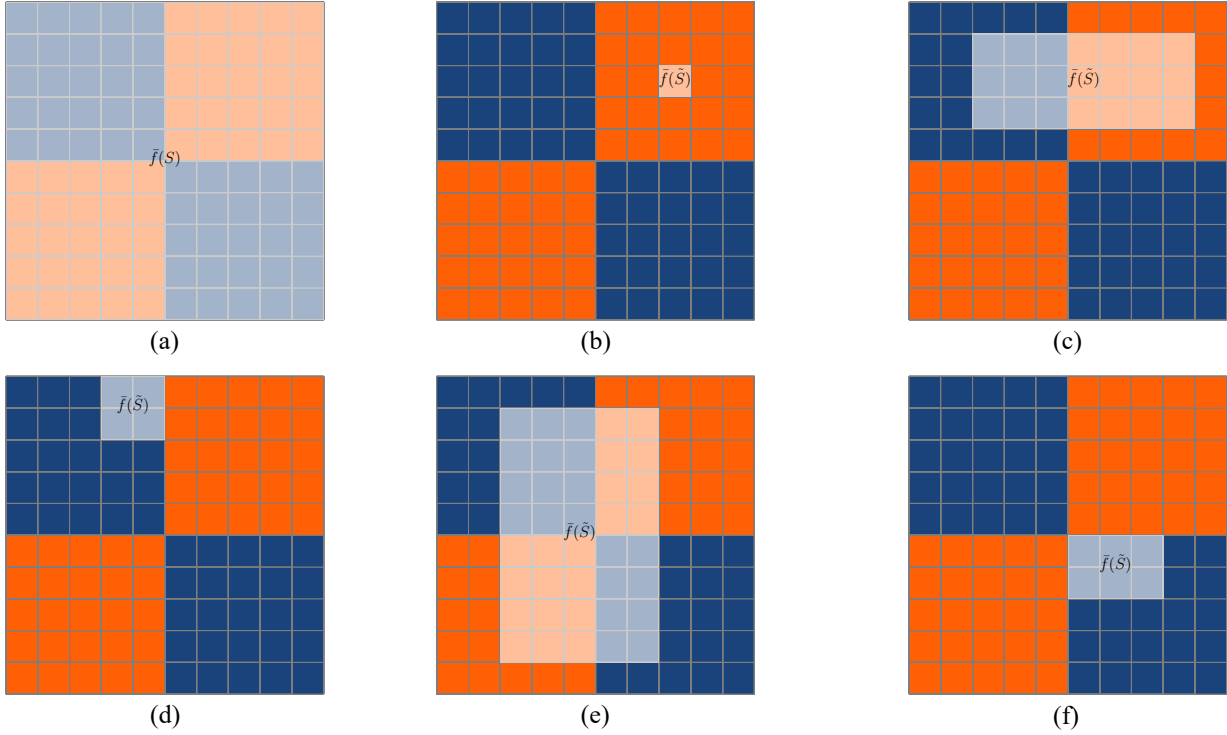


Figure 2.2: Example subsets for  $SH$  calculation. (a) Full domain mean. (b-f) Examples of rectangular subsets (highlighted regions) over which the subset mean is computed.

$P = (N(N - 1) + 1)(M(M - 1) + 1)$  total possible rectangular subsets. For a scalar field  $f$  defined over some domain  $S$ ,  $SH$  is computed as

$$SH(f, S) = \frac{1}{P} \sum_{\tilde{S} \in \mathbb{R}} |\bar{f}(S) - \bar{f}(\tilde{S})|. \quad (2.7)$$

Because the range of gas phase and aerosol emissions varies across orders of magnitude, it is useful to instead utilize a normalized version of the spatial heterogeneity metric,

$$SH(f, S) = \frac{1}{\bar{f}(S) [\frac{3}{2}(N \times M)(N - 1)(M - 1) + N(N - 1) + M(M - 1)]} \sum_{\tilde{S} \in \mathbb{R}} |\bar{f}(S) - \bar{f}(\tilde{S})|. \quad (2.8)$$

A visualization of the total domain mean  $\bar{f}(S)$  and domain subset means  $\bar{f}(\tilde{S})$  are shown in Figure 2.2. The checkerboard pattern represents an idealized emission pattern, where orange-filled cells correspond to regions of uniform emissions and dark blue regions correspond to zero emissions.  $\bar{f}(S)$  is shown in subplot (a), while five examples of rectangular subsets are displayed in subfigures (b-f).

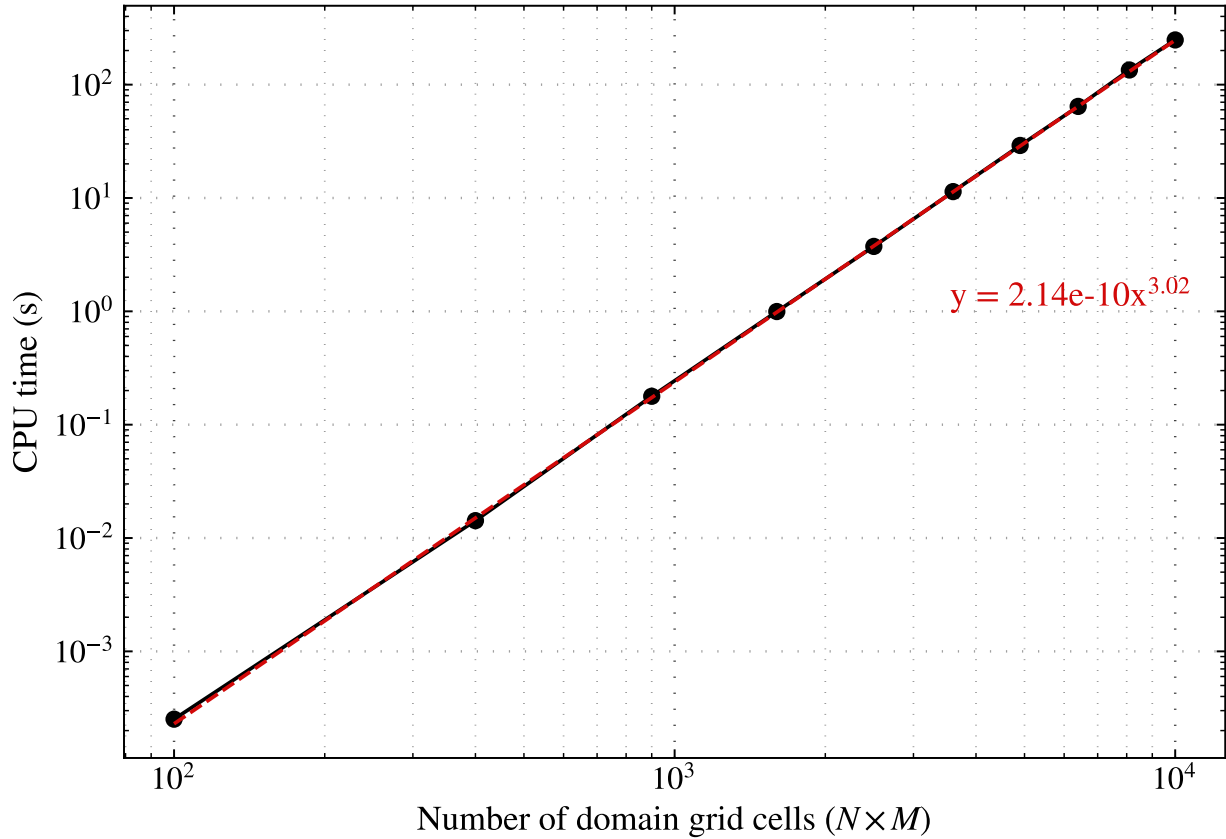


Figure 2.3: CPU time for the naive looping  $SH$  Fortran subroutine. The x-axis indicates the total number of domain grid cells (elements) in the array passed to the subroutine. A power law regression is plotted as the red dashed line.

### 2.3.2 Computational methods for computing the spatial heterogeneity metric

To calculate  $SH$  over a computational domain, an array comprising the scalar quantity of interest with dimension equal to the size of the domain ( $N$  by  $M$ ) is passed to a Fortran subroutine. Here, we discuss two approaches to calculating  $SH$ : a computationally expensive naive looping algorithm and a significantly more efficient Monte Carlo based method.

The naive subroutine loops over all possible rectangular subdomains which can be quite computationally expensive, especially for domains with a large number of grid cells (e.g.,  $100 \times 100$  grid cells laterally as used for domain mesh size in this thesis). Figure 2.3 shows the computational scaling for a Fortran subroutine using this naive looping algorithm. A power law regression (red dashed line) is fit to the CPU time vs. the total number of domain grid cells. The naive looping algorithm scales as  $O(n^3)$  for  $n$  the number of grid cells. For domain sizes used in this thesis ( $N = M = 100$ ), this results in a single calculation taking in excess of 2

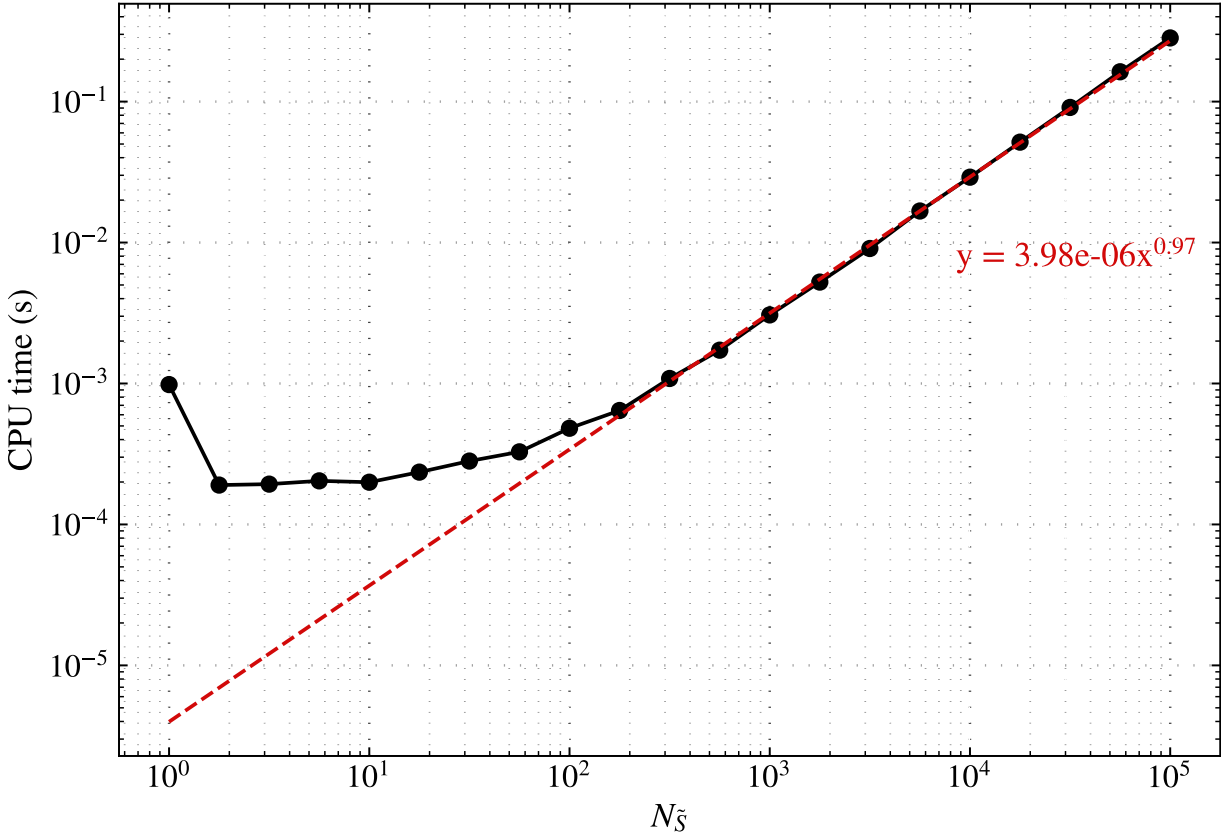


Figure 2.4: CPU time for the Monte Carlo  $SH$  Fortran subroutine. The x-axis indicates the number of domain subsets that are randomly selected to determine the  $SH$  estimate. A power law regression is plotted as the red dashed line.

minutes.

Instead of looping over every possible subdomain, we may use the fact that the probability of selecting any given subdomain is the same (i.e., the sampling probability is uniform across the entire domain) in order to construct a Monte Carlo sampling based approach for calculating  $SH$ . We then pass the array with domain scalar values alongside a parameter for the number of subsets to sample ( $N_{\tilde{S}}$ ) to our Monte Carlo-based Fortran subroutine. Figure 2.4 shows the CPU time for corresponding number of randomly selected domain subsets, ranging from 1 to 100,000 for a domain with dimensions  $N = M = 100$  and  $P = (100(100 - 1) + 1)(100(100 - 1) + 1) = 98,029,801$  total subsets. For a low number of randomly selected subsets (number of subdomains  $\lesssim 100$ ), the algorithm scales quite weakly, suggesting that computational overhead limits speedup in this region over the naive algorithm. As the number of subdomains increases above 100, the algorithm scales as  $O(N_{\tilde{S}})$  as indicated by the power law regression.

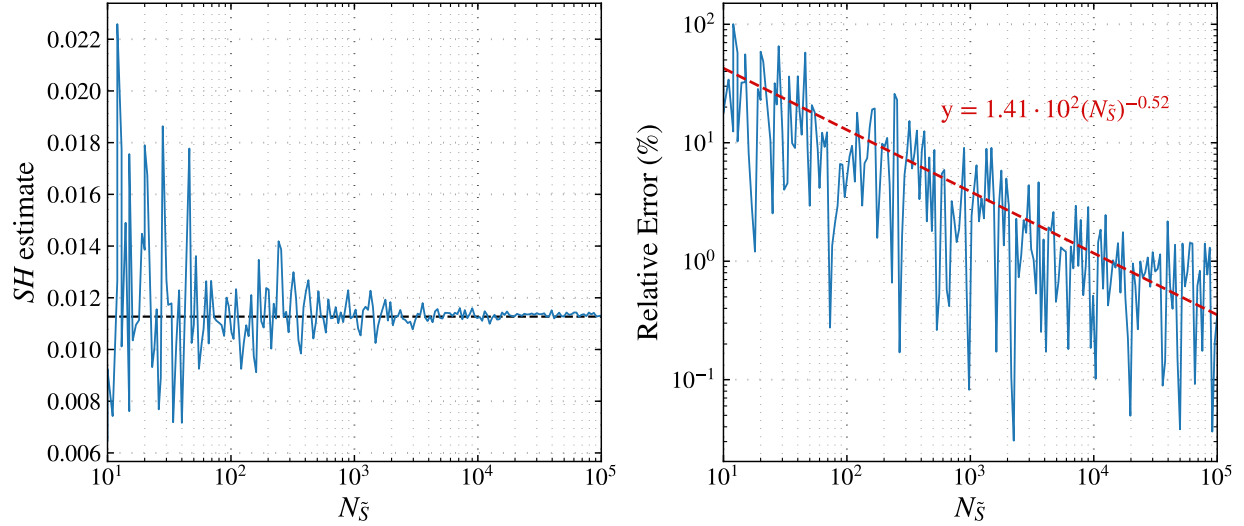


Figure 2.5:  $SH$  estimate in blue for the Monte Carlo sampling subroutine vs. the number of randomly selected domain subsets (top panel). The true value of  $SH$  computed via the naive algorithm is shown as the black line. Absolute relative error between  $SH$  estimate and the true value of  $SH$  (middle panel). Bias between  $SH$  estimate and the true value of  $SH$  (bottom panel)

We validate the accuracy of the Monte Carlo sampling subroutine against the naive looping approach in Figure 2.5. First, the precise value of  $SH$  was computed via the naive algorithm for a scalar field of random noise with dimensions  $N = M = 100$ . We then vary the number of randomly selected subsets  $N_{\bar{S}}$  used to compute the estimate of  $SH$  in the Monte-Carlo subroutine. The left panel in Figure 2.5 shows how the  $SH$  estimate converges on the precise value of  $SH$  (shown as a horizontal black dashed line). The right panel displays the relative error between  $SH$  estimates and the precise value (note the logarithmic scaling). Relative error decreases as  $\propto 1/\sqrt{N_{\bar{S}}}$  as indicated by the power law regression in red. This behavior is to be expected, because as the number of samples (i.e.,  $N_{\bar{S}}$ ) increases, the error should decrease like the standard error— $SE = \sigma/\sqrt{n}$  for  $\sigma$  the standard deviation of a sampling distribution and  $n$  the number of samples.

Given the performance of the Monte Carlo sampling subroutine over the naive looping approach and its ability to reach a high level of accuracy with minimal error when sampling a sufficient number of domain subsets, we utilize the Monte Carlo method for subsequent  $SH$  calculations. For such calculations, we choose the number of randomly selected domain subsets to be 10,000 as this results in relative error  $\sim 1\%$  for the domain size  $N = M = 100$  used in this thesis. Referring back to Figures 2.3 and 2.4 for naive algorithm performance and Monte Carlo sampling performance, respectively, we find that for a domain size with  $N = M = 100$ , CPU time is in excess of two minutes for the naive looping approach and of order  $\sim 0.1$  s for

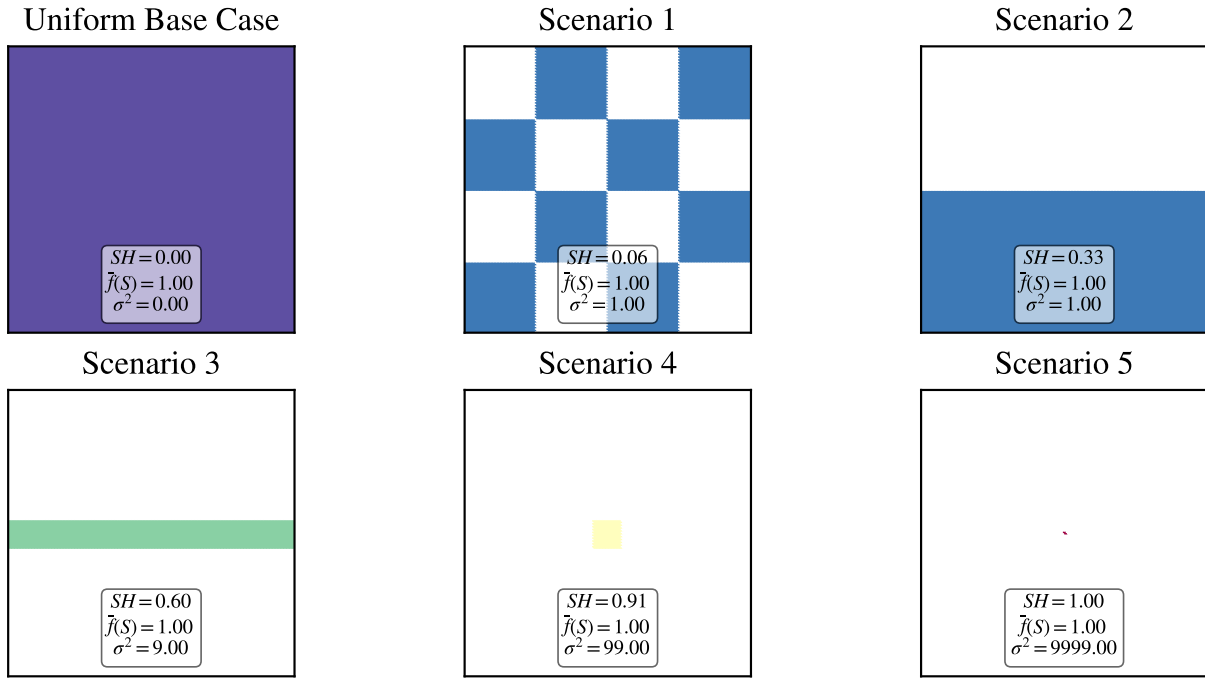


Figure 2.6: Example emission patterns arranged from least heterogeneous (“Uniform Base Case”) to most heterogeneous (“Scenario 5”). For each pattern, the spatial heterogeneity  $SH$  is listed alongside the domain mean ( $\bar{f}(S)$ ) and variance ( $\sigma^2$ ). The color of each scenario indicates the emission scaling relative to the uniform base case with red being the highest scaling.)

the Monte Carlo subroutine. This corresponds to a speedup in excess of 1000.

### 2.3.3 Example calculations for emission patterns

We calculate the spatial heterogeneity for 6 emission scenarios shown in Figure 2.6. Emission patterns are ordered from low to high  $SH$ , ranging from uniform emissions across the domain (“Uniform Base Case”) to highly heterogeneous localized emissions. Note that the total mass of emissions per unit time is the same across all scenarios. The emissions scaling rate is adjusted based on the area each pattern occupies relative to the base case and is indicated by the color of each emission region (dark blue corresponds to scaling closer to unity while red indicates the greatest magnitude of scaling).

For each scenario, the domain mean,  $\bar{f}(S)$ , and variance,  $\sigma^2$ , are shown in addition to  $SH$ . Note that the variance of the checkerboard scenarios 1 and 2 are all equal to 1.0 while the  $SH$  increases across these scenarios. This highlights an important attribute of the spatial heterogeneity metric—the  $SH$  metric provides information not only on how variable an emission pattern is across the domain, but also is sensitive to how the

variance is arranged. This marks an advantage of the  $SH$  metric over previously discussed metrics, including semivariograms, fractal dimensions, and information entropy statistical measures that are insensitive to changes in the distribution of variance over the scalar field of interest.

# Chapter 3

## Modeling tools

This chapter discusses the modeling tools necessary for conducting simulations presented in this thesis. A description of the transport treatment, large-eddy simulations, is provided alongside discussion of requisite sub-grid scale parameterizations that we utilize. Attributes of the computational domain, including its spatial extent, grid resolution, and other defining qualities are presented. Meteorological initial conditions for simulations are discussed as well as determination of necessary spin-up time for the development of convective boundary layer in the computational domain. Subsequently, chemical mechanisms used for gas phase and aerosol chemistry are discussed. Lastly, the aerosol model, PartMC, and its coupling with the chosen transport model is discussed.

### 3.1 Large-eddy simulations

Within the planetary boundary layer (PBL), turbulent eddies are responsible for mixing and transporting gases and aerosol particles as well as thermal and kinetic energy. Over time, these eddies break down due to flow instabilities, frictional losses due to interactions with physical boundaries, and the viscosity of the atmospheric constituents. Therefore, it is important for modeling frameworks that represent the PBL to explicitly resolve the physical scales over which transport and mixing occur, as well as accurately model the dynamical tendency of kinetic energy transfer from large to small eddies.

Representation of turbulence in modeling frameworks is a computationally challenging task because of the range of scales one must consider and the associated need for high spatial resolution. In the PBL, turbulent eddies range in size from hundreds of meters to the Kolmogorov length scale on the order of a few millimeters (Kolmogorov 1991), at which size eddies break down due to kinematic viscosity of atmospheric constituents. A widespread technique when modeling the PBL is the use of large-eddy simulations (LES). In LES, the equations of motion are filtered such that the largest, energy-containing eddies are explicitly

resolved down to a grid resolution on the order of 10 meters. For eddies smaller than the resolution of the grid, sub-grid scale (SGS) parameterizations are used to represent the statistical attributes of unresolved eddies, including their energy dissipation and stress forces.

For simulation results presented in this thesis, we use the Weather Research and Forecasting model (WRF) configured for LES (Skamarock et al. 2008). In practice, conducting LES studies in WRF arises from modeling choices including the representation of SGS turbulence parameterizations and adequately high grid resolution; that is, there is no “switch” for configuring WRF in LES mode, but rather structural choices which permit representation of the relevant dynamics.

### 3.1.1 Sub-grid scale parameterizations

A key choice in the implementation of LES is the selection of SGS turbulence parameterizations. Specifically, one must parameterize the SGS stress  $\tau_{ij}$  and SGS flux  $q_i$ . The stress tensor  $\tau_{ij}$  represents the deformational forces acting both normal ( $i = j$ ) and perpendicular ( $i \neq j$ ) to each grid cell, while the SGS flux  $q_i$  refers to the transport of scalars such as momentum, heat, or other quantities by unresolved eddies. A common technique for the closure of SGS stress and flux is the use of eddy-viscosity models. This technique was pioneered by Smagorinsky for parameterizing the motion of SGS eddies in a model of general circulation (Smagorinsky 1963). Eddy-viscosity models mimic the linear relationship between the stress tensor of a Newtonian fluid and shearing forces acting on the fluid scaled by the fluid’s molecular viscosity. As such, eddy-viscosity models are not fundamentally grounded in physical tendencies of turbulent flows, but rather provide an empirical approximation that mimics Newtonian fluids and has been shown to be reasonable for representing SGS turbulence in modeling studies of the PBL (Stoll et al. 2020). The SGS stress and SGS flux are then expressed as

$$\tau_{ij} = -2v_T \tilde{S}_{ij}, \quad (3.1)$$

$$q_i = -v_\theta \frac{\partial \tilde{\theta}}{\partial x_i}, \quad (3.2)$$

where  $v_T$  is the eddy viscosity coefficient,  $\tilde{S}_{ij} = \frac{1}{2}(\partial \tilde{u}_i / \partial x_j + \partial \tilde{u}_j / \partial x_i)$  is the resolved strain rate tensor (i.e., the rate at which straining forces such as expansion and shearing due to resolved flow occur),  $v_\theta$  is the eddy diffusivity coefficient for some scalar quantity  $\theta$ , and  $\partial \tilde{\theta} / \partial x_i$  is the resolved-scale gradient of scalar  $\theta$  in direction  $x_i$ . As  $\tilde{S}_{ij}$  and  $\partial \tilde{\theta} / \partial x_i$  are known quantities determined at the resolved scale, eddy-diffusivity

models then become a matter of determining  $v_T$  and  $v_\theta$ .

Deardorff was the first to implement Smagorinsky's eddy-diffusivity SGS model for LES, however, he found that the model was overly diffusive for short wavelength features (Deardorff 1970). Deardorff 1980 instead proposed an alternative eddy-diffusivity model in which a prognostic equation for SGS kinetic energy  $E$  is solved alongside expressions for  $v_T$  and  $v_\theta$

$$\frac{\partial E}{\partial t} = -\frac{\partial \tilde{u}_j E}{\partial x_j} + 2v_T \tilde{S}_{ij} \tilde{S}_{ij} - v_\theta \frac{\partial \tilde{b}}{\partial z} + \frac{\partial}{\partial x_j} 2v_T \frac{\partial E}{\partial x_j} - \epsilon, \quad (3.3)$$

$$v_T = C_1 \ell \sqrt{E}, \quad (3.4)$$

$$v_\theta = \left(1 + 2 \frac{\ell}{\Delta}\right) v_T, \quad (3.5)$$

where  $b$  is buoyancy,  $\epsilon$  is the turbulent kinetic energy (TKE) dissipation,  $C_1$  is a coefficient that must be specified by the modeler, and  $\ell$  is the turbulent length scale. In this thesis, we use Deardorff's TKE scheme for eddy diffusivity. Customarily,  $C_1 = 0.1$  and we use this value as recommended by an idealized test case for LES simulations packaged alongside the WRF codebase.

### 3.1.2 Computational domain

We model the PBL in an 3D idealized domain with dimensions 10 km in both lateral dimensions and 2 km vertically. A horizontal resolution of 100 m was chosen alongside a vertical resolution of approximately 20 m<sup>1</sup>, resulting in a domain of 100x100x100 grid cells. This resolution is necessary to resolve eddies responsible for turbulent transport in the PBL. A higher resolution vertically is desired in order to accurately represent vertical motions due to convective and turbulent transport. Time discretization is set to 1 second for all simulations, however sub-models such as chemistry (when active) further refine time discretization to maintain stability for integration.

The domain is absent of any topographic features with a uniform, flat surface. Latitude and Longitude coordinates of (0, 0) are used internally for computing the solar zenith angle necessary for photolysis calculations, however, the domain's idealized topography is not intended to match the geographic region surrounding these coordinates.

---

<sup>1</sup>WRF uses a terrain-following pressure “eta” coordinate system for vertical levels. Note that because the domain only extends to 2 km vertically, vertical levels are nearly equally spaced apart.

### 3.1.3 Meteorological Initial Conditions

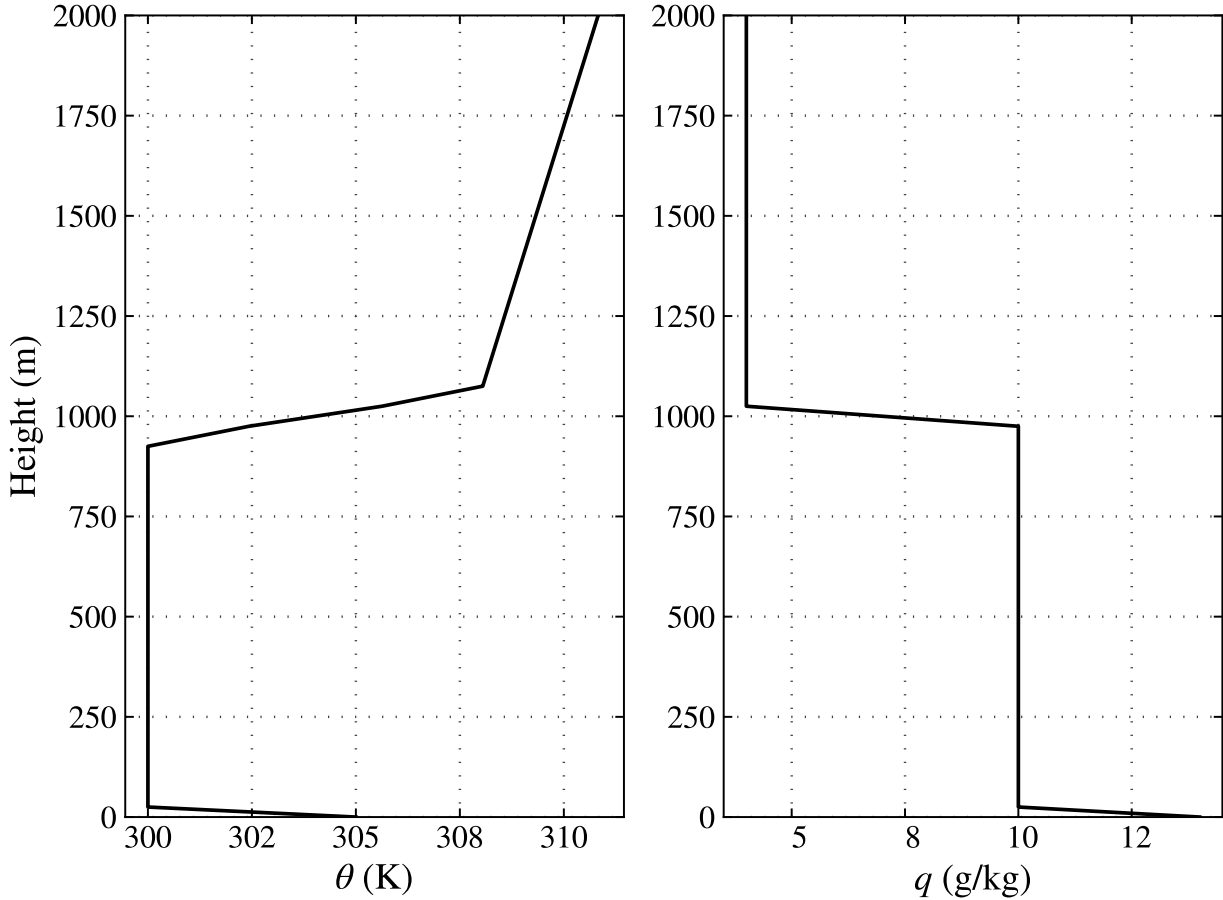


Figure 3.1: Idealized atmospheric sounding used for domain meteorological initial conditions. Initial conditions for potential temperature (left) and specific humidity (right).

The domain meteorological conditions are initialized using an ideal sounding typical of a convective boundary layer (see Figure 3.1). The lowest 25 m of the atmosphere are initially unstable to allow for parcels to rise due to buoyancy into the neutral PBL that extends to approximately 1 km. Above this point, the PBL is capped by an inversion up to 2 km.

Both zonal ( $u$ ) and meridional ( $v$ ) wind are set to zero throughout the entire domain. Tian et al. 2022 and Jerome D. Fast, Berg, et al. 2019 both show that the impact of surface heterogeneities in surface heat fluxes on cloud formation and type are sensitive to wind conditions, and are most pronounced for minimal background winds. Extending the relevance of these findings to this thesis, our choice of an initial condition characterized by zero winds is intended to isolate the impact of emissions spatial heterogeneity on the evolving atmospheric

state of gasses and aerosols.

At the surface, the specific humidity  $q$  is highest at  $14 \text{ g kg}^{-1}$  and lowers to a uniform  $10 \text{ g/kg}$  within the PBL. Above the PBL,  $q$  is a uniform  $4 \text{ g kg}^{-1}$  extending vertically to the top of the domain. At the surface, a uniform surface heat flux of  $0.24 \text{ K ms}^{-1}$  is set and random perturbations of the temperature field are imposed at the lowest four levels to initiate turbulence. The surface heat flux is responsible for maintaining convection and turbulent transport over the course of the simulation. Boundary conditions are periodic along all lateral boundaries.

### 3.1.4 Simulation spin-up

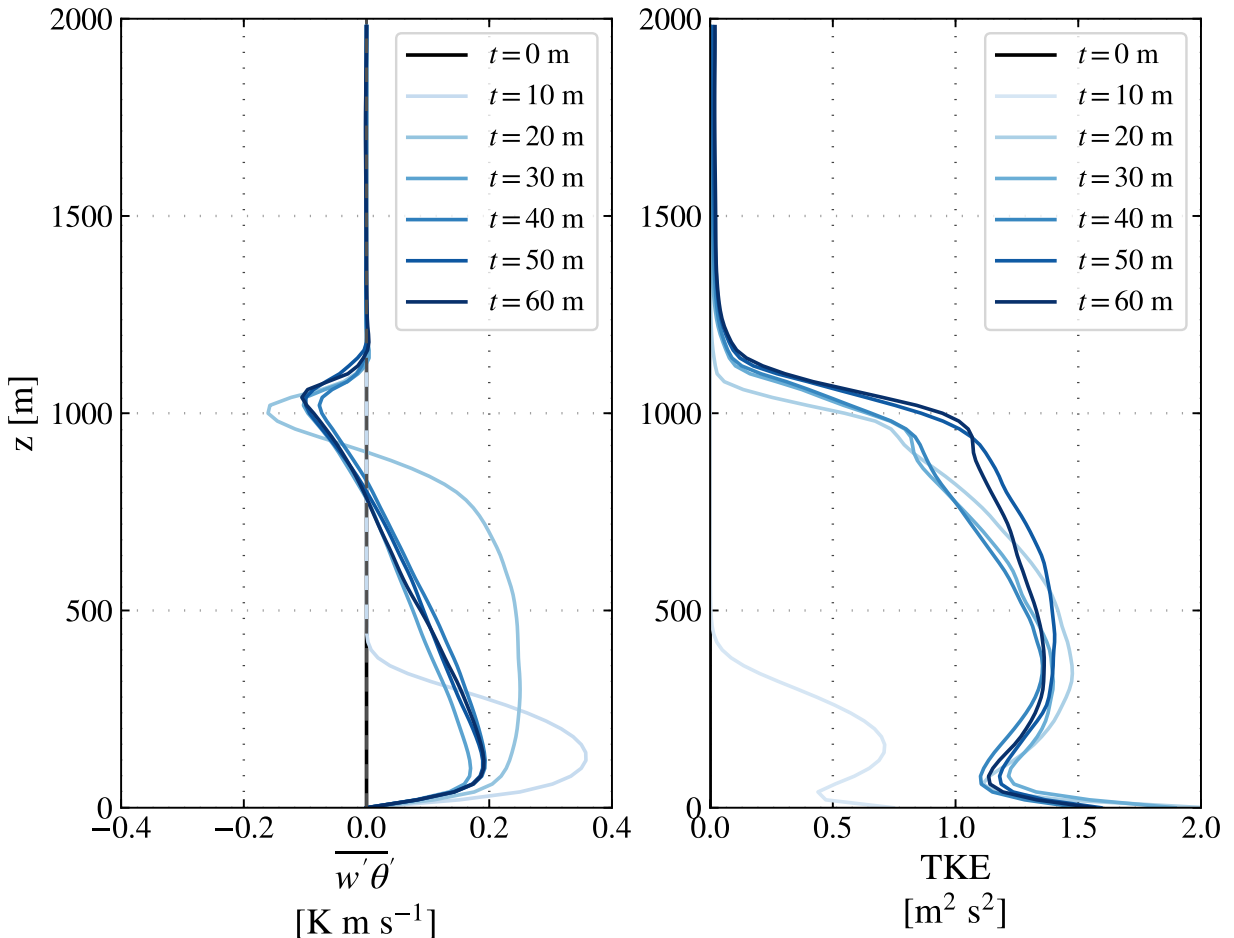


Figure 3.2: Resolved-scale vertical heat flux profiles (left) and TKE at intervals of 10 minutes during the first hour of simulation spin-up.

Prior to the release of gas and aerosol emissions, the simulation is allowed to spin up for a period of 1 hour.

During this time, convection and turbulence within the boundary become well established and thoroughly mix the initial conditions for gases and aerosols alongside transporting heat and momentum. In a well established convective boundary layer, the profile of vertical heat flux should decrease approximately linearly with height. Both resolved-scale<sup>2</sup> vertical heat flux and TKE profiles are shown in Figure 3.2 in increments of 10 minutes from  $t = 0$  minutes to  $t = 1$  hour. Initially, vertical heat flux is zero everywhere due to the initial condition of zero vertical velocity. At  $t = 10$  minutes, vertical heat flux is localized near the surface and exceeds  $0.3 \text{ K m s}^{-1}$ . By  $t = 30$  minutes, initial transient behavior in vertical heat flux relaxes as the convective boundary layer becomes more well established and the heat flux profile takes on a linearly decreasing trend with height. Profiles for subsequent times agree closely with the profile at  $t = 30$  minutes, indicating that the convective boundary layer is near fully established by 30 minutes. Note that the TKE profiles in Figure 3.2 indicate that energy-containing eddies in the upper boundary layer continue to develop through  $t = 1$  hour, as TKE increases in the upper boundary layer from  $\sim 0.7 \text{ m}^2 \text{s}^{-2}$  at  $t = 30$  minutes to  $\sim 1.1 \text{ m}^2 \text{s}^{-2}$  by  $t = 1$  hour. Thus 1 hour of model spin-up time was chosen to adequately allow for development of the convective boundary layer and resolved scales of turbulence.

## 3.2 Gas phase simulations

### 3.2.1 Chemical mechanism

In Chapter 4, we evaluate the impact of emissions spatial heterogeneity on gas phase reactions with a particular focus on ozone production. We select the chemical mechanism Carbon-Bond Mechanism-Z (CBMZ) for gas phase photochemical reactions (Zaveri and Peters 1999). CBMZ models both inorganic and organic compounds prevalent in anthropogenic and biogenic emissions. CBMZ allows computationally efficient calculation of over 100 reactions across dozens of chemical species. This is possible due to the model’s “lumped-structure” approach to sorting similar organic compounds by their carbon bond structure (e.g., alkanes, carbonyls, etc.). This reduces the need for tracking large volumes of organic species and reactions. Despite simplifications to the organic chemistry mechanism, CBMZ has been shown to accurately represent concentrations of compounds of primary interest for atmospheric chemistry applications (e.g.,  $\text{O}_3$ ,  $\text{NO}_x$ , etc.) (Zaveri and Peters 1999).

---

<sup>2</sup>Ideally, one would evaluate total (resolved + parameterized) vertical heat flux and total TKE. WRF does not provide output for SGS quantities, so it would be necessary for one to modify the codebase to allow exporting these additional data.

### 3.2.2 Initial conditions and emissions

Table 3.1: Gas phase emissions and initial conditions. Table adapted from N. Riemer, M. West, et al. 2009 with permission.

Species	Symbol	Initial Mole Fraction (ppb)	Emissions ( $\text{nmol m}^{-2} \text{s}^{-1}$ )
Nitric oxide	NO	0.1	31.8
Nitrogen dioxide	NO <sub>2</sub>	1.0	1.67
Nitric acid	HNO <sub>3</sub>	1.0	
Ozone	O <sub>3</sub>	50.0	
Hydrogen peroxide	H <sub>2</sub> O <sub>2</sub>	1.1	
Carbon monoxide	CO	21	291.3
Sulfur dioxide	SO <sub>2</sub>	0.8	2.51
Ammonia	NH <sub>3</sub>	0.5	6.11
Hydrogen chloride	HCl	0.7	
Methane	CH <sub>4</sub>	2200	
Ethane	C <sub>2</sub> H <sub>6</sub>	1.0	
Formaldehyde	HCHO	1.2	1.68
Methanol	CH <sub>3</sub> OH	0.12	0.28
Methyl hydrogen peroxide	CH <sub>3</sub> OOH	0.5	
Acetaldehyde	ALD2	1.0	0.68
Paraffin carbon	PAR	2.0	96
Acetone	AONE	1.0	1.23
Ethene	ETH	0.2	7.2
Terminal olefin carbons	OLET	$2.3 \cdot 10^{-2}$	2.42
Internal olefin carbons	OLEI	$3.1 \cdot 10^{-4}$	2.42
Toluene	TOL	0.1	4.04
Xylene	XYL	0.1	2.41
Lumped organic nitrate	ONIT	0.1	
Peroxyacetyl nitrate	PAN	0.8	
Higher organic acid	RCOOH	0.2	
Higher organic peroxide	ROOH	$2.5 \cdot 10^{-2}$	
Isoprene	ISOP	0.5	0.23
Alcohols	ANOL		3.45

Gas phase initial conditions and emissions are chosen to represent species and concentrations typical of an urban plume and are adopted from N. Riemer, M. West, et al. 2009. The authors determined gas phase concentrations and emission rates via the 1987 Southern California Air Quality Study (SCAQS) data set which contains measurements of both gas phase species and particulate matter mass concentrations collected at multiple sites across the Los Angeles basin (Zaveri, Easter, et al. 2008). Table 3.1 contains all gas phase initial conditions and emission rates. Empty entries signify zero concentrations or emission rates. To allow

for simulation spin-up, all emission rates are set zero during the first hour of simulations. Subsequently, emitted compounds are released only at the surface and at a constant rate as specified in Table 3.1 for the remainder of the simulation.

### 3.3 Multiphase simulations

#### 3.3.1 Chemical mechanism

Chapter 5 presents simulation results where both gas phase chemistry and aerosol processes (e.g., coagulation, gas-particle partitioning, etc.) are modeled. Both gas phase and aerosol chemistry is represented using the Model for Simulating Aerosol Interactions and Chemistry (MOSAIC) (Zaveri, Easter, et al. 2008). MOSAIC was developed by the authors of CBMZ, and it should be noted that CBMZ is included a sub-model within MOSAIC for handling gas phase chemistry. For aerosol chemistry, MOSAIC simulates dynamic gas-particle partitioning and phase-dependent thermodynamic equilibrium. A key challenge for modeling aerosol chemistry is that the coupled system of solid-liquid phase reactions that govern aerosol thermodynamic equilibrium is often numerically stiff due to the rate of reactions varying over large timescales. Often, chemical mechanisms solve such stiff systems in a computationally expensive manner either by iterative techniques or by directly minimizing the Gibbs Free energy of the system. MOSAIC takes an alternative approach whereby the system of equilibrium reactions is reformulated as a pseudo-transient system. This recasts the system as ordinary differential equations, for which standard numerical techniques are used to integrate and obtain equilibrium steady state solutions. This approach makes MOSAIC computationally efficient while maintaining good agreement when benchmarked against numerically rigorous and accurate models (Zaveri, Easter, et al. 2008).

#### 3.3.2 Aerosol representation

We use the Particle Monte Carlo (PartMC) model for particle-resolved representation of aerosols (N. Riemer, M. West, et al. 2009). In PartMC, aerosol particles are represented via a set of computational particles with appropriate multiplicity to represent the desired aerosol population. Each computational particle is allowed to compositionally vary due to aerosol processes (e.g., coagulation, condensation, gas-particle partitioning, etc.), thus allowing the representation of a far greater degree of compositional diversity and aerosol properties than sectional or modal based aerosol models. PartMC is a box model, meaning that within computational

grid cells, the position of computational particles is not tracked. Instead, processes such as coagulation are handled in the probabilistic manner of Gillespie 1975. PartMC is coupled with MOSAIC, thereby leveraging the computational efficiency and accuracy of each model in allowing full representation of an aerosol state (number and mass concentration, per-particle composition) under aging due to both aerosol physical processes and chemical reactions.

Curtis, Nicole Riemer, and Matthew West 2017 coupled PartMC-MOSAIC with WRF for a single column model of the planetary boundary layer. The authors developed approaches for modeling the turbulent diffusion and dry deposition of aerosol particles as stochastic processes. The resulting modeling framework, WRF-PartMC-MOSAIC, is extended here for use with 3D LES.

For WRF-PartMC-MOSAIC-LES, we use 100 computational particles per grid cell for a total of 100 million computational particles throughout the domain at initialization. This value was chosen to balance computational efficiency and storage demands alongside numerical representability – too few computational particles will result in random noise for aerosol population properties due to the stochastic nature of the PartMC model.

### 3.3.3 Initial conditions and emissions

Initial conditions and emissions of gas phase species match those discussed in Section 3.2.2 and are displayed in Table 3.1. Similarly, aerosol initial conditions and emission rates are adopted from N. Riemer, M. West, et al. 2009, who based aerosol distributions, composition, and emission rates off measurements collected as part of the SCAQS campaign in the Los Angeles valley. Aerosol initial conditions and emission properties are summarized in Table 3.2. Size distributions for aerosol initial conditions and emissions are shown in Figure 3.3 and Figure 3.4, respectively. The aerosol initial condition is comprised of two modes, including a Aitken mode and accumulation mode. Each mode is an equal mixture of 50% ammonium sulfate and 50% primary organic aerosol (POA). Three emission modes are chosen to represent emissions from various urban combustion sources, including cooking, diesel vehicles, and gasoline vehicles. The cooking emission mode is comprised of 100% POA and the diesel and gasoline modes are each a mixture of POA and black carbon (BC).

Table 3.2: Aerosol emissions and initial conditions. Table adapted from N. Riemer, M. West, et al. 2009 with permission.

Initial/Background	$N$ ( $\text{m}^{-3}$ )	$D_{\text{gn}}$ ( $\mu\text{m}$ )	$\sigma_g$	Composition by Mass
Aitken Mode	$3.2 \cdot 10^9$	0.02	1.45	50% $(\text{NH}_4)_2\text{SO}_4$ , 50% POA
Accumulation Mode	$2.9 \cdot 10^9$	0.116	1.65	50% $(\text{NH}_4)_2\text{SO}_4$ , 50% POA
Emissions	$E$ ( $\text{m}^{-2} \text{s}^{-1}$ )	$D_{\text{gn}}$ ( $\mu\text{m}$ )	$\sigma_g$	Composition by Mass
Meat cooking	$9 \cdot 10^6$	0.086	1.9	100% POA
Diesel vehicles	$1.6 \cdot 10^8$	0.05	1.7	30% POA, 70% BC
Gasoline vehicles	$5 \cdot 10^7$	0.05	1.7	80% POA, 20% BC

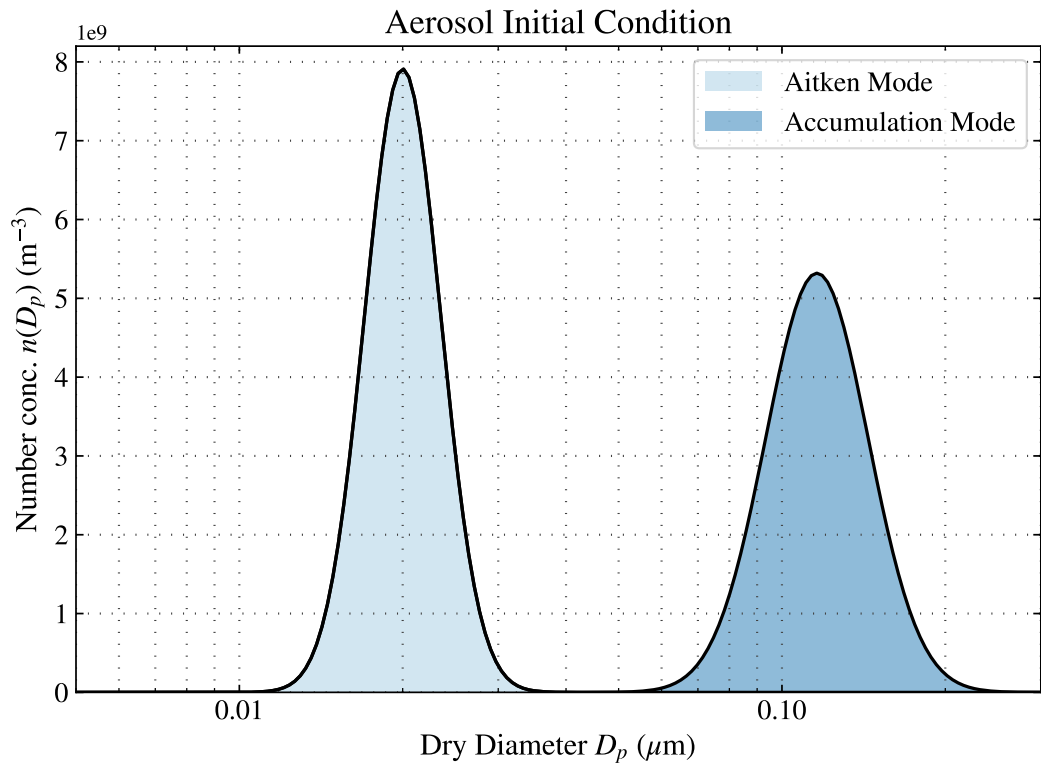


Figure 3.3: Aerosol initial condition size distributions.

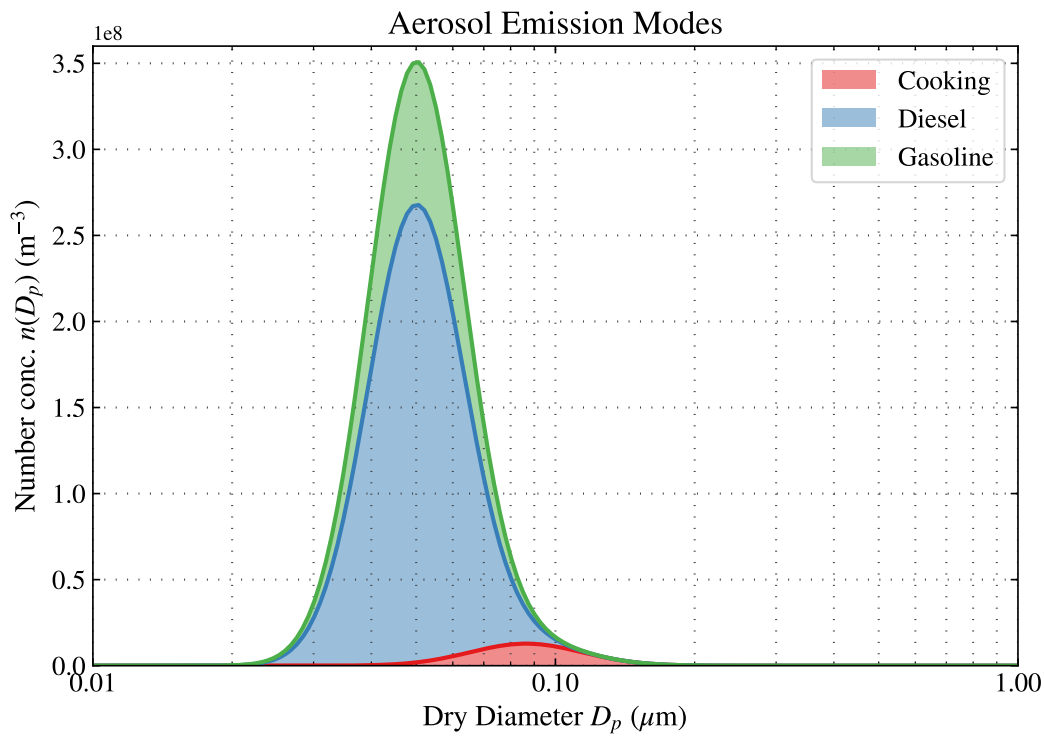


Figure 3.4: Aerosol emission size distributions.

# Chapter 4

## Impacts of emissions spatial heterogeneity on gas-phase reactions

This chapter investigates the impacts of gas phase emissions and associated chemical reactions on the production of ozone in the planetary boundary layer. The effect emissions spatial heterogeneity on ozone production is explored across numerous emissions scenarios with ranging emissions spatial heterogeneity. We find that for the most heterogeneous emissions case, ozone production is reduced in the mid-boundary layer by up to  $\sim 13\%$ . We also evaluate the spatial heterogeneity of ozone and its precursor compounds  $\text{NO}_x$  and volatile organic compounds (VOCs) after they are emitted. We find that  $SH$  varies considerably across precursors and also exhibits spatio-temporal variability.

### 4.1 Simulated emissions scenarios

We conduct four simulations in total ranging in emissions spatial heterogeneity from  $SH = 0$  to  $SH = 1$  for precursor species responsible the production of ozone. Emissions scenarios are shown in Figure 4.1. The first simulation, named the uniform base case scenario, is characterized by uniform emissions of all compounds across the computational domain ground level. The uniform base case has a spatial heterogeneity equal to zero. This scenario represents the emissions across a single grid cell in a lower resolution model, such as a regional or global climate model, where emitted species are both uniform and dilute. Thus, results for simulations with higher emissions heterogeneity are compared against the uniform base case to quantify the structural uncertainty in ozone concentrations resulting from the assumption of uniform, dilute emissions characteristic of coarser resolved models that do not adequately resolve the true emissions spatial heterogeneity.

Across the simulated emission scenarios, the area occupied by ground level emissions decreases up to a single grid cell in the case of emissions scenario 3. This scenario is meant to represent a highly localized emissions source and is the maximally heterogeneous case with  $SH = 1$ . The total mass per unit time emitted

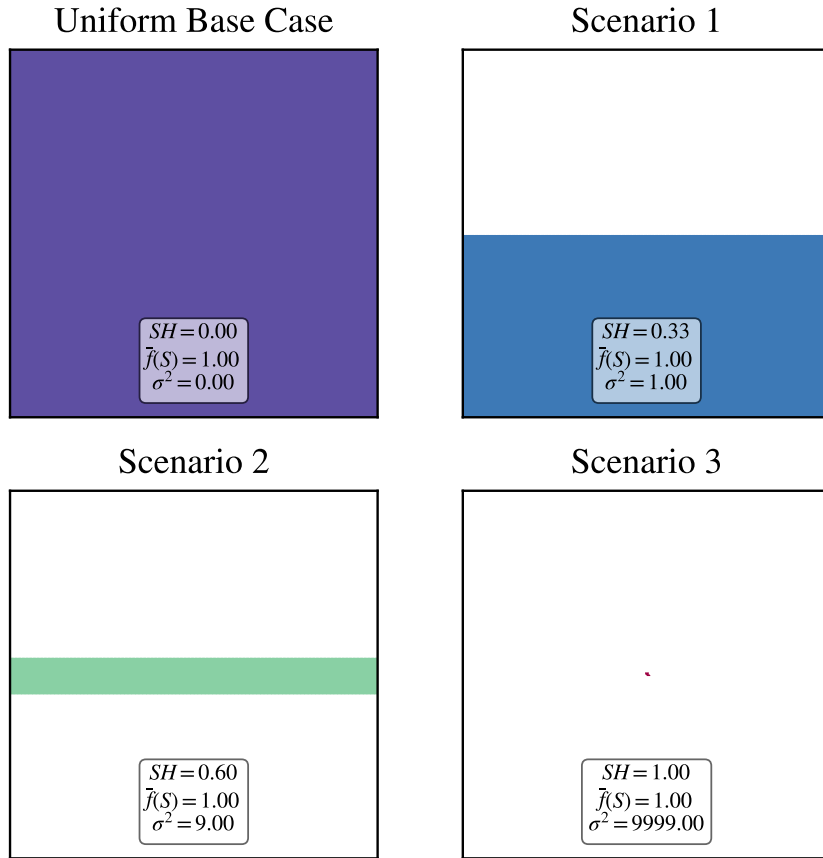


Figure 4.1: Emissions scenarios for ozone production simulations. The spatial heterogeneity of each emission scenario is listed in the lower portion of each scenario alongside domain mean and variance.

across each scenario remains the same, thus the emission rate for high spatial heterogeneity cases must be scaled by the ratio between the area occupied by emissions in the uniform base case and the area emissions occupy in the corresponding emissions scenario. For example, the area of emissions in emissions scenario 3 is  $0.01 \text{ km}^2$  while the area occupied by emissions in the uniform base case is  $100 \text{ km}^2$ , resulting in an emissions rate scaling factor of  $100/0.01 = 10,000$ .

Each simulation was run for a total of 6 hours beginning at 9:00 AM LT and ending at 3:00 PM LT. The first hour of each simulation allows spin up and development of the PBL. Afterward, emissions occur at a constant rate for the remainder of each simulation.

## 4.2 Results

Maybe a little summary of what the sub-sections are here before launching into results?

### 4.2.1 Ozone cross sections

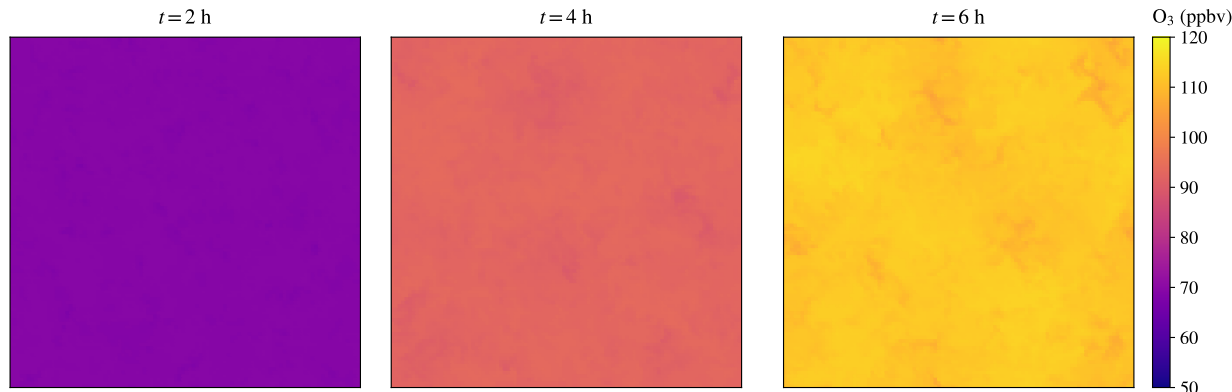


Figure 4.2: Ozone cross sections in the x-y plane at 2 hour intervals in the middle of the PBL ( $z \sim 500 \text{ m}$ ) for the uniform base case.

In order to visualize the spatial heterogeneities present in ozone throughout each simulation, cross sections of ozone concentrations in the x-y plane were plotted for each emissions scenario. Cross sections were selected at a vertical level corresponding to the approximate middle of the PBL ( $z \sim 500 \text{ m}$ ) and were plotted at regular, 2 hour intervals.

Ozone cross section plots for the uniform base case are shown in Figure 4.2. Ozone concentrations are displayed as molar fractions in parts per billion by volume (ppbv). Throughout each snapshot, the distribution of ozone is shown to be nearly uniform with minimal concentration gradients. Ozone concentrations steadily increase throughout the course of the simulation, reaching in excess of 110 ppbv by  $t = 6 \text{ h}$ .

Ozone cross sections for emission scenarios 1–3 are shown in Figures 4.3–4.5, respectively. By  $t = 2 \text{ h}$ , ozone concentrations have risen from their initial condition of 50 ppbv to a nearly uniform 60 ppbv in areas distant from the region where the emissions plume passes through. Approaching the area surrounding the plume, ozone concentrations are lower at  $\sim 50 \text{ ppbv}$ , indicating that very little ozone production occurs in the immediate vicinity of the emissions plume. This trend increases moving from emissions scenario 1 (Figure 4.3) to emissions scenario 3 (Figure 4.5), where the absence of elevated ozone levels in the central region of the plume is clearly visible.

By  $t = 4 \text{ h}$  and  $t = 6 \text{ h}$ , ozone concentrations have risen in the region immediately surrounding the plume, reaching upwards of 110 ppbv in each scenario by  $t = 6 \text{ h}$ . The region of most efficient ozone production clearly overlaps with the region where the plume is rising through the PBL; however, for the highest spatial

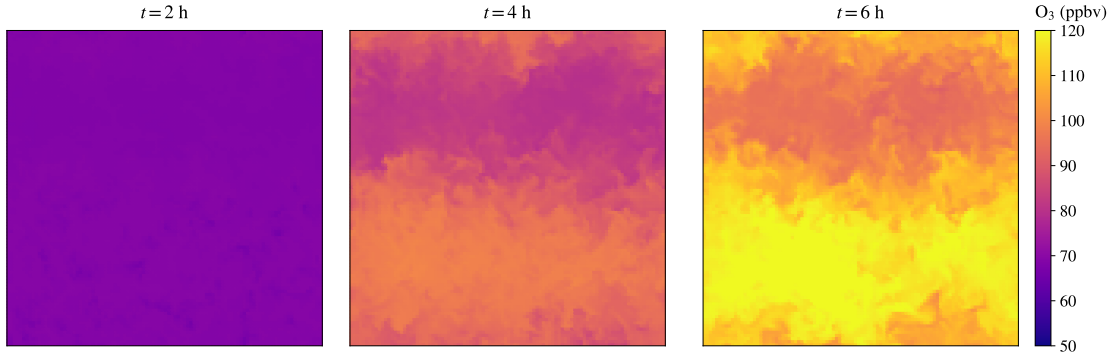


Figure 4.3: Ozone cross sections in the x-y plane at 2 hour intervals in the middle of the PBL ( $z \sim 500$  m) for emissions scenario 1.

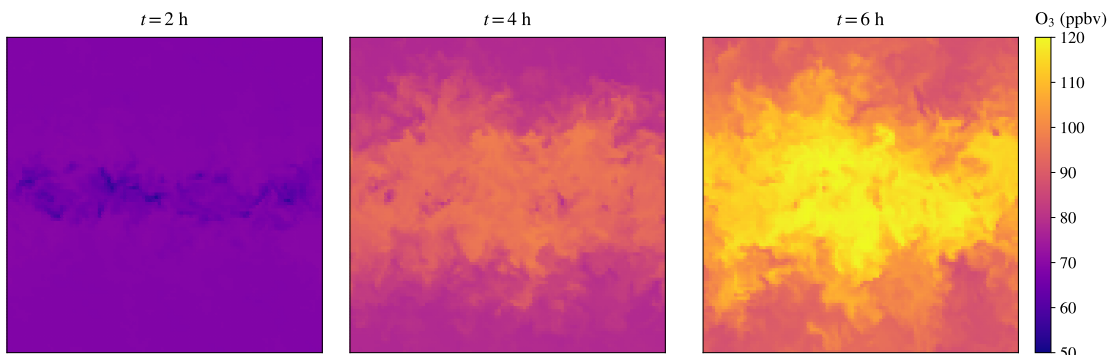


Figure 4.4: Ozone cross sections in the x-y plane at 2 hour intervals in the middle of the PBL ( $z \sim 500$  m) for emissions scenario 2.

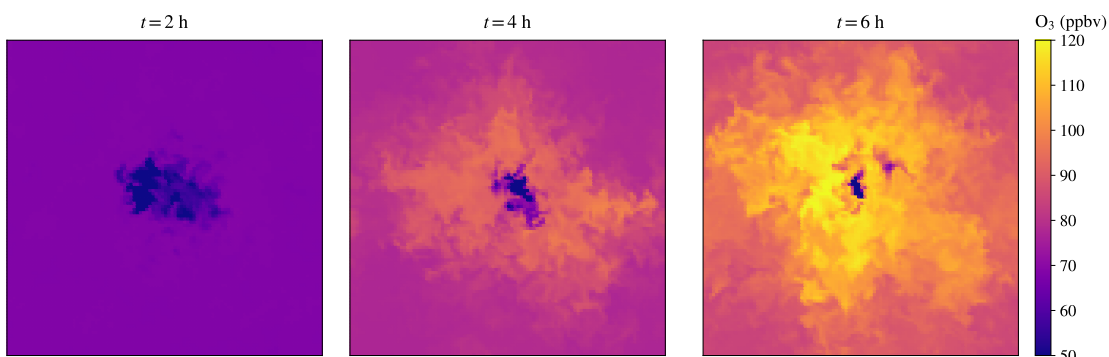


Figure 4.5: Ozone cross sections in the x-y plane at 2 hour intervals in the middle of the PBL ( $z \sim 500$  m) for emissions scenario 3.

heterogeneity emissions scenario, scenario 3 (Figure 4.5), we find that ozone concentrations are significantly depressed in the immediate vicinity of the plume. This points to the non-linear nature of ozone production and its dependence on the relative abundance of  $\text{NO}_x$  and VOCs.

#### 4.2.2 Spatio-temporal trends in ozone and its precursors

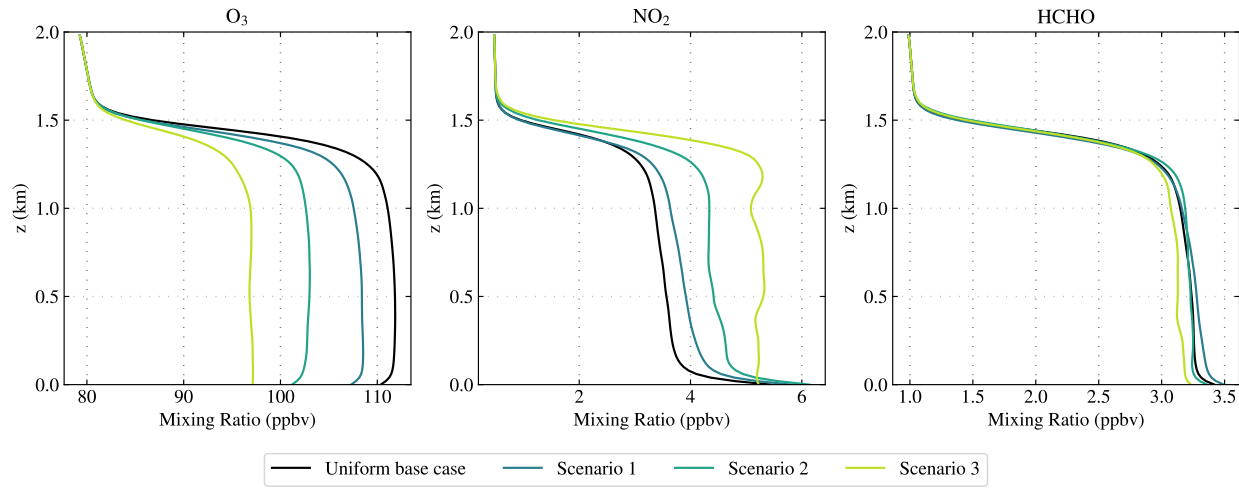


Figure 4.6: Vertical profiles at  $t = 6$  h for ozone, NO<sub>2</sub>, and HCHO (left to right) for each emissions scenario. Each vertical profile indicates the species mean concentration when horizontally averaged at each vertical level.

Vertical profiles at  $t = 6$  h for ozone, NO<sub>2</sub>, and HCHO (formaldehyde) across each emissions scenario are shown in Figure 4.6. For each plot, the vertical profile was computed by determining the horizontal average across the domain of each compound and for each vertical level. NO<sub>2</sub> is displayed alongside ozone to evaluate whether NO<sub>x</sub> titration is occurring—at high NO concentrations, there is a net conversion of ozone to NO<sub>2</sub> via



Usually this reaction is balanced by photolysis of NO<sub>2</sub>, however, in emissions plumes with high concentrations of NO, Reaction 4.1 results in a net conversion of ozone to NO<sub>2</sub>. HCHO is chosen as a representative VOC.

We find that mean ozone concentrations are nearly uniform in the PBL for each emissions scenario, with a reduction in mean concentrations from  $\sim 112$  ppbv in the uniform base case to  $\sim 97$  ppbv for emissions scenario 3. By  $t = 6$  h, the boundary layer height has grown to nearly  $z = 1.5$  km, above which point ozone concentrations are nearly identical at  $\sim 80$  ppbv across emissions scenarios. Note the initial condition for ozone is a uniform 50 ppbv throughout the entire domain, indicating that in the absence of additional NO<sub>x</sub> and VOC precursors due to emissions, ozone concentrations rise by approximately 30 ppbv over 6 hours due to ambient precursor concentrations and photolysis reactions.

NO<sub>2</sub> concentrations vary considerably within the boundary layer, with concentrations approaching 6 ppbv

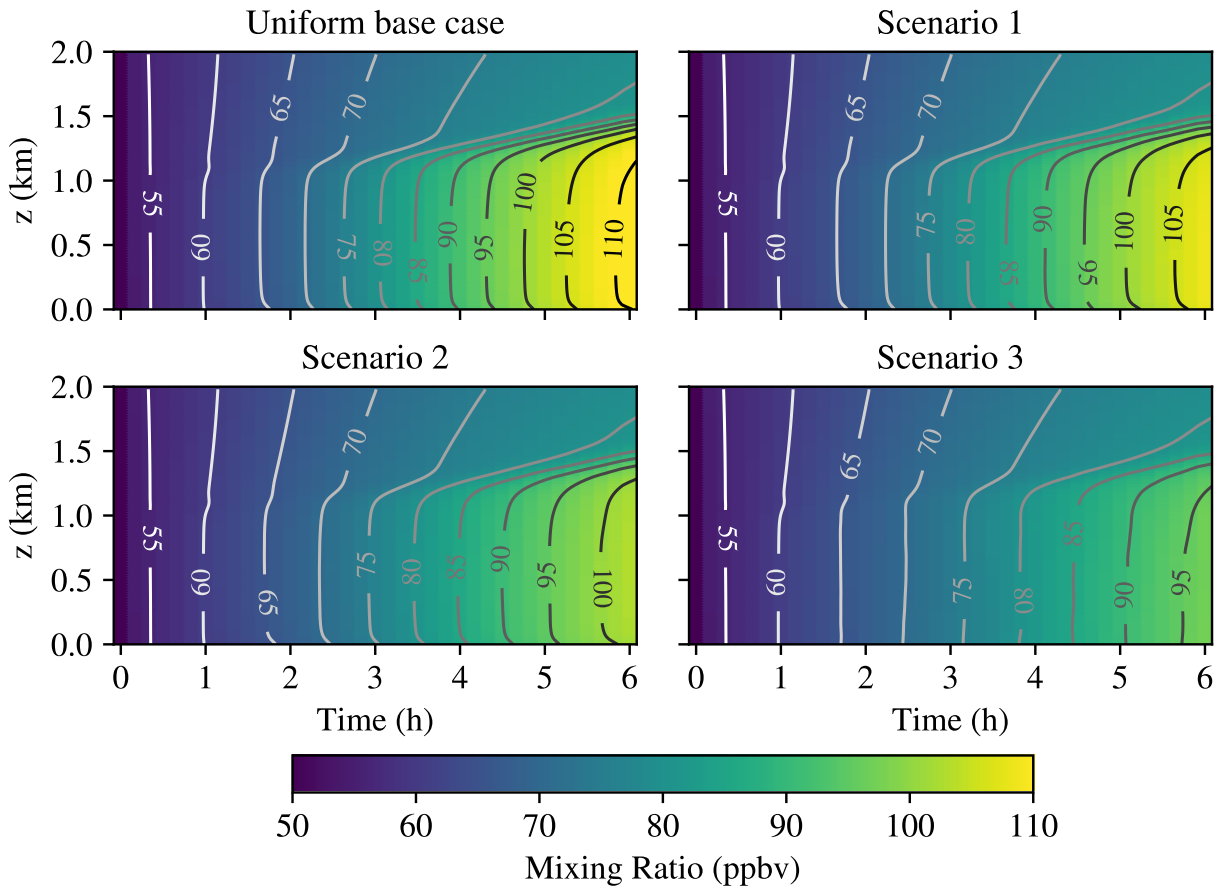


Figure 4.7: Ozone concentration time-height plots for each emissions scenario.

near the surface followed by a slightly decreasing trend in the middle to upper PBL. We find higher NO<sub>2</sub> concentrations as we move from the uniform base case to higher emissions spatial heterogeneity scenarios. We also find that under the highest emissions *SH* scenarios (scenario 2 and 3), the profile of NO<sub>2</sub> is more variable with height.

HCHO concentrations are relatively uniform across each emissions heterogeneity scenario, with concentrations between 3–3.5 ppbv in the PBL. Agreement in the abundance of HCHO across emission scenarios suggest that it is not as sensitive to emissions spatial heterogeneity as NO<sub>x</sub> probably owing to the rate at which it reacts with other species.

Time-height sections of ozone concentrations are shown for each emissions scenario in Figure 4.7. For each time-height figure, the horizontal average concentration of ozone was computed for each vertical level and at time in the simulation output. Isopleths are superimposed on each time-height plot and indicate regions of constant ozone concentrations in increments of 5 ppbv.

During the first hour of each simulation, ozone concentrations gradually increase nearly uniformly from the initial concentration of 50 ppbv to 60 ppbv. Emissions are turned on at  $t = 1$  h, however ozone concentrations for emissions scenarios 1–3 do not appear to appreciably diverge from the uniform base case until  $t \simeq 2$  h and beyond. After this point, ozone concentrations increase in the PBL of each scenario (the PBL height gradually grows throughout the simulation as indicated by the region of highest ozone concentrations due to the constant heat flux at the surface). Ozone concentrations alongside the ozone formation rate are highest in the uniform base case. Note that between hours 5 and 6, ozone concentrations in the PBL increase by approximately 10 ppbv as indicated by isopleths. By comparison, ozone concentrations increase by approximately 5 ppbv for scenario 3 during the same time period.

To quantify the relative difference between ozone production in the uniform base case and each emission scenario, Figure 4.8 displays time-height plots for each emissions scenario where the percent difference between ozone in the uniform base case and each scenario is displayed with superimposed isopleths. Percent difference is calculated as

$$\% \text{ difference} = 100 \times \left( \frac{\overline{[O_3]}(t, z)_{\text{Scenario}} - \overline{[O_3]}(t, z)_{\text{Base case}}}{\overline{[O_3]}(t, z)_{\text{Base case}}} \right), \quad (4.2)$$

where  $\overline{[O_3]}(t, z)_{\text{Scenario}}$  is the horizontally averaged concentration of ozone at time  $t$  and vertical level  $z$  for a particular scenario and  $\overline{[O_3]}(t, z)_{\text{Base case}}$  is the horizontally averaged concentration of ozone at time  $t$  and vertical level  $z$  for the uniform base case.

In Figure 4.8, regions shaded in blue indicate negative percent difference (i.e., the uniform base case contains higher concentrations in a given region) while red indicates positive percent difference. Regions shaded in gray indicate zero percent difference. We find that ozone concentrations for emissions scenario 1 are in good agreement with the uniform base case within the free troposphere during the entire simulation and also in the PBL prior to  $\sim 2$  hours. After this point, ozone concentrations are up to 3% less in the PBL through  $t = 6$  h.

We find similar but heightened trends for ozone concentration percent difference for emissions scenarios 2 and 3, respectively. For scenario 2, ozone concentrations are up to 8% less in the PBL through  $t = 6$  h and are reduced by up to  $\sim 13\%$  for scenario 3.

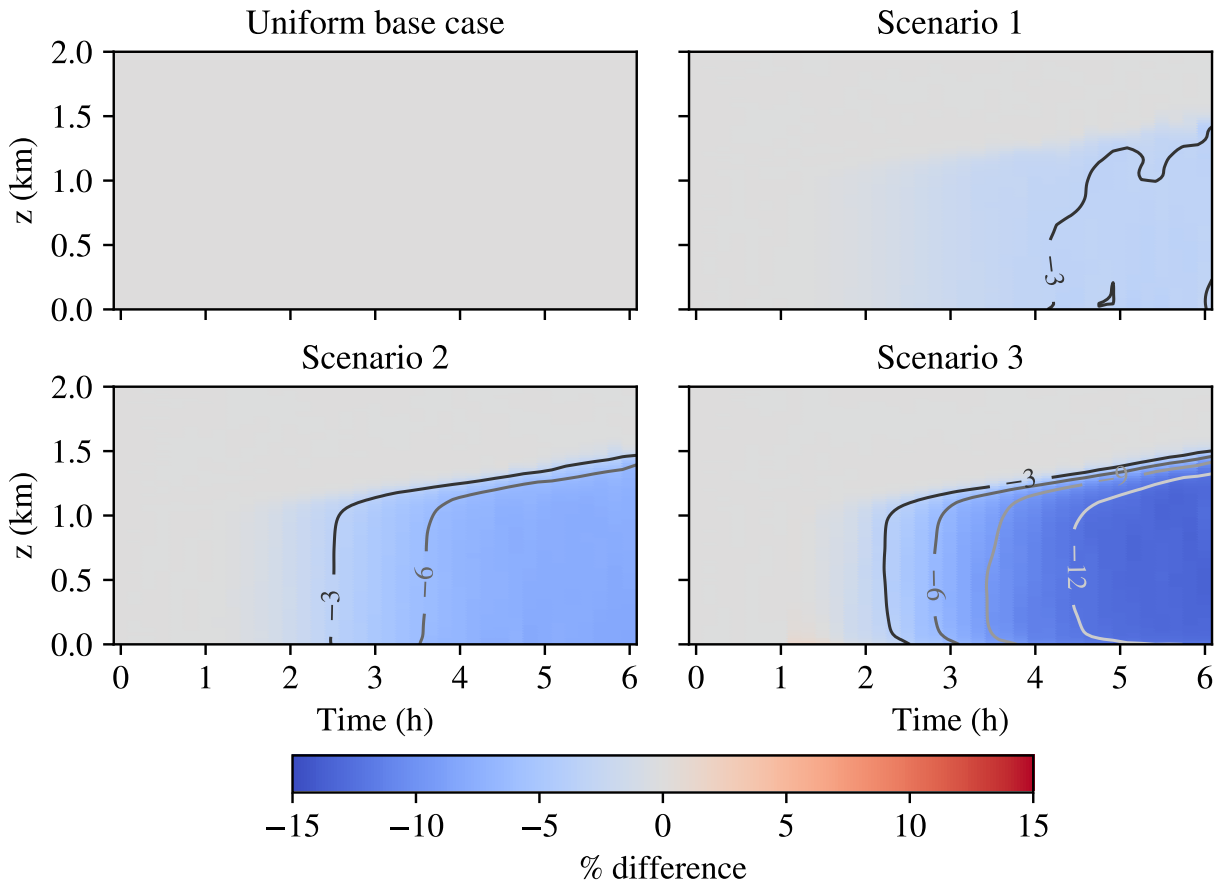


Figure 4.8: Time-height plots of ozone percent difference for each emissions scenario.

#### 4.2.3 Spatial heterogeneity in the atmosphere of ozone and its precursors

In addition to the spatial heterogeneity of each emission pattern as shown in Figure 4.1, once gas phase species are emitted from the surface, their atmospheric distribution will be influenced by the emissions pattern heterogeneity, the strength of mixing, and chemical reactions that alter the abundance of compounds. We refer to the spatial heterogeneity of a gas phase species in the atmosphere as the species' *field* spatial heterogeneity.

Figure 4.9 shows time-height plots of the field spatial heterogeneity for NO (top), HCHO (middle), and ozone (bottom) for the uniform base case. Field  $SH$  is computed for horizontal cross sections of the domain at each vertical level and each time. Regions filled with dark blue correspond to low field  $SH$  while regions in green and yellow indicate high field  $SH$ . In Figure 4.9, the field  $SH$  of each compound is very low. After  $t = 1$  h, NO field  $SH$  is  $\sim 0.01$  within the PBL. HCHO field  $SH$  is  $\sim 0.001$  within the PBL following the release of emissions at  $t = 1$  h, with slightly higher values of 0.01 near the upper PBL developing after  $t = 2$

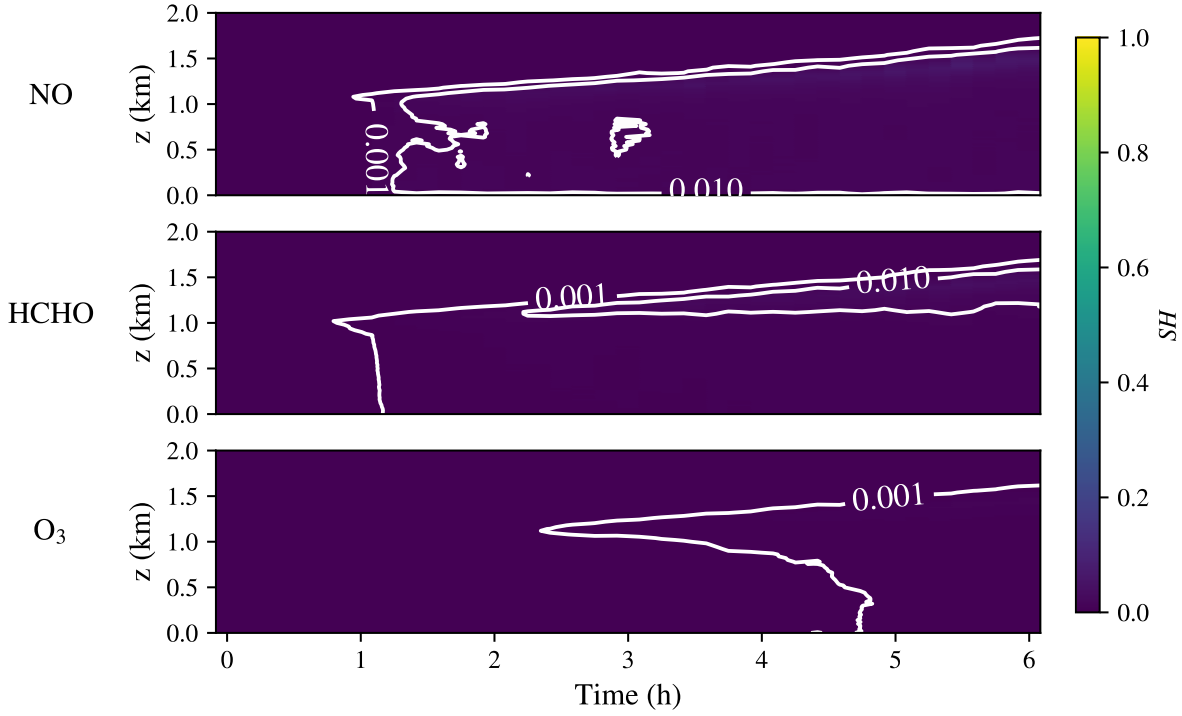


Figure 4.9: Time-height plot of field  $SH$  for  $O_3$ ,  $NO_x$ , and  $HCHO$  in the uniform base case.  $SH$  value contours are shown in grayscale for each subplot.

h. Ozone field  $SH$  is the lowest of the three compounds, with values of 0.001 developing in the upper PBL after  $t = 2$  h and extending to the surface by  $t = 5$  h.

Similarly, Figure 4.10 shows time-height plots for ozone and its precursors for emissions scenario 1. Recall that the emissions  $SH$  for scenario 1 is 0.33. Field  $SH$  for all species is lower than the emissions  $SH$  (as we expect due to atmospheric processes that disperse, dilute, and alter the concentration of each compound). As emissions begin at  $t = 1$  h, the field  $SH$  of NO is  $\sim 0.1$  within the PBL and increases to 0.2 after approximately 2 hours. Around  $t = 5$  h, the field  $SH$  of NO decreases back down to 0.1 within the PBL. Following the release of emissions at  $t = 1$  h, HCHO field  $SH$  is 0.05, increasing to 0.1 by approximately 2 hours and 30 minutes where it remains for the duration of the simulation. Similar to field  $SH$  for the uniform base case, ozone exhibits the lowest field  $SH$  of all three species, with values of 0.001 from  $t = 1$  h to  $t = 3$ , afterward increasing to 0.01.

We find similar trends to scenario 1 in the field  $SH$  of ozone and its precursors for emissions scenario 2 as shown in Figure 4.11. Recalling that the emissions  $SH$  of scenario 2 is 0.60, we find that the field  $SH$  of NO and HCHO correspondingly increase compared to scenario 1. Following emissions at  $t = 1$  h, the field

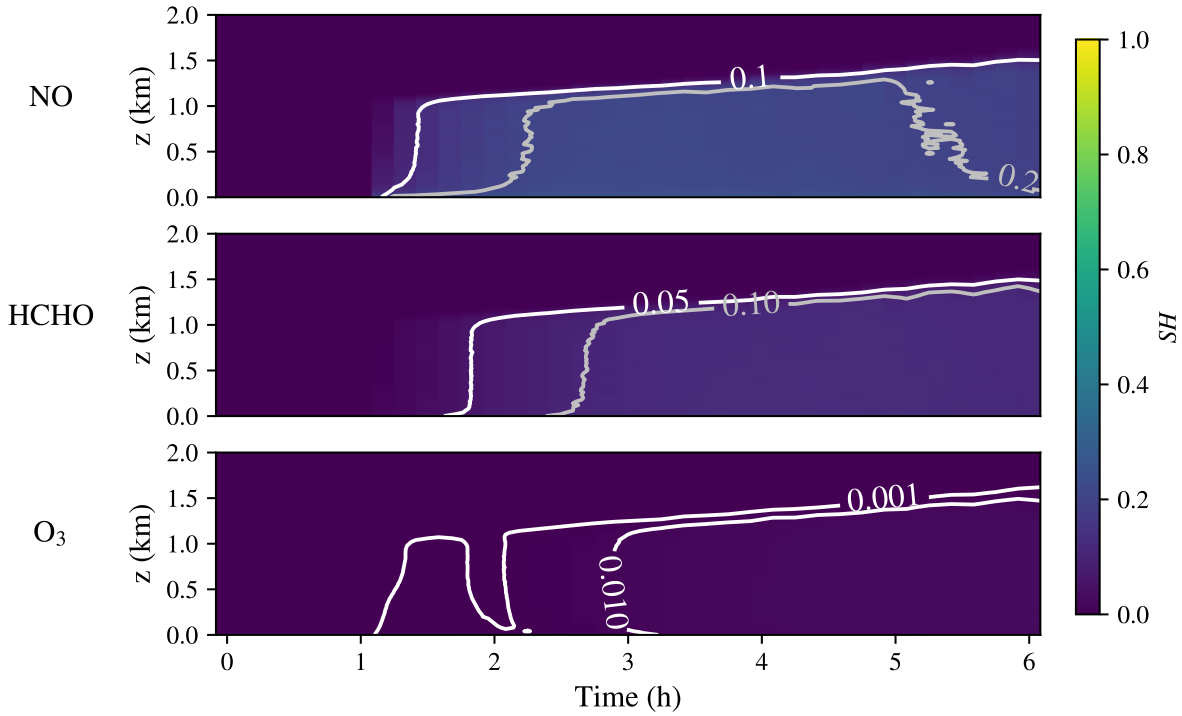


Figure 4.10: Time-height plot of field  $SH$  for  $O_3$ ,  $NO_x$ , and  $HCHO$  in emissions scenario 1.  $SH$  value contours are shown in grayscale for each subplot.

$SH$  of NO in the PBL increases to 0.3 over nearly the entire height PBL except for near the surface where the field  $SH$  reaches 0.4. The field  $SH$  of HCHO increases to 0.15 by  $t = 3$  h, where it remains through the duration of the simulation. The pattern of field  $SH$  for ozone closely matches its behavior noted for scenario 1—from  $t = 1$  h to  $t = 3$  h, ozone field  $SH$  is of order 0.001, increasing to 0.01 afterwards.

Figure 4.12 shows the field  $SH$  of ozone and its precursors for emissions scenario 3. Scenario 3 posses the highest emissions spatial heterogeneity,  $SH = 1$ . As a result, the field  $SH$  of both NO and HCHO are markedly higher compared to previous scenarios. Field  $SH$  of NO varies both spatially and temporally for scenario 3. Following the release of emissions at  $t = 1$  h, we find a high field  $SH$  of 0.8 near the surface that persists for the duration of the simulation. Moving up in the PBL, field  $SH$  ranges from 0.4 to 0.6. From  $t = 1$  h to  $t = 2$  h, the region of high field  $SH$  at 0.6 is localized near the surface. Following this point, this high field  $SH$  region extends upwards to the top of the PBL from  $t = 2$  h to  $t = 3$  h. After this point, field  $SH$  lowers back down to 0.4 over most of the PBL. Field  $SH$  of HCHO is relatively uniform through the PBL and increases following emissions to 0.2 by  $t = 3$  h where it remains for the duration of the simulation. Similar to the field  $SH$  of ozone discussed for scenarios 1 and 2, ozone exhibits a very similar pattern for scenario

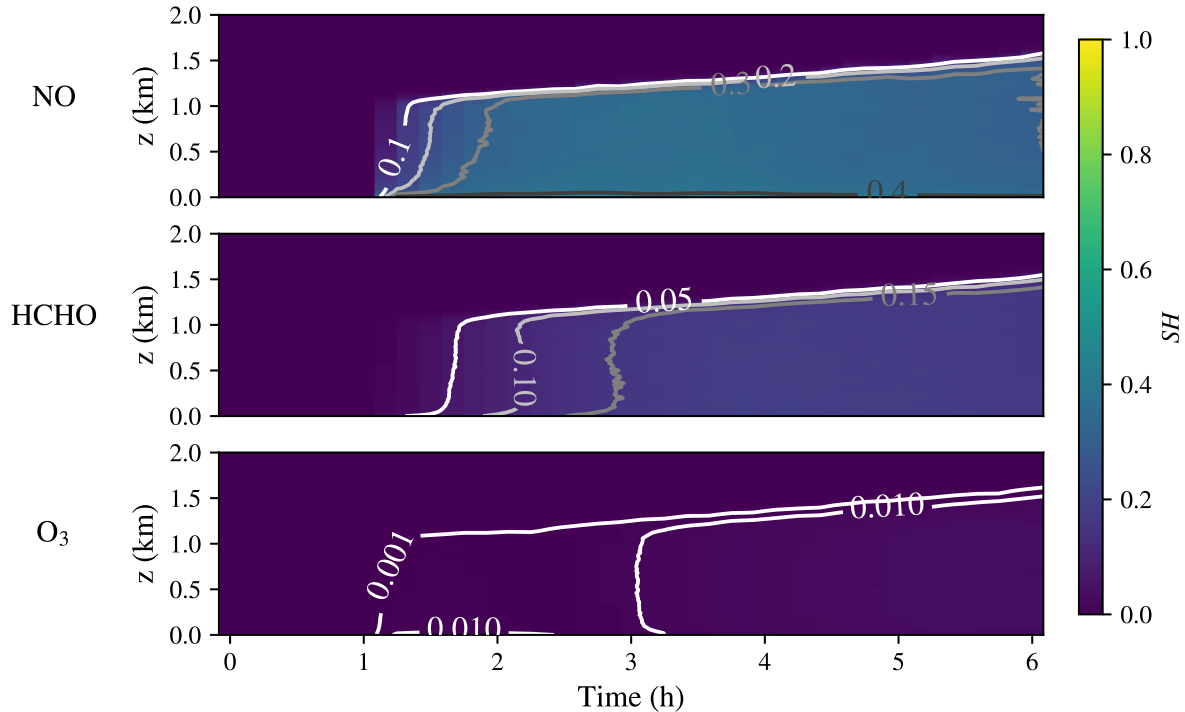


Figure 4.11: Time-height plot of field  $SH$  for  $O_3$ ,  $NO_x$ , and  $HCHO$  in emissions scenario 2.  $SH$  value contours are shown in grayscale for each subplot.

3–from  $t = 1$  h to  $t = 3.5$  h, ozone field  $SH$  is of order 0.001, increasing to 0.01 afterwards.

Decrease in NO field sh seems to occur around the same time that HCHO field sh increases, shortly followed by ozone. My theory is that this may point to changes in ozone production efficiency as the relative abundance of  $NO_x$  changes due to continued emissions and perhaps the VOCs are reacting more to produce more ozone (thus increasing the conc. and coupling the field sh of ozone to VOC field sh?) Its also the case that there ARE aerosols in these simulations and that presents an important pathway for the removal of  $NO_x$  via nitric acid to form aerosol nitrate and nitric acid deposition.

### 4.3 Discussion

This either goes here or in the introduction..

- Worth noting at some point past studies that have evaluated the production of ozone in LES as well as some studies that investigate the impacts of spatial het. on ozone production (Initial studies investigated idealized interactions between turbulence and ozone chemistry in the PBL, more recent studies have branched into region-specific studies to investigate impacts of spatially heterogeneous emissions and

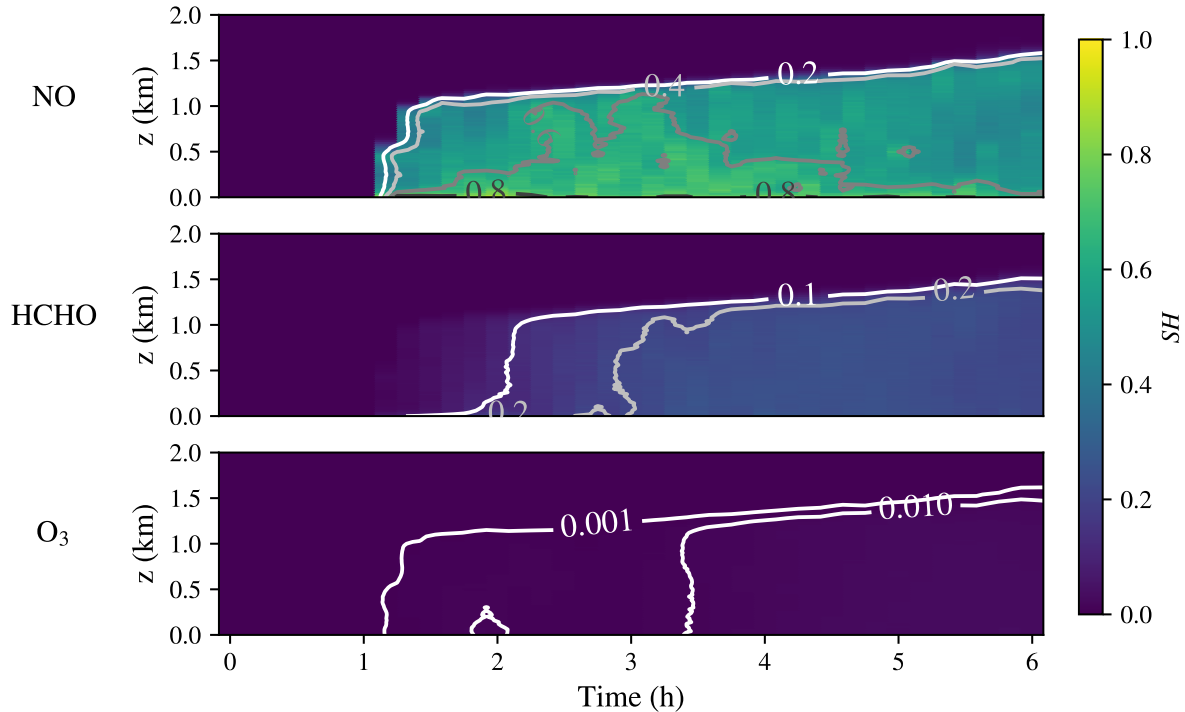


Figure 4.12: Time-height plot of field  $SH$  for  $O_3$ ,  $NO_x$ , and  $HCHO$  in emissions scenario 3.  $SH$  value contours are shown in grayscale for each subplot.

turbulence-chemistry interactions on local ozone production).

- Schumann 1989 Idealized LES of boundary layer - investigate binary reactions (such as those typical of ozone production) with varying reaction rates. For rates typical of ozone-nox reactions, the mechanism is significantly impacted by turbulence.
- Sykes, Henn, et al. 1992 Idealized LES of boundary layer - investigate turbulence chemistry interactions on ozone chemistry, particularly focused on the removal mechanism oxidizing NO to  $NO_2 + O_2$ . Find that the production rate of  $NO_2$  is highly dependent on the turbulent mixing of the plume. They show that the turbulence segregation coefficient can be approximated as uniform in a emitted plume.
- Auger and Legras 2007 (seems very similar to what I am doing here) LES of PBL over  $10 \times 10$  km domain. Indicate that segregation is strongest in the first two hours - after 3 hours segregation is largely reduced due to efficient mixing in the PBL.
- Zhong, Cai, and Bloss 2015 Similar to Zhong et al 2017, find that ozone production rate is reduced due to incomplete mixing.

- Zhong, Cai, and Bloss [2017](#) LES study of O<sub>3</sub>-NO<sub>x</sub>-VOC chemistry in urban street canyons characterized by high spatial variability in concentration gradients. NO<sub>x</sub> and HO<sub>x</sub> radicals were consumed to produce NO<sub>2</sub> and O<sub>3</sub>. Segregation effect due to incomplete mixing reduces the production of NO<sub>2</sub>.
- Y. Wang, Ma, Muñoz-Esparza, C. W. Y. Li, et al. [2021](#)
- Y. Wang, Brasseur, and T. Wang [2022](#) Similar to wang 2023
- Y. Wang, Ma, Muñoz-Esparza, Dai, et al. [2023](#) Use of LES (WRF-Chem LES [what chem mechanism?](#)) for urban (Hong Kong) emissions compared against mesoscale simulations, show that NO<sub>x</sub> is underestimated and O<sub>3</sub> overestimated in mesoscale simulations when compared to LES, attributed to the higher spatial resolution of emissions and explicitly resolving turbulent transport.

# Chapter 5

## Impacts of emissions spatial heterogeneity on aerosol properties and CCN activity

This chapter presents results for the impacts of emissions spatial heterogeneity on aerosol properties, including changes to the aerosol size distribution, composition, mixing state, and CCN activity. We begin with a set of simplified simulations to isolate the effect of spatial heterogeneity on an important aerosol process, coagulation. Subsequently, we present simulation results for full multiphase (gas and aerosol) chemistry runs and discuss changes to aerosol properties and CCN activity. We find that under high emissions spatial heterogeneity, up to 25% more CCN activate in the upper boundary layer for supersaturations in the range  $S = 0.3\%$  to  $S = 0.6\%$ . The effects of ammonium on CCN activity are also explored, as we find that high spatial heterogeneity scenarios allow more nitrate in the aerosol phase due to the availability of free ammonium.

### 5.1 Idealized coagulation simulations

Prior to discussing simulations utilizing the full multiphase chemical mechanism for aerosols and chemistry, we first focus our discussion on the impact of spatial heterogeneity on aerosol number concentration due to coagulation. Coagulation is a primary mechanism for aerosol aging and its rate scales with the square of the number concentration of particles, thus making it an important aerosol process for which to evaluate the impacts of spatial heterogeneity.

#### 5.1.1 Simulation scenarios

Here we investigate the modification to the rate of coagulation under numerous spatial heterogeneity scenarios. We run a total of 6 simulations for a range of  $SH$  scenarios shown in Figure 5.1. As with gas phase simulations in Chapter 4, the concentration of atmospheric constituents (here aerosol particle number concentration)

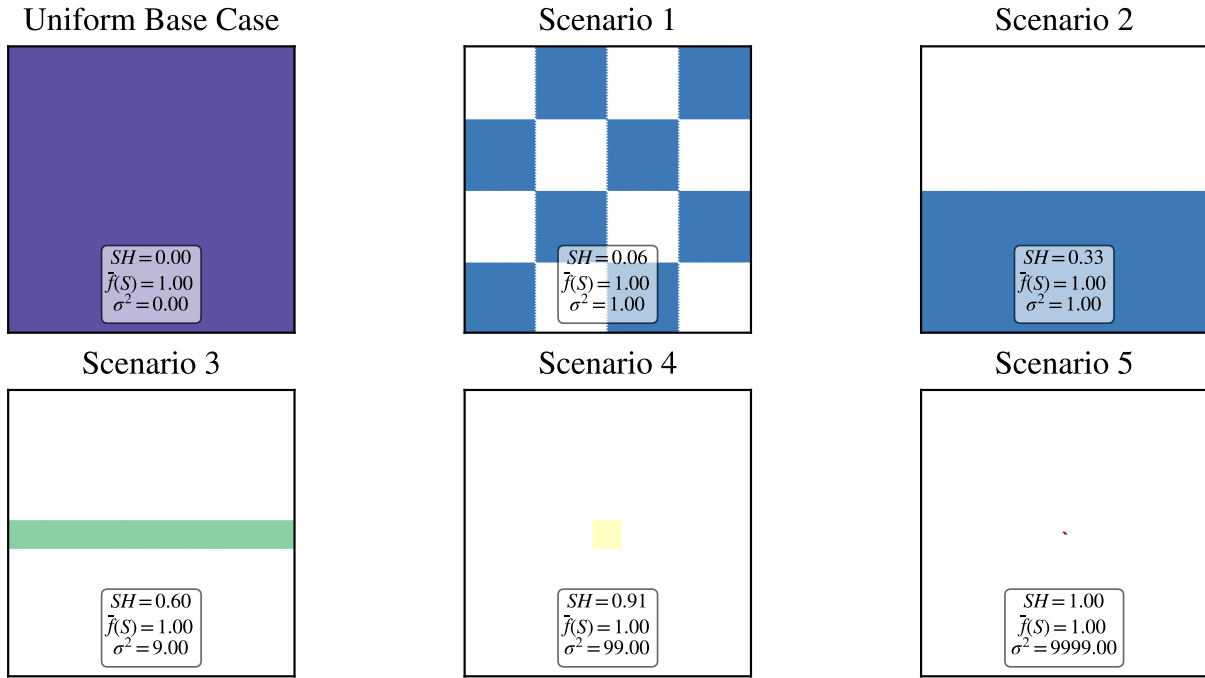


Figure 5.1:  $SH$  scenarios for ideal coagulation simulations.

must be scaled within the  $SH$  scenario region by the ratio of the area of the uniform base case and the area occupied by the  $SH$  pattern. For example, the aerosol number concentration in the central region of scenario 5 is a factor of 10,000 higher than in the uniform base case.

Note that the setup of these simulations differs from all other simulations discussed in this thesis. Chemistry is turned off primarily for computational efficiency as, here, we are simply interested in changes to the number concentration rather than changes to aerosol composition. Instead of using initial conditions that are uniform throughout the domain, here the aerosol initial condition is set by the chosen  $SH$  scenario for each vertical level in the domain (i.e., the pattern extends vertically throughout the domain). Additionally, emissions are turned off such that only coagulation is responsible for changes to aerosol number concentration.

### 5.1.2 Results

Figure 5.2 show how the total number concentration of aerosol particles decreases due to coagulation under each  $SH$  scenario. For each scenario, we compute the average number concentration at each vertical level and time  $t$ ,  $\bar{N}_{\text{total}}(t)$ . This number concentration is then normalized by the number concentration at time  $t = 0$ ,  $\bar{N}_{\text{total}}(t = 0)$ . A subset of number concentration timeseries are shown in Figure 5.2 for the lowest 20

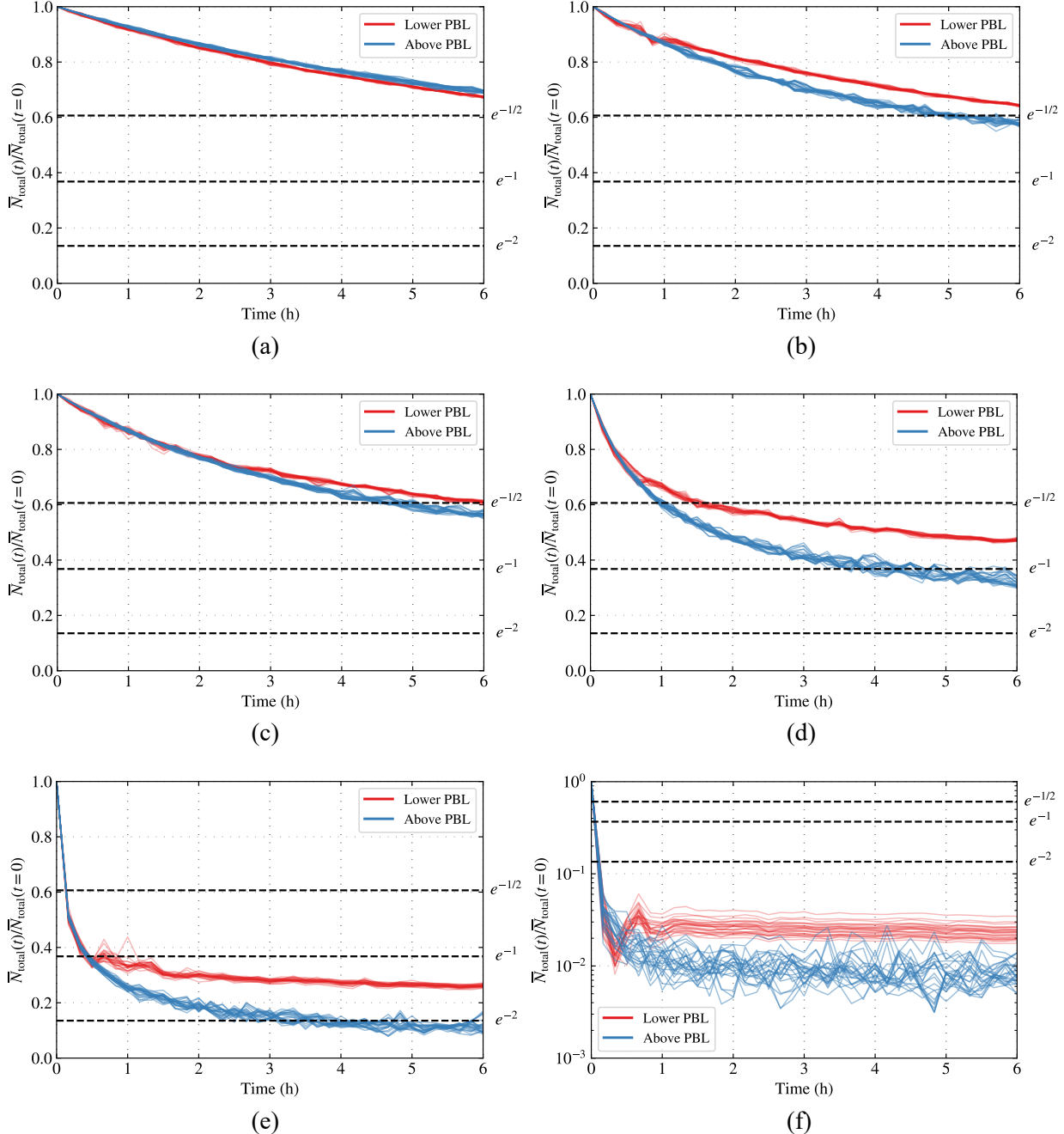


Figure 5.2: Total number concentration for each *SH* scenario normalized by the initial condition total number concentration. Lines indicate normalized number concentration averaged over each vertical level in the domain. (a) Uniform base case. (b–f) Scenarios 1–5

vertical levels of the PBL ( $z = 0$  m to  $z \sim 200$  m) and highest 20 vertical levels in the domain above the PBL ( $z \sim 1.8$  km to  $z = 2$  km). The reason for this grouping is that these two regions are notably different in terms of the rate at which the total number concentration decreases. For scenarios 1–5 (Figure 5.2 subfigures

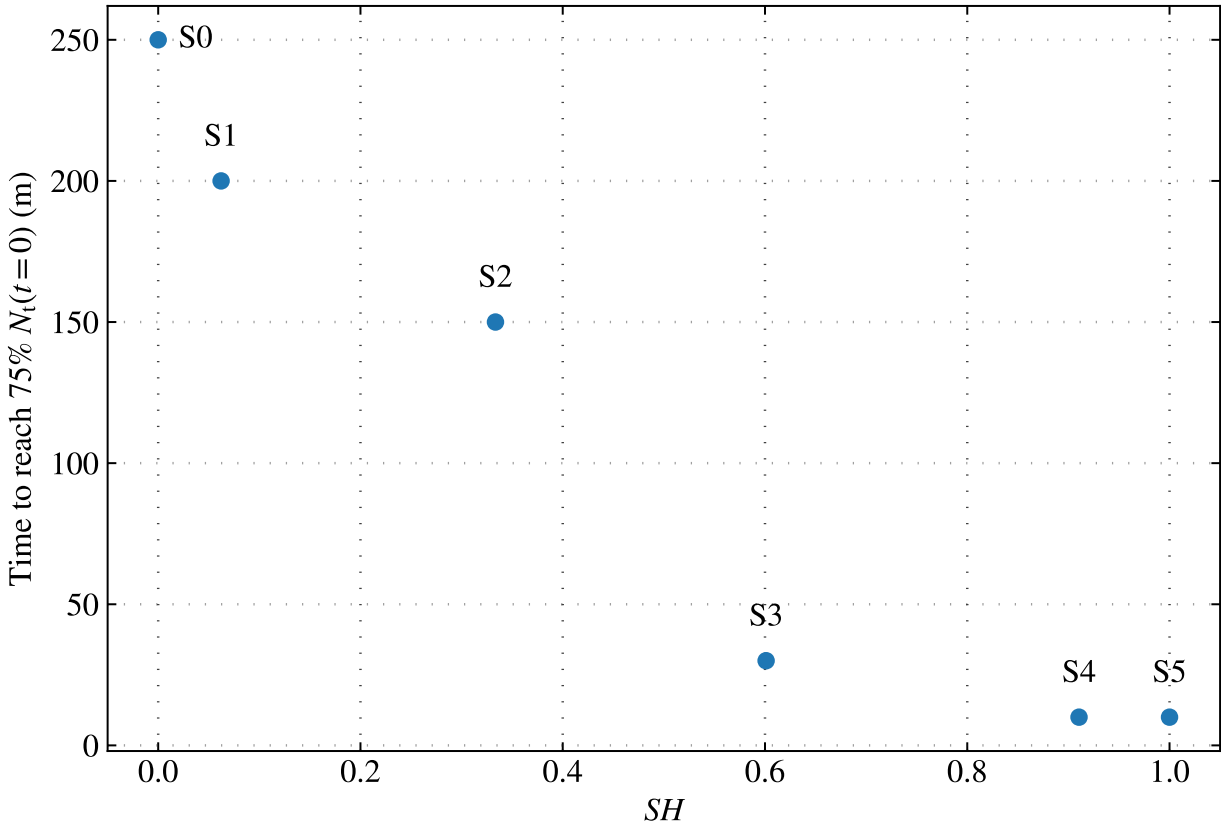


Figure 5.3: Time required in minutes for the total number concentration in the lowest 200 m of the PBL to be reduced to 75% of the initial value vs. scenario  $SH$ . “S0” is the uniform base case, with all other scenarios labeled S1–S5.

b–f), we find that the total number concentration decreases slower in the lower PBL than above the PBL. A notable exception to this trend is the uniform base case (Figure 5.2 subfigure a). Recall that the rate of coagulation scales as the square of the number of particles. As a result, highly heterogeneous patterns that require significant scaling up of the number concentration will have greater rates of coagulation within the high-concentration region associated with the  $SH$  pattern. As the PBL develops and turbulent motion begins to diffuse the initial structure of the  $SH$  pattern, concentration gradients are reduced, resulting in a reduction of the rate of coagulation. This turbulent motion does not disturb the structure of the  $SH$  pattern above the PBL, and thus coagulation will proceed at a faster rate within the high concentration region of the  $SH$  pattern.

We find that as the  $SH$  increases across scenarios, the total number concentration is reduced more rapidly. For each plot in Figure 5.2, we include horizontal dashed lines indicating the e-folding time alongside a half e-folding time ( $e^{-1/2}$ ) and double e-folding time as the rate at which the total number concentration is reduced under  $SH$  scenarios varies widely.

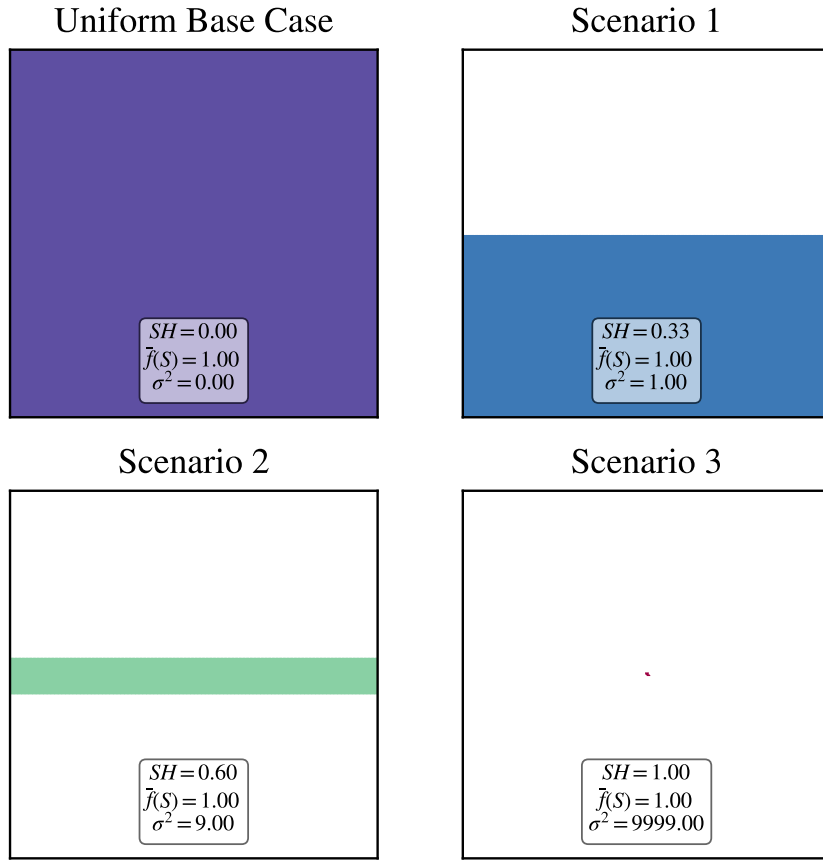


Figure 5.4: Emissions scenarios for multiphase chemistry simulations. The spatial heterogeneity of each emission scenario is listed in the lower portion of each scenario alongside domain mean and variance.

Figure 5.3 shows the time required the number concentration in the lower PBL to be reduced to 75% of the initial total number concentration plotted against the spatial heterogeneity of each scenario. The uniform base case (“S0”) requires over four hours to reach 75% of the initial total concentration, while the highest heterogeneity scenarios 4 and 5 require only 10 minutes.

## 5.2 Full multiphase simulations

Here we discuss simulations containing full multiphase chemistry under numerous emissions spatial heterogeneity scenarios. A summary of emissions scenarios is presented followed by presentation of results pertaining to the aerosol state and properties under each emission scenario.

### 5.2.1 Simulated emissions scenarios

Scenarios discussed in this section match the set of emissions scenarios presented in Chapter 4 Section 4.1. We evaluate changes to the aerosol population under four scenarios with increasing spatial heterogeneity as shown in Figure 5.4. As with previous results, the first scenario is a “uniform base case”, characterized by diffuse and uniform emissions across the ground level of the domain ( $SH = 0$ ). Scenarios 1–3 present progressively higher heterogeneity up to  $SH = 1$ , whereby the rate of emissions is scaled to ensure the total mass per unit time emitted across each scenario is the same.

### 5.2.2 Aerosol size distributions

Figure 5.5 shows aerosol number distributions for each simulated emissions scenario. The initial condition size distribution is presented alongside the size distribution at the end of each simulation ( $t = 6$  h). Each size distribution is taken from a vertical level in the upper boundary layer at  $z \sim 800$  m. Due to the stochastic treatment aerosols in the WRF-PartMC model and the chosen number of computational particles per grid cell ( $n = 100$ ), size distributions represent the average distribution in a  $1 \text{ km}^2$  region centered over the emissions plume. For all scenarios except scenario 1, this region is located at the center of the domain. For scenario 1, emissions are released in one half of the domain that is offset from the center, thus the averaging region for the size distribution is located in the center of the emissions plume. WRF-PartMC returns the number distribution in 100 logarithmically spaced bins ranging from  $10^{-9}$  m to  $10^{-3}$  m.

For each scenario displayed in Figure 5.5, the initial condition size distribution is shown in light blue. The distribution is bimodal, containing an Aitken (left) and accumulation mode (right). The Aitken mode contains fine particulates and is centered around 20 nm, while the accumulation mode contains slightly fewer particles and is centered around 116 nm.

After 6 hours, the number of particles with diameter smaller than  $\sim 30$  nm is significantly reduced as these small particles undergo coagulation and growth by gas-to-particle partitioning. For particle diameters greater than  $\sim 30$  nm, the number concentration is increased under each scenario as primary aerosol are emitted and particles undergo aging. For the uniform base case (Figure 5.5 subplot a), the distribution still takes on a bimodal shape at  $t = 6$  h, however the Aitken mode has been replaced by a mode centered around 35 nm and is likely a combination of primary aerosol emissions and growth of smaller particles from the initial Aitken mode.

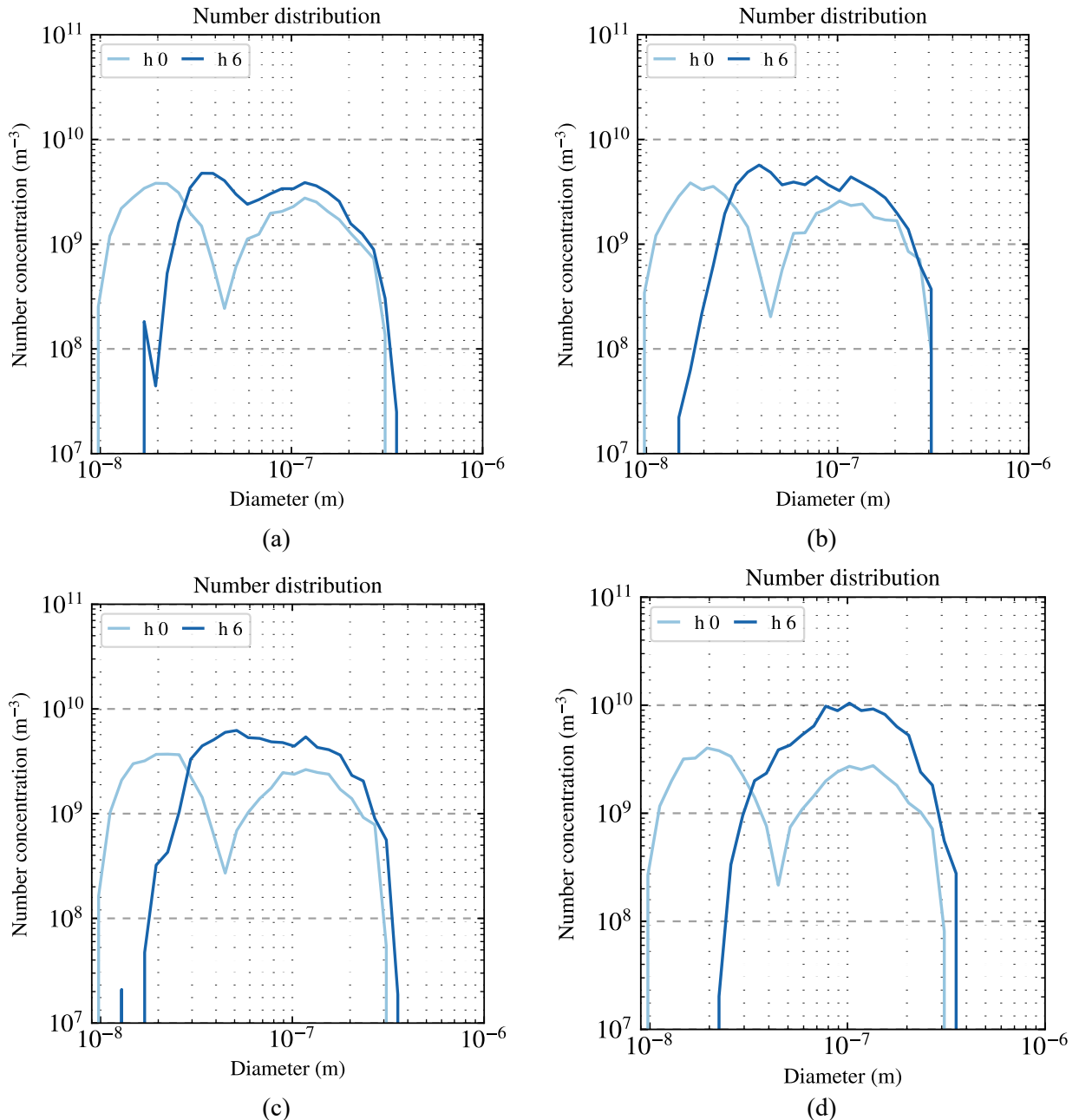


Figure 5.5: Aerosol number distribution plots for each emissions scenario. The distribution initial condition (light blue) is shown alongside the distribution at the end of each simulation ( $t = 6 \text{ h}$ ). Scenarios are labeled as the following: (a) uniform base case, (b) scenario 1, (c) scenario 2, (d) scenario 3.

Moving to higher emissions spatial heterogeneity scenarios, we find that the number distribution loses its bimodal shape after 6 hours, especially under the highest heterogeneity scenario, scenario 3 (Figure 5.5 subplot d). For scenario 3, the number distribution peaks around  $0.1 \mu\text{m}$ . Compared with the uniform base case, the number concentration of particles in the accumulation mode near  $D_p = 0.1 \mu\text{m}$  is approximately

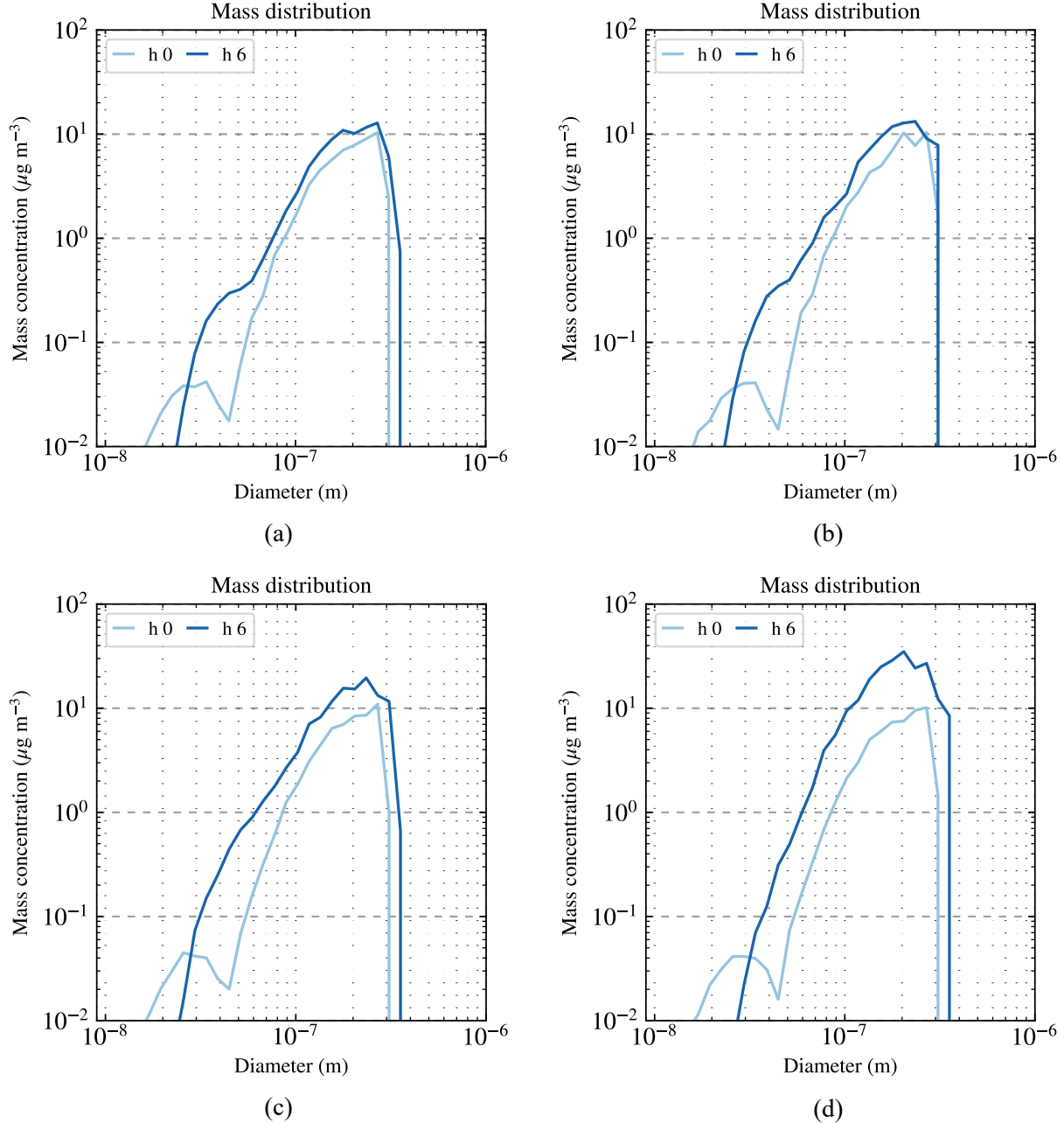


Figure 5.6: Aerosol mass distribution plots for each emissions scenario. The distribution initial condition (light blue) is shown alongside the distribution at the end of each simulation ( $t = 6$  h). Scenarios are labeled as the following: (a) uniform base case, (b) scenario 1, (c) scenario 2, (d) scenario 3.

half an order of magnitude higher ( $10^{10} \text{ m}^{-3}$  vs.  $4 \cdot 10^9 \text{ m}^{-3}$ ).

Figure 5.6 shows mass distribution plots for each emissions scenario. Mass distributions were taken from the same upper boundary layer region as number distributions and the same averaging technique was applied over a  $1 \text{ km}^2$  region centered over the emissions plume. Mass concentrations are presented in  $\mu \text{g m}^{-3}$ .

The mass distribution initial condition presents a bimodal profile as before; however, much more mass is concentrated in the larger accumulation mode particles due to the cubic scaling between mass and particle diameter,  $M_p \propto D_p^3$ . After six hours, the mass concentration of all particles with diameters larger than  $\sim 25$  nm is increased. The distribution for the uniform base case (Figure 5.6 subfigure a) contains two distinct modes, one corresponding to the accumulation mode and an additional mode centered around  $40 - 50$  nm. This mode likely contains primary aerosol emissions and particles that have grown from the Aitken mode due to aging processes.

As with the number distributions, when moving from low to high  $SH$  scenarios, the bimodal shape of the mass distribution is replaced by a single mode centered around the accumulation mode, peaking at  $D_p = 0.2$   $\mu\text{m}$ . When compared to the uniform base case, mass concentrations in the accumulation mode for the highest  $SH$  case, scenario 3, are approximately 3 times higher ( $\sim 30 \mu\text{g m}^{-3}$  vs.  $\sim 10 \mu\text{g m}^{-3}$ ).

### 5.2.3 Aerosol composition

Figure 5.7 shows time-height plots for aerosol sulfate concentrations in parts per billion by volume (ppbv). Mixing ratios are shown instead of mass concentrations as mixing ratio is independent of the atmospheric pressure and density. To compute the mixing ratio in ppbv for aerosol concentrations natively output by WRF-PartMC in  $\text{kg m}^{-3}$ , concentrations are multiplied by the inverse of atmospheric density for each vertical level and by a factor of  $10^9$  to convert from mol/mol to parts per billion.

As with previous time-height plots presented in Chapter 4, each pixel in the time-height grid mesh represents the average concentration over a given vertical level and time. Isopleths indicate lines of constant sulfate mixing ratios, ranging from 3.50 to 4.75 ppbv in increments of 0.25 ppbv.

Initially, each scenario contains a uniform sulfate concentration of  $\sim 3.5$  ppbv. During the first hour, concentrations gradually increase everywhere, likely due to the oxidation of ambient  $\text{SO}_2$  and partitioning of resulting  $\text{H}_2\text{SO}_4$  into the aerosol phase due to its extremely low volatility vapor pressure. As emissions turn on at  $t = 1$  h, the concentration of sulfate across emissions scenarios begins to diverge. In the uniform base case, sulfate concentrations steadily increase within the PBL through  $t = 6$  h up to 4.75 ppbv. For high  $SH$  scenarios such as scenario 3, the rate of increase in sulfate concentrations is suppressed—it takes nearly two hours for sulfate concentrations to increase from 4.25 ppbv at  $t = 4$  h to 4.50 by  $t = 6$  h whereas the same increase under the uniform base case takes approximately 1 hour between  $t = 3$  h and  $t = 4$  h. This results in lower sulfate concentrations within the PBL under high  $SH$  scenarios through  $t = 6$  h. For each scenario and

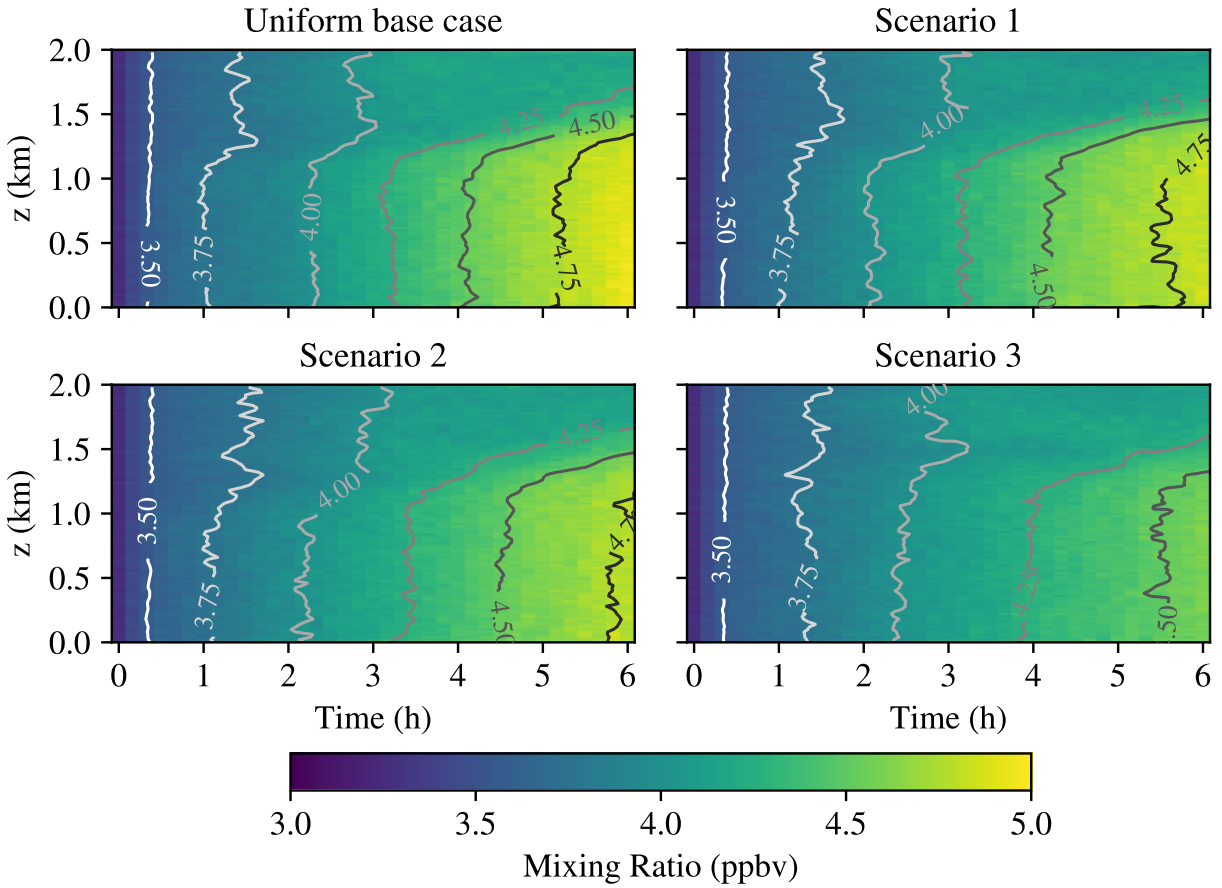


Figure 5.7: Time-height plots for aerosol sulfate across each emissions scenario. Isopleths indicate sulfate mixing ratio in ppbv ranging from 3.5–4.75 ppbv.

timestep, we find that sulfate concentrations are approximately uniform throughout the PBL.

Time-height plots for ammonium concentrations in each emissions scenario are shown in Figure 5.8. Initially, aerosol ammonium concentrations are uniformly 1.2 ppbv everywhere. Ammonium concentrations steadily increase as ambient ammonia partitions into the aerosol phase. Following the release of emissions at  $t = 1$  h, ammonium concentrations are similar across each scenario between  $t = 1$  h to  $t = 2$  h with concentrations increasing to 1.5 ppbv. Subsequently, ammonium concentrations differ both spatially and temporally across emissions scenarios. Ammonium concentrations in the base case remain diffuse and relatively uniform throughout the PBL, increasing to 1.8 ppbv through  $t = 6$  h. As  $SH$  increases across scenarios, ammonium concentrations in the upper PBL increase to as much as 2.1 ppbv in scenario 3 by  $t = 5$  to  $t = 6$  h. Meanwhile, concentrations in the lower PBL remain near 1.7–1.8 ppbv.

Figure 5.9 shows time-height plots of aerosol nitrate concentrations for each emissions scenario. Note

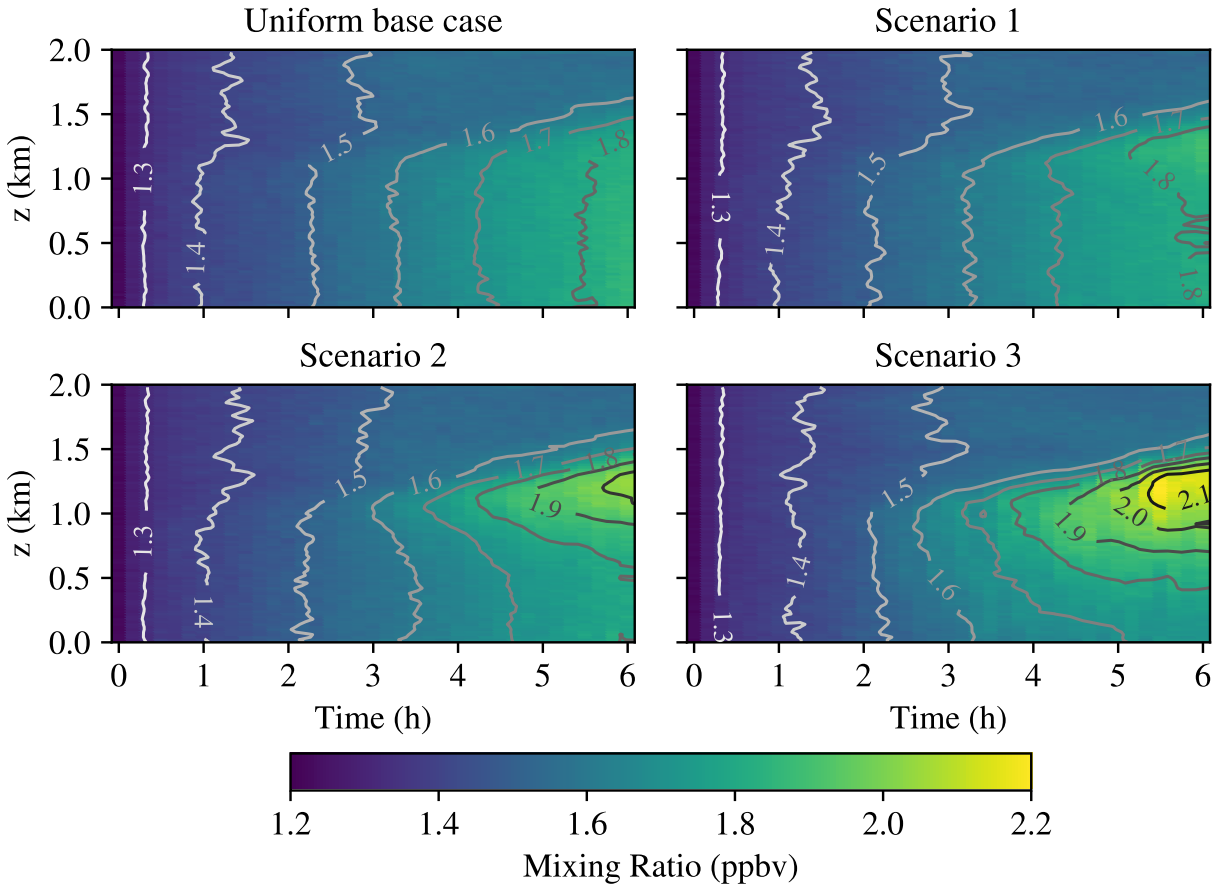


Figure 5.8: Time-height plots for aerosol ammonium across each emissions scenario. Isopleths indicate ammonium mixing ratio in ppbv ranging from 1.3–2.1 ppbv.

the logarithmic scaling for the color bar as nitrate concentrations span numerous orders of magnitude due to trace concentrations in some regions. Initially, no nitrate is present in the aerosol phase (zero concentrations are indicated by white). Nitrate concentrations remain at or below  $10^{-3}$  ppbv in the free troposphere throughout each scenario. When compared to sulfate and ammonium, the abundance of nitrate is most sensitive to emissions spatial heterogeneity as only trace amounts of nitrate ( $10^{-3}$ – $10^{-2}$  ppbv) are present in the upper PBL in the uniform base case, whereas concentrations reach 1 ppbv in the upper PBL in scenario 3. Additionally, the formation of nitrate occurs over a broader depth of the PBL for high *SH* scenarios and the onset of formation occurs earlier.

Time-height plots for sulfate, ammonium, and nitrate capture the spatial and temporal variation of each aerosol species across each emissions scenario. However, to help quantitatively summarize and compare the relative abundances of each species, we focus here on the final state of the sulfate-nitrate-ammonium system

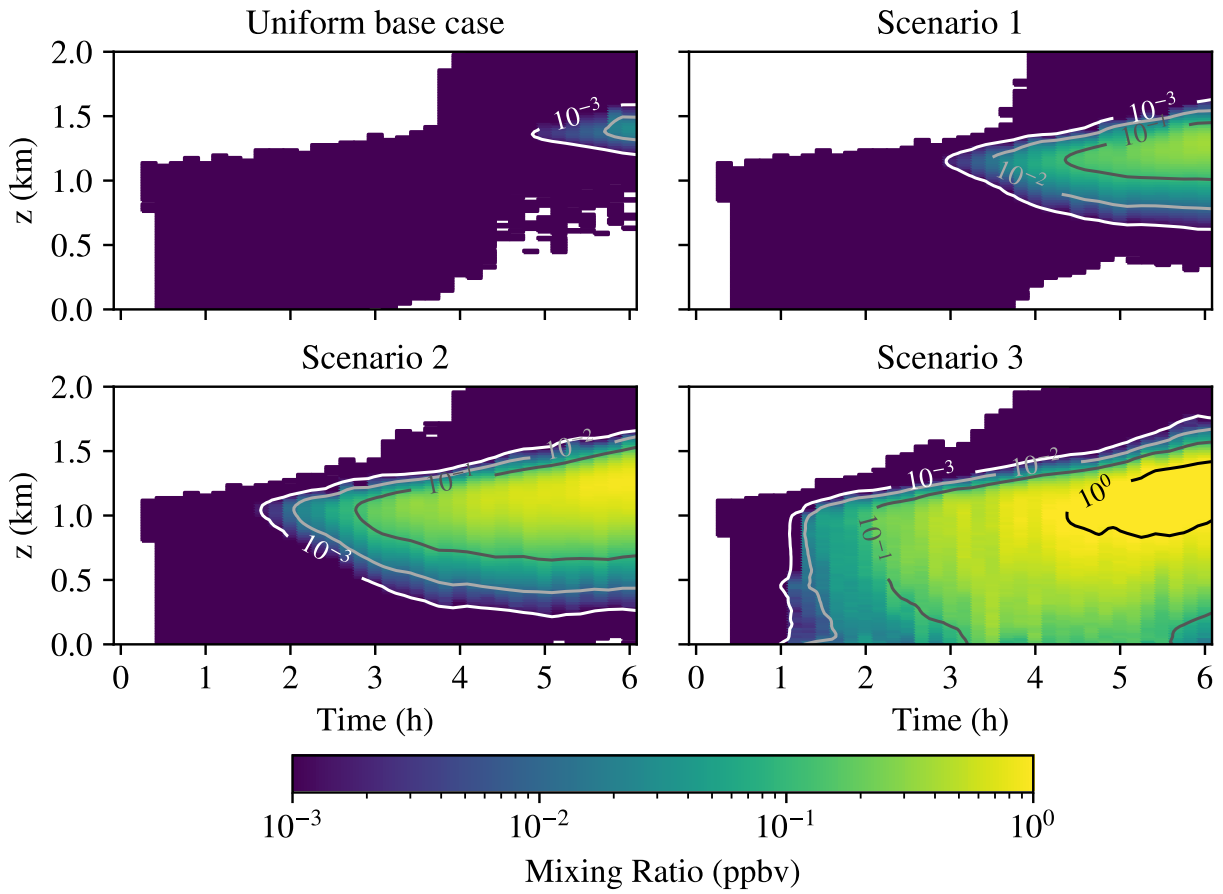


Figure 5.9: Time-height plots for aerosol nitrate across each emissions scenario. Isopleths indicate nitrate mixing ratio in ppbv ranging from  $10^{-3}$  to  $10^0$  ppbv.

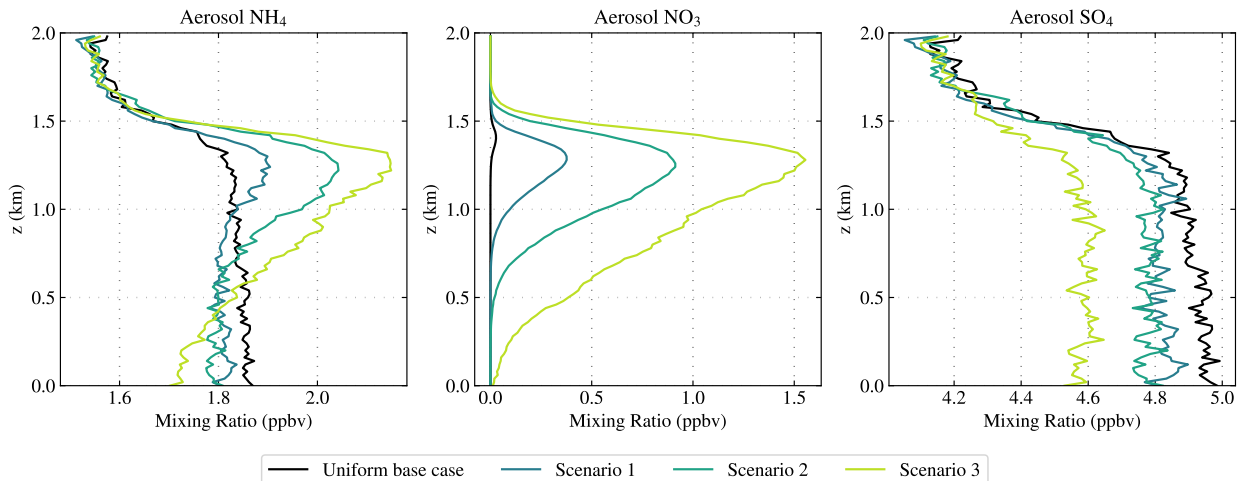


Figure 5.10: Vertical profiles of aerosol ammonia, nitrate, and sulfate at  $t = 6$  h.

at the end of each simulation,  $t = 6$  h. Figure 5.10 shows vertical profiles of ammonia, nitrate, and sulfate for  $t = 6$  h, whereby each vertical profile represents the horizontally averaged concentration in ppbv at each vertical level of the domain.

We find that ammonium has a relatively uniform concentration of 1.85 ppbv in the PBL for the uniform base case. As the spatial heterogeneity of emissions scenarios increases, the abundance of ammonium increases towards the upper PBL (which reaches a height of  $z \sim 1.5$  km by  $t = 6$  h), reaching 2.1 ppbv in the highest  $SH$  scenario. Near the surface, ammonia concentrations decrease as the  $SH$  of the emissions scenario increases.

Nitrate levels increase with increasing emissions  $SH$ . For lower  $SH$  scenarios, this increase is localized to the upper PBL. As emissions  $SH$  increases across scenarios, nitrate concentrations also increase in the lower PBL, however the region of highest nitrate concentrations remains vertically distributed in the upper PBL. Nitrate levels reach up to 1.5 ppbv at  $z \sim 1.25$  km in the highest  $SH$  scenario.

Compared with ammonium and nitrate, sulfate concentrations within the PBL are more vertically uniform for each emissions scenario. As the  $SH$  of emissions scenarios increases, sulfate concentrations are reduced by approximately the same amount everywhere in the PBL from a PBL average of 4.9 ppbv in the uniform base case to 4.6 ppbv in scenario 3.

Figure 5.11 shows the size-resolved mass fraction of aerosol particles in the upper PBL ( $z \sim 800$  m) at 2-hour intervals for the uniform base case. The average of species mass as a fraction of aerosol total mass is displayed for each aerosol species in WRF-PartMC. As with number and mass distribution plots, species concentrations are size-resolved with 100 logarithmically spaced bins between  $10^{-9}$  and  $10^{-3}$  m. Mass fractions are computed by dividing the mass of each species by the total mass of a bin. In order to reduce stochastic noise, an averaging strategy similar to that utilized for the number and mass distribution plots is employed, whereby mass fractions are computed for aerosol particles contained within a  $1 \text{ km}^2$  cross section of the domain centered over the emissions plume. Aerosol species model symbols are included in the key of Figure 5.11. A comprehensive list of aerosol species in WRF-PartMC is contained in Table 5.1 alongside a description of each species model symbol”.

For the initial condition, the composition of all particles is identical, with a mixture comprised of sulfate, organic carbon (OC), and ammonium. Once emissions are active at  $t = 1$  h, the release of carbonaceous primary aerosol introduces black carbon (BC) into the aerosol population. By  $t = 6$  h, BC makes up a meaningful fraction of aerosol mass for fine particulates; particles with diameter  $\sim 20$  nm are up to 50% BC

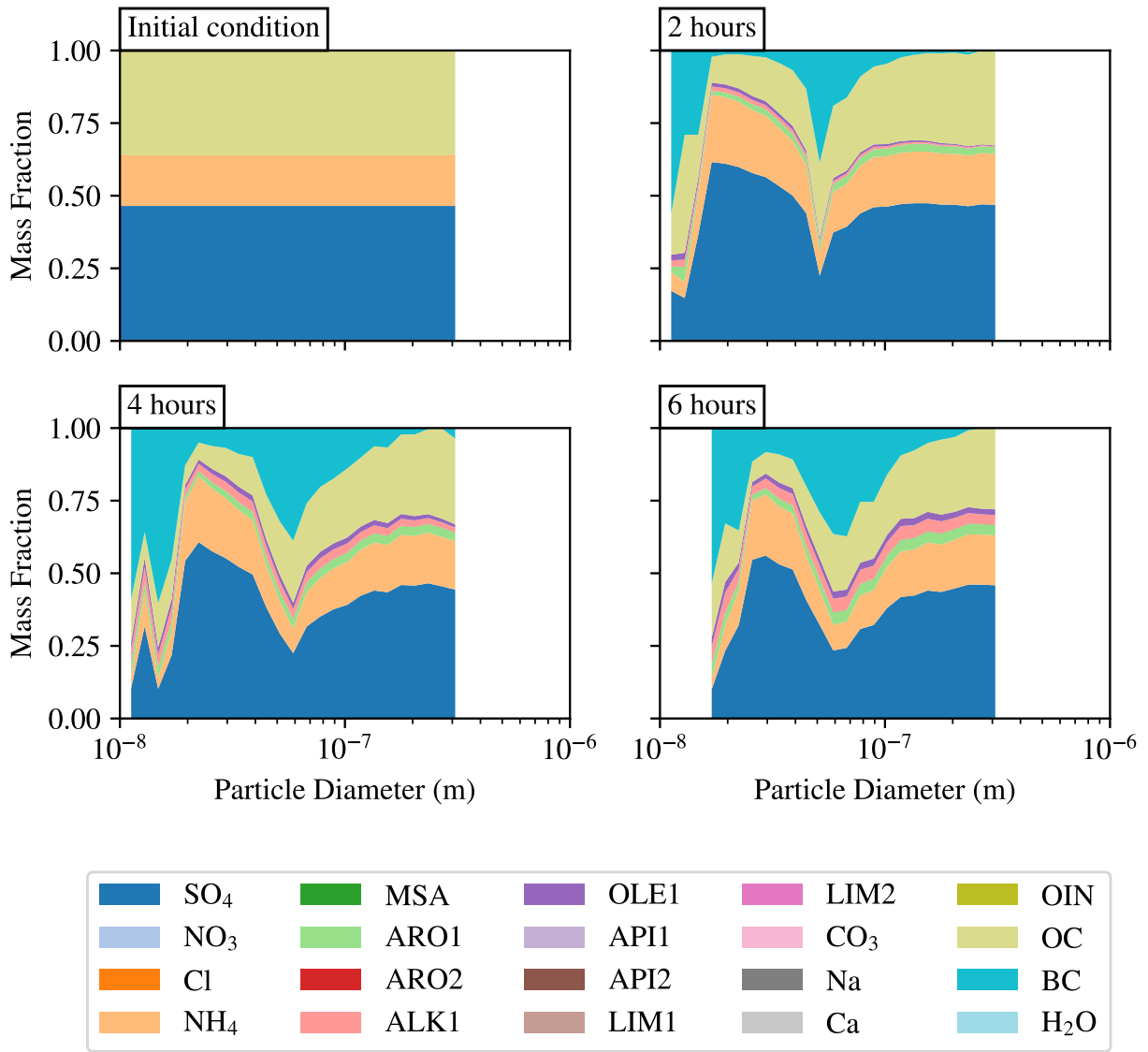


Figure 5.11: Size-resolved mass fraction for the uniform base case at regular 2-hour intervals.

and particles near 50–60 nm are  $\sim 40\%$  BC.

Additionally, volatile organic compounds (VOCs) are emitted in the gas phase which are oxidized, lowering their volatility and allowing them to condense into the aerosol phase as secondary organic aerosol (SOA). SOA species are organized by functional group in WRF-PartMC and include aromatics (“ARO1”, “ARO2”), alkanes (“ALK1”, “ALK2”), limonenes (“LIM1”, “LIM2”), etc (see Table 5.1 for a full list). In size-resolved mass fraction plots, SOA appears as a ribbon of green, pink, and purple atop nitrate (orange), indicating that alkanes, olefins, and aromatics comprise the bulk of SOA species present in aerosol particles. In total, SOA makes up a small fraction of aerosol mass, reaching up to 10% of total mass by  $t = 6$  h.

Table 5.1: Aerosol species and associated hygroscopicities in WRF-PartMC

Aerosol species	Model symbol	Hygroscopicity $\kappa$
Sulfate	SO4	0.65
Nitrate	NO3	0.65
Chloride	Cl	0.53
Ammonium	NH4	0.65
Nethanesulfonic acid	MSA	0.53
Aromatic	ARO1	0.1
Aromatic	ARO2	0.1
Alkanes	ALK1	0.1
Olefin	OLE1	0.1
$\alpha$ -pinene	API1	0.1
$\alpha$ -pinene	API2	0.1
Limonene	LIM1	0.1
Limonene	LIM2	0.1
Carbonate	CO3	0.53
Sodium	Na	0.53
Calcium	Ca	0.53
Other inorganics	OIN	0.1
Organic carbon	OC	0.001
Black carbon	BC	0
Water	H2O	0

Throughout the uniform base case simulation, the mass fraction of sulfate makes up a large portion of aerosol mass. After initially being comprised of 45% sulfate across all aerosol diameters, by  $t = 6$  h, sulfate mass fraction varies between a minimum of 10% for ultrafine particles less than 20 nm and peaks at  $\sim 50\%$  for particles near 30 nm. Particles in the accumulation mode are comprised of 30–40% sulfate. Ammonium initially comprises  $\sim 10\%$  of aerosol mass fraction and its relative contribution to total aerosol mass is fairly consistent across time, especially for larger particles ( $D_p > 0.1 \mu\text{m}$ ). The mass fraction of ammonium reaches a minimum for particles ultrafine particles less than 30 nm in diameter. It is important to note that no nitrate is present at any point during the uniform base case simulation.

Figure 5.12 shows size-resolved mass fraction plots for the highest heterogeneity case, scenario 3. By  $t = 6$  h, the composition of aerosol particles is markedly different than in the uniform base case shown in Figure 5.11. Most notably, we find that nitrate comprises a large fraction of aerosol mass, especially for particle diameters near  $D_p \sim 0.1 \mu\text{m}$ . As particle diameter decreases below  $0.1 \mu\text{m}$ , the mass fraction of sulfate steadily increases from less than 10% to nearly 60% for particles with diameter  $D_p \lesssim 30$  nm. Sulfate

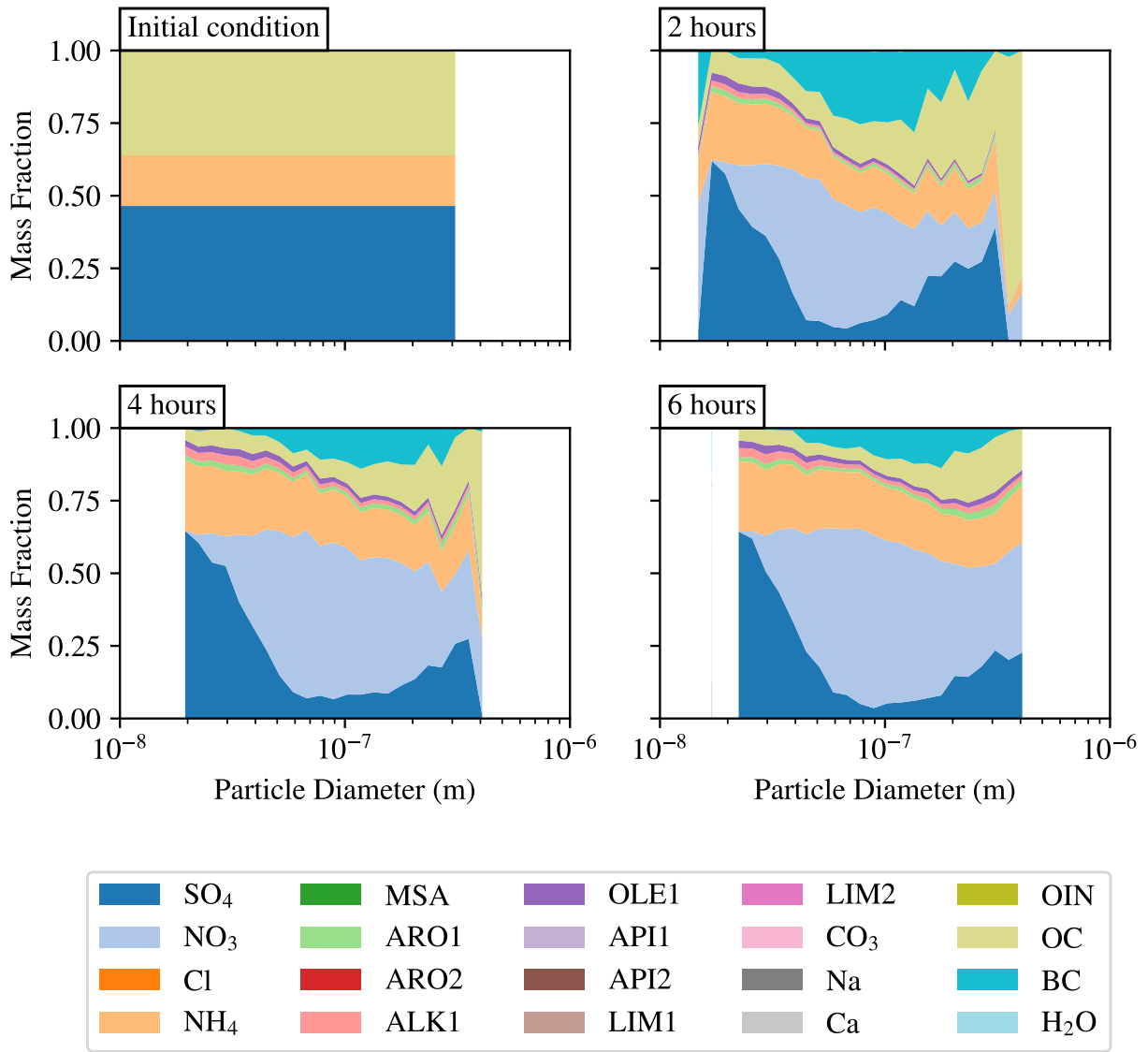


Figure 5.12: Size-resolved mass fraction for emissions scenario 3 at regular 2-hour intervals showing species mass fraction as a percent of total aerosol mass vs. particle diameter.

and nitrate effectively replace the large mass fraction of BC found for these ultrafine particles. By  $t = 6\text{ h}$ , sulfate, nitrate, and ammonium jointly comprise a majority of aerosol mass across all particles diameters observed in emissions scenario 3. For particles smaller than  $0.1\text{ }\mu\text{m}$ , sulfate, nitrate, and ammonium represent over 80% of aerosol mass. For particles larger than  $0.1\text{ }\mu\text{m}$ , these species comprise 70–80% of aerosol mass.

Differences observed in aerosol composition are important due to the varying properties of aerosol species and their downstream influence on the atmospheric state. For example, particle hygroscopicity determines the critical supersaturation at which a particle of a given diameter will active as a cloud condensation nucleus.

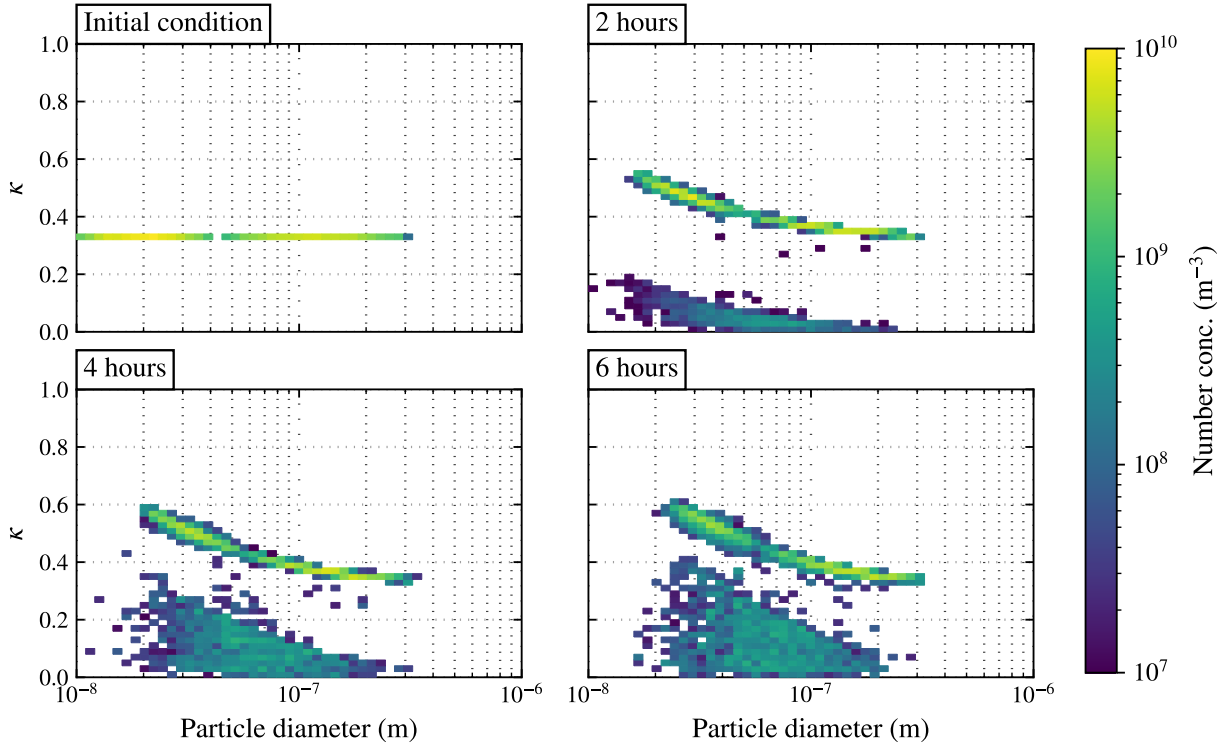


Figure 5.13: 2-dimensional number distributions  $n(D_p, \kappa)$  at regular two-hour intervals for the uniform base case.

Hygroscopicity is parameterized using the  $\kappa$ -Köhler theory of Petters and Kreidenweis 2007.  $\kappa$ -Köhler theory is a modification to Köhler's relationship for determining the saturation ratio over a particle and the critical supersaturation at which the particle activates (Köhler 1936). Each aerosol species has an associated hygroscopicity  $\kappa$ , and the total particle  $\kappa$  is a volume-weighted sum of each species  $\kappa$ . Note that Table 5.1 lists the hygroscopicity parameter  $\kappa$  of each aerosol species and is highly variable (e.g., the hygroscopicity of BC is zero while sulfate has a hygroscopicity of 0.65). Values of  $\kappa$  greater than 0.5 indicate the aerosol species has a high hygroscopicity, while  $\kappa = 0$  corresponds to a nonhygroscopic compound.

Figure 5.13 shows two-dimensional number distributions at regular two hour intervals for the uniform base case in the upper PBL ( $z \sim 800$  m). The x-axis indicates particle diameter in meters, while hygroscopicity  $\kappa$  is plotted along the y-axis. Particles are binned into a two-dimensional histogram by diameter (50 bins from 10 nm to 1  $\mu$ m) and  $\kappa$  (50 bins from 0 to 1) and the number concentration within each bin is tallied and displayed as a colorbar. Bins with zero particles are filled in white.

At the initial condition, we find that all particles posses the same total hygroscopicity,  $\kappa = 0.32$ , as each is a mixture of ammonium sulfate and OC. Beginning at  $t = 1$  h, emissions of primary aerosol and gas phase

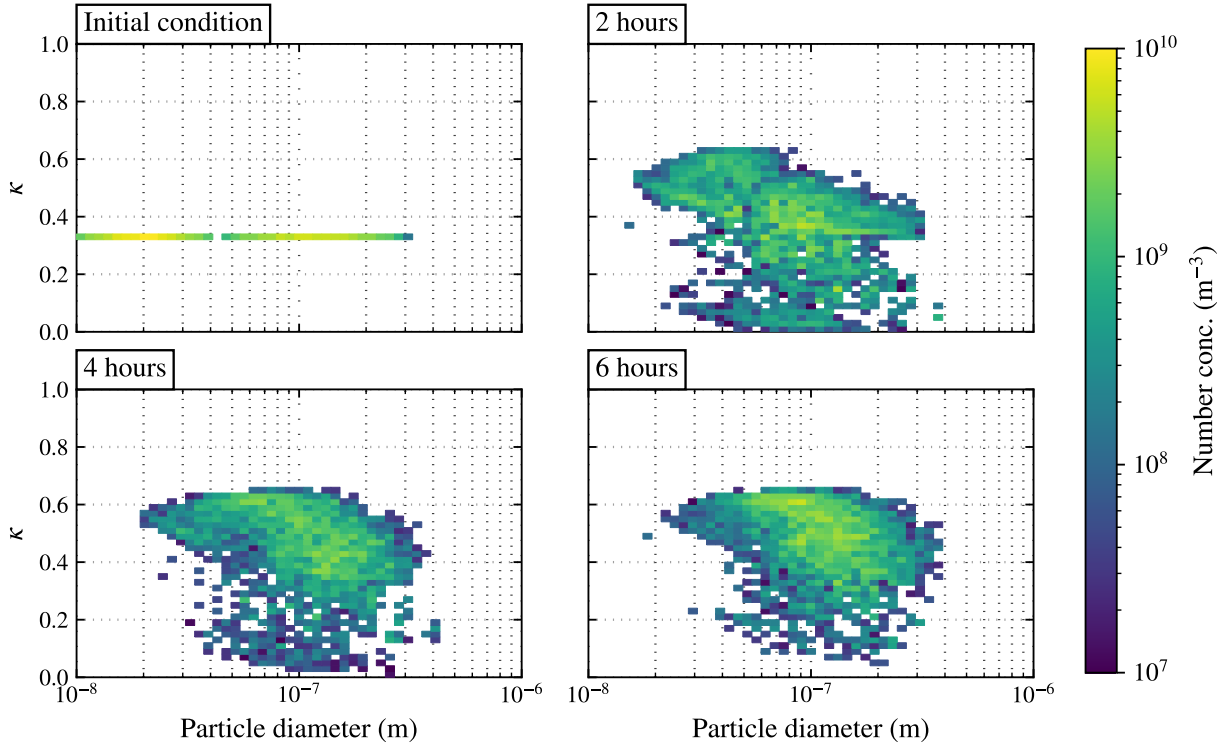


Figure 5.14: 2-dimensional number distributions  $n(D_p, \kappa)$  at regular two-hour intervals for scenario 3.

species alter the distribution of particle hygroscopicity. Recall that emitted primary aerosol are composed of OC and BC with  $\kappa$  values 0.001 and 0, respectively. This results in a distribution of low- $\kappa$  aerosol particles situated beneath the sulfate-rich aerosol. As the simulation evolves, gas-particle partitioning and coagulation age the aerosol population, increasing particle hygroscopicity.

Figure 5.14 shows two-dimensional size distributions at regular two hour intervals for the highest  $SH$  scenario, scenario 3. We find that following the initial condition, the evolution of the  $\kappa$ -resolved size distribution differs markedly from the uniform base case in numerous ways. First, the abundance of low- $\kappa$  primary aerosol due to emissions is greatly reduced for  $t = 2$  h to  $t = 6$  h. The increased rate of coagulation for high  $SH$  scenarios shown in Section 5.1.2 indicates that this process is likely enhanced for emissions scenario 3 and removes aerosol particles in the high-concentration emissions plume. Additionally, we find a greater abundance of high- $\kappa$  particles in the size range 20 nm to 0.4  $\mu\text{m}$  with  $\kappa$  in excess of 0.6 for some particles near  $D_p = 0.1 \mu\text{m}$ . By comparison, far fewer particles in the uniform base case posses  $\kappa \sim 0.6$  and are limited to the size range 20–30 nm.

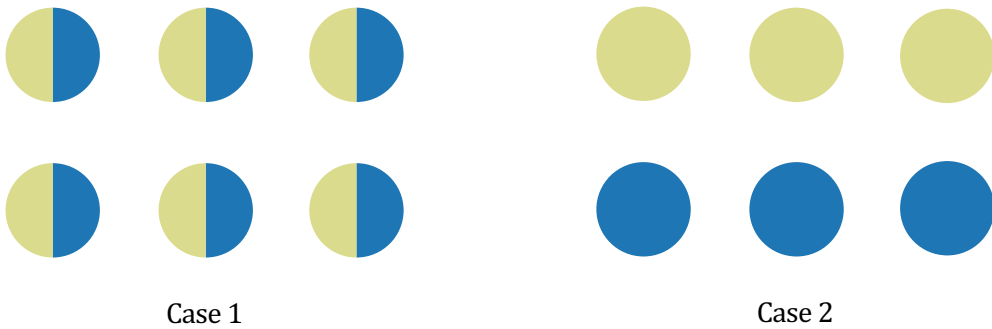


Figure 5.15: Two idealized cases for aerosol populations composed of ammonium sulfate (blue) and organic carbon (beige). Case 1 is fully internally mixed while case 2 is fully externally mixed, yet each case contains the same bulk concentration of each species.

#### 5.2.4 Aerosol mixing state

So far in this section we have shown results for the bulk composition of the aerosol. That is, we have shown which aerosol species are contained in the population, their mean abundances, and how they vary with particle size. However, these results do not indicate how each aerosol species is distributed amongst the particles in the population. Consider two cases, each with a grouping of six monodisperse aerosol particles. In the first case, all aerosol particles are an equal mixture of 50% ammonium sulfate and 50% OC. In the second case, half of the particles are 100% ammonium sulfate and the remaining half are 100% OC. When averaged to find the bulk composition of the population, each case leads to the same conclusion—the population is composed of 50% ammonium sulfate and 50% OC. However, this bulk state oversimplifies the compositional diversity of the particle population and aerosol particle properties vary considerably across each case. Note that the hygroscopicity  $\kappa$  under the two cases will differ. If all particles are internally mixed as in the first case (i.e., each particle is a mixture of ammonium sulfate and OC), all particles have a  $\kappa$  [actually compute that here]. For the second case, the particles are externally mixed (i.e., each particle is purely composed of a single aerosol species), resulting in the ammonium sulfate particles being highly hygroscopic,  $\kappa = \text{compute}$ , while the pure OC particles are nearly nonhygroscopic,  $\kappa = 0.001$ . As a consequence, there will exist a supersaturation at which all of the particles in case 1 active as CCN, while only half of the particles in the second case will active. This illustrates the importance of the aerosol mixing state, which describes how externally or internally mixed aerosol species are in the particle population.

The mixing state  $\chi$  is quantified using the metric definition of N. Riemer and M. West 2013 and is defined

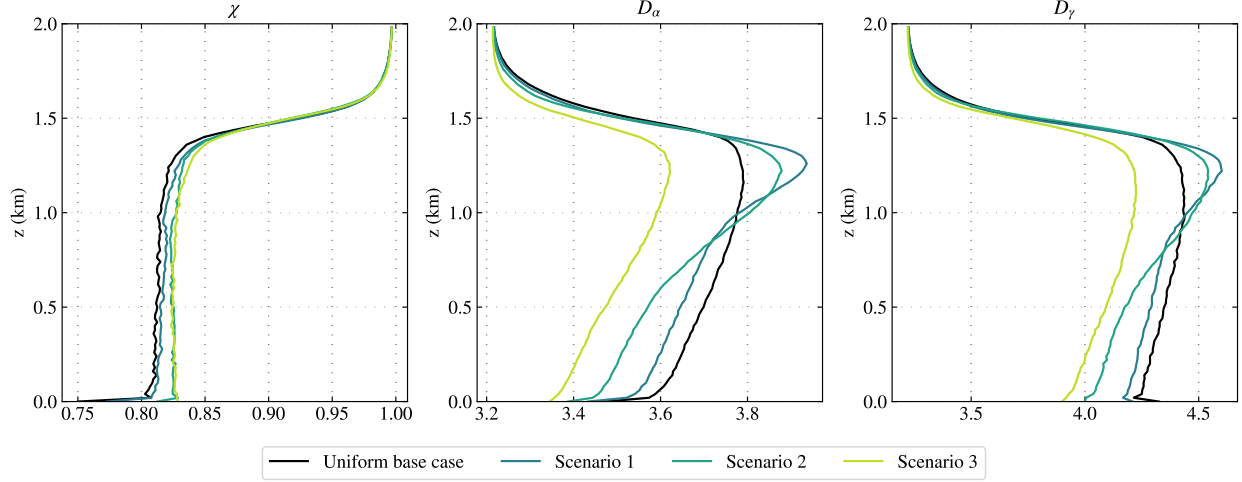


Figure 5.16: Vertical profiles for mixing state  $\chi$  and diversity measures  $D_\alpha$  and  $D_\gamma$  for each emissions scenario at  $t = 6$  h.

as

$$\chi = \frac{D_\alpha - 1}{D_\gamma - 1}, \quad (5.1)$$

where  $D_\alpha$  is the average particle species diversity and  $D_\gamma$  is the bulk population species diversity.  $D_\alpha$  is related to the average Shannon entropy for each particle as

$$D_\alpha = \exp \left( \sum_{i=1}^N p_i H_i \right), \quad (5.2)$$

where  $p_i$  is the mass fraction of particle  $i$  in the population and  $H_i$ , the Shannon entropy of the species distribution in particle  $i$ , is

$$H_i = \sum_{a=1}^A -p_i^a \ln(p_i^a), \quad (5.3)$$

where  $p_i^a$  is the mass fraction of species  $a$  in particle  $i$ .

$D_\gamma$  is related to the Shannon entropy for the distribution of an aerosol species in the population as

$$D_\gamma = \exp \left( \sum_{a=1}^A p^a \ln(p^a) \right), \quad (5.4)$$

where  $p^a$  is the mass fraction of species  $a$  in the population.

Figure 5.16 shows vertical profiles for  $\chi$  and its associated diversity measures  $D_\alpha$  and  $D_\gamma$  for each emissions scenario at  $t = 6$  h. We find that  $\chi$  is approximately the same across each emission scenario in

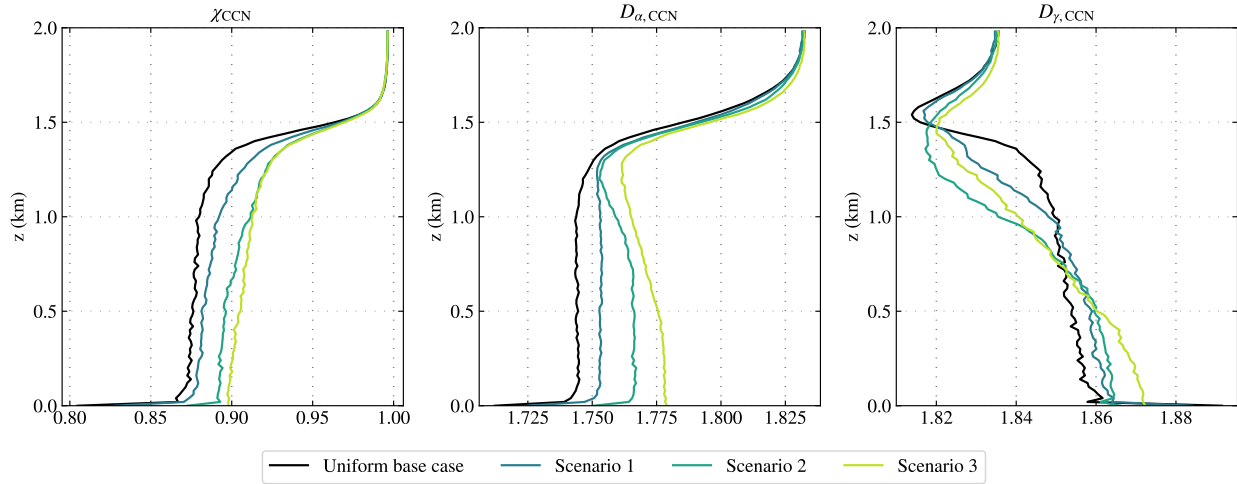


Figure 5.17

both the PBL and in the free troposphere. Furthermore,  $\chi$  is nearly uniform within the PBL, with values near  $\chi \sim 0.81$  in the uniform base case and  $\chi \sim 0.83$  in the highest  $SH$  scenario, scenario 3. Above the PBL,  $\chi$  matches closely across all scenarios and reaches  $\chi \sim 1$  by the top of the domain. These results point to a near-fully internally mixed aerosol population in the PBL and completely internally mixed aerosol above the PBL.

We find that diversity measures  $D_\alpha$  and  $D_\gamma$  increase with height in the PBL and subsequently decrease in the free troposphere. In the middle to lower PBL, both  $D_\alpha$  and  $D_\gamma$  decrease for high  $SH$  scenarios relative to the uniform base case. We find that  $D_\alpha$  and  $D_\gamma$  both peak near the top of the PBL and reach a maximum for emissions scenario 1 at 3.95 and 4.6, respectively.

Figure 5.17 shows vertical profiles for  $\chi$  and diversity measures  $D_\alpha$  and  $D_\gamma$  for particles which activate as CCN [Need to ask Jeff how mixing state is calculated for CCN? Is this for particles that activate above a certain supersaturation threshold?]. For each emissions scenario,  $\chi_{CCN}$  gradually increases in the PBL.  $\chi_{CCN}$  is slightly greater than  $\chi$  for each scenario, indicating that CCN are very well mixed in the PBL. Furthermore,  $\chi_{CCN}$  increases slightly with greater emissions  $SH$  (e.g., at  $z = 500$  m,  $\chi_{CCN} = 0.87$  for the uniform base case and  $\chi_{CCN} = 0.90$  for scenario 3). As  $SH$  increases,  $D_{\alpha,CCN}$  also slightly increases in the PBL (e.g., at  $z = 500$  m,  $D_{\alpha,CCN} = 1.74$  for the uniform base case and  $D_{\alpha,CCN} = 1.77$  for scenario 3). Above the PBL,  $D_{\alpha,CCN}$  tends to converge across emissions scenarios, increasing to  $\sim 1.83$  at  $z = 2$  km. We find that  $D_{\gamma,CCN}$  gradually decreases moving vertically in the PBL for each emissions scenario. As  $SH$  increases across emissions scenarios,  $D_{\gamma,CCN}$  takes on higher values in the lower to middle boundary layer, while in the middle to upper

boundary layer this trend is reversed, with higher  $SH$  indicating lower values of  $D_{\gamma,CCN}$ .

### 5.2.5 Impacts of emissions $SH$ on CCN activity

We have shown that emissions spatial heterogeneity alters the aerosol composition, producing more nitrate-rich particles and that this results in an increase in aerosol hygroscopicity  $\kappa$ . The critical supersaturation at which a particle activates as a cloud condensation nucleus is a function of  $\kappa$  and particle diameter. Thus, changes to the aerosol properties such as composition and hygroscopicity will propagate to changes in CCN activity.

Here, we group particles by critical saturation into CCN that activate at the following supersaturation levels:  $S = 0.1, 0.3, 0.6, 1.0\%$ . CCN concentrations at each supersaturation level are determined in the following manner. First, the critical supersaturation  $S_c$  is determined for each particle by using a root finding algorithm to solve for the critical point of the supersaturation curve  $S(D_p, \kappa)$  of  $\kappa$ -Köhler theory Petters and Kreidenweis 2007. Particles are then grouped by supersaturation ( $0.1, 0.3, 0.6, 1.0\%$ ) required for activation in a cumulative manner (i.e., particles activating at  $S = 0.3\%$  are included in bins for  $S = 0.5\%$  and higher supersaturations as they will activate at any supersaturation higher than  $S = 0.3\%$ ). Subsequently, the concentration of CCN at each supersaturation level is determined for each grid cell.

Figure 5.19 shows vertical profiles for each emissions scenario of CCN that activate at supersaturations  $S = 0.1, 0.3, 0.6, 1.0\%$ . Each vertical profile is taken at time  $t = 6$  h and displays the level-averaged mixing ratio in ppbv of particles that would act as CCN at each supersaturation level (note, environmental conditions do not exceed 100% RH at any point or time in each simulation).

For  $S = 0.1\%$ , we find that CCN concentrations decrease with increasing  $SH$  in the lower boundary layer. In the middle to upper boundary layer, the opposite trend is observed, with CCN concentrations increasing as emissions  $SH$  increases. This increase is most pronounced at the top of the PBL ( $z \sim 1.25$  km), where CCN concentrations reach nearly 1.2 ppbv for scenario 3 compared to 1.0 ppbv in the uniform base case.

Increases in CCN concentrations due to increasing emissions  $SH$  are observed everywhere in the PBL for  $S = 0.3\%$ , with concentrations again peaking near the top of the boundary layer. For the highest  $SH$  scenario, we find CCN concentrations in the upper PBL exceed 3.5 ppbv, while in the uniform base case, CCN concentrations are a vertically uniform 2.8 ppbv.

For  $S = 0.6\%$ , we find that CCN concentrations in the lowest 500 m of the PBL for Scenarios 1–3 are slightly lower than in the uniform base case. In the middle to upper PBL, we find that the increases in  $SH$

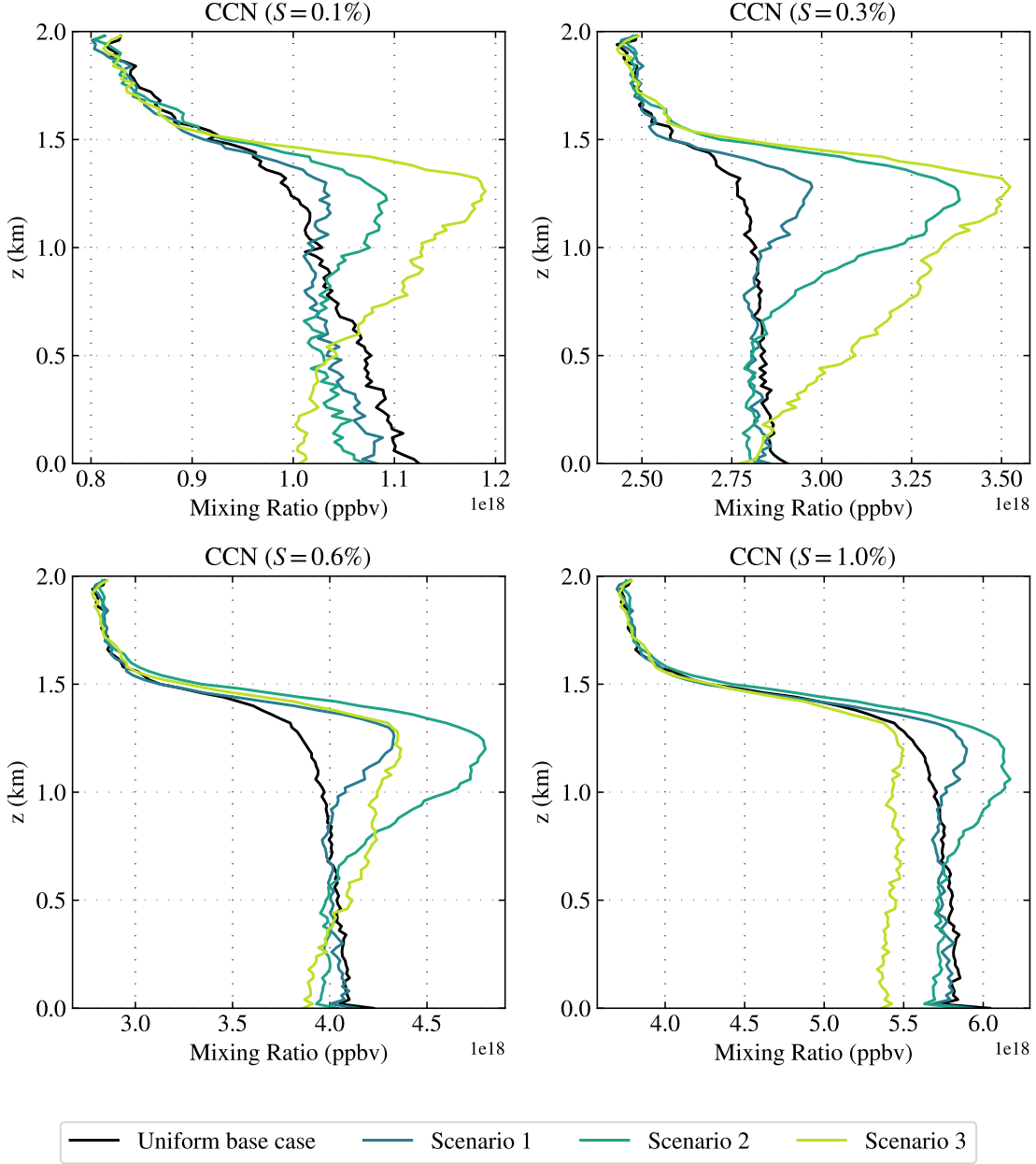


Figure 5.18: Vertical profiles ( $t = 6$  h) for each emission scenario of CCN activating at supersaturations  $S = 0.1, 0.3, 0.6, 1.0\%$

correspond to non-monotonic changes in CCN concentrations (i.e., CCN concentrations do not appear to increase with progressively higher  $SH$  scenarios as found in the upper PBL for  $S = 0.1\%$  and  $S = 0.3\%$ ). Instead, CCN concentrations in the upper PBL for  $S = 0.6\%$  are highest for the mid- $SH$  scenario (scenario 2), followed by scenario 3, scenario 1, and the uniform base case.

For  $S = 1.0\%$  we also find a complex set of responses to CCN concentrations across emissions  $SH$

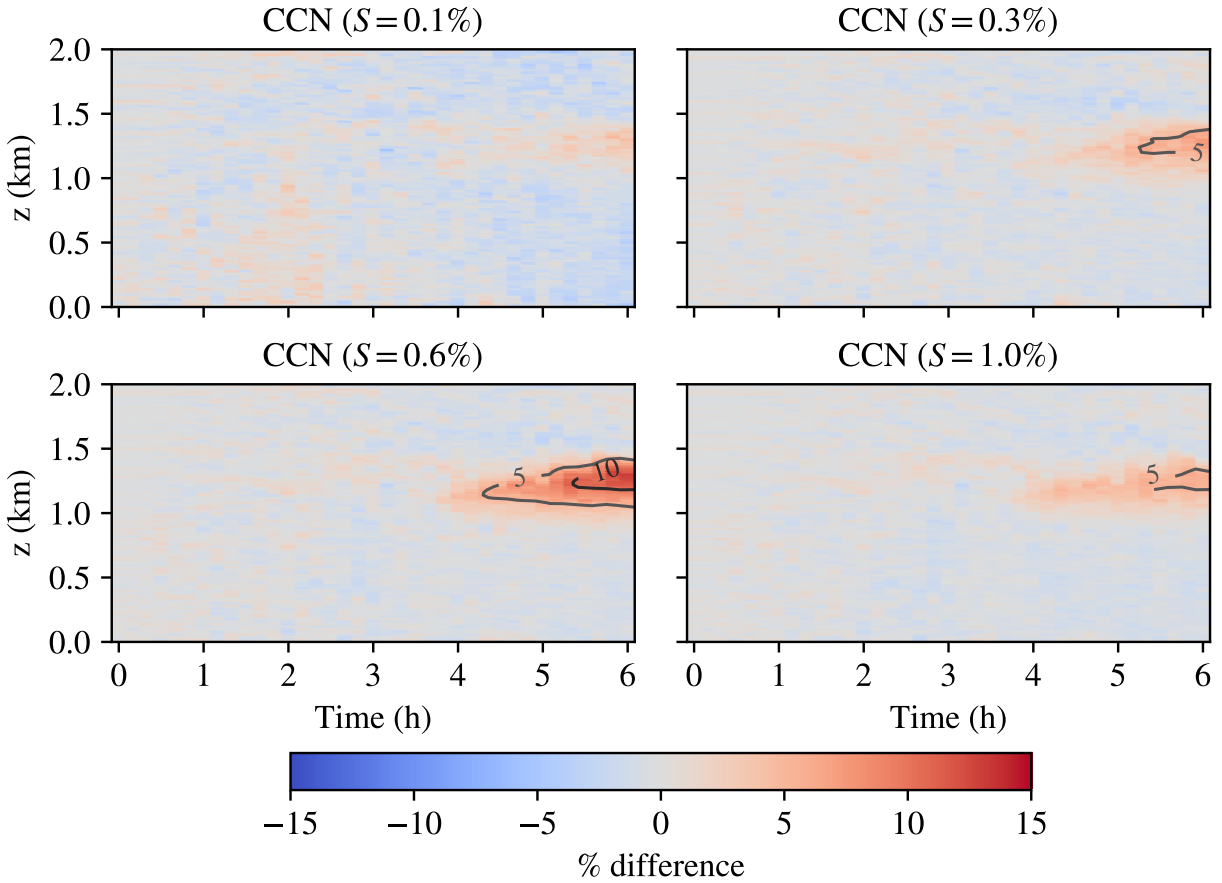


Figure 5.19: Time-height plots for the percent difference between CCN concentrations in the uniform base case and scenario 1 for each supersaturation level. Red indicates an increase in CCN relative to the base case while blue indicates a decrease. Isopleths indicate lines of constant percent difference in increments of 5%.

scenarios. For low to mid-*SH* scenarios 1 and 2, we find that CCN concentrations in the lowest 600 m of the PBL closely align with the uniform base case. In the middle to upper boundary layer, scenarios 1 and 2 exhibit an increase in CCN concentrations relative to the uniform base case. We find that CCN concentrations for  $S = 1.0\%$  in the highest *SH* scenario, scenario 3, are approximately uniform throughout the extent of the PBL at 4.4 ppbv, slightly less than the 4.6 ppbv observed for the uniform base case.

Figure 5.19 shows time-height plots for the percent difference of CCN concentrations in emissions scenario 1 relative to the uniform base case. Plots are shown for each supersaturation level ( $S = 0.1, 0.3, 0.6, 1.0\%$ ). Red indicates increases in CCN concentrations relative to the base case while blue indicates a decrease. To aid interpretability, isopleths indicating percent difference in steps of 5% are shown on each figure. If no isopleths are present, this indicates that percent difference did not exceed 5% anywhere or at any time between the

emissions scenario CCN concentrations and the uniform base case. Percent difference is calculated as

$$\% \text{ difference} = 100 \times \left( \frac{\overline{[\text{CCN}]}(t, z, S)_{\text{Scenario}} - \overline{[\text{CCN}]}(t, z, S)_{\text{Base case}}}{\overline{[\text{CCN}]}(t, z, S)_{\text{Base case}}} \right), \quad (5.5)$$

where  $\overline{[\text{CCN}]}(t, z, S)_{\text{Scenario}}$  is the horizontally averaged concentration of CCN at time  $t$  and vertical level  $z$  that activate at supersaturation  $S$  for the given emissions scenario and  $\overline{[\text{CCN}]}(t, z, S)_{\text{Base case}}$  is the horizontally averaged concentration of CCN at time  $t$  and vertical level  $z$  that activate at supersaturation  $S$  for the uniform base case.

Stepping through each supersaturation level, we find that at  $S = 0.1\%$ , percent difference does not exceed 5% at any point during the simulation. Slight spatial and temporal fluctuations are found in CCN concentrations, however, these do not appear to significantly depart from percent difference between scenario 1 and the uniform base case in the first hour of the simulation during which the configuration and spinup of each simulation is identical, indicating that internal variability due to stochastic noise is likely on the order of 1–2%.

For  $S = 0.3\%$ , we find a slight increase in CCN concentrations beginning at  $t = 5$  h from  $z \sim 1.1$  km to  $z \sim 1.4$  km on the order of 5%. Similarly for  $S = 0.6\%$  and  $S = 1.0\%$ , we find that CCN concentrations increase in the upper PBL. At  $S = 0.6\%$  CCN concentrations increase up to 10% by  $t = 5$  h. At  $S = 1.0\%$ , we find similar behavior in the percent difference for  $S = 0.3\%$ , with an increase in CCN concentrations the upper PBL of up to 5%.

Figure 5.20 shows time-height plots for percent difference in CCN concentrations at each supersaturation level between scenario 2 and the uniform base case. We find that for each supersaturation level, CCN concentrations increase in the upper PBL by at least 5%. Additionally, the onset of increased CCN concentrations relative to the uniform base case is earlier than found for scenario 1 for each supersaturation level.

For  $S = 0.1\%$ , we find that CCN concentrations in the upper PBL increase up to 5% beginning at  $t = 4.5$  h. For  $S = 0.3\%$  and  $S = 0.6\%$ , we find increases of up to 20% with elevated concentrations relative to the uniform base case beginning at  $t \sim 3$  h and gradually increasing in the upper PBL through the remainder of each simulation. For  $S = 1.0\%$ , CCN concentrations increase in a similar manner to those found for  $S = 0.1\%$  with concentrations increasing up to 5% in the upper PBL. However, CCN concentrations increase earlier than in the lower supersaturation case, with elevated concentrations by 5% in the upper PBL appearing around  $t = 2.5$  h.

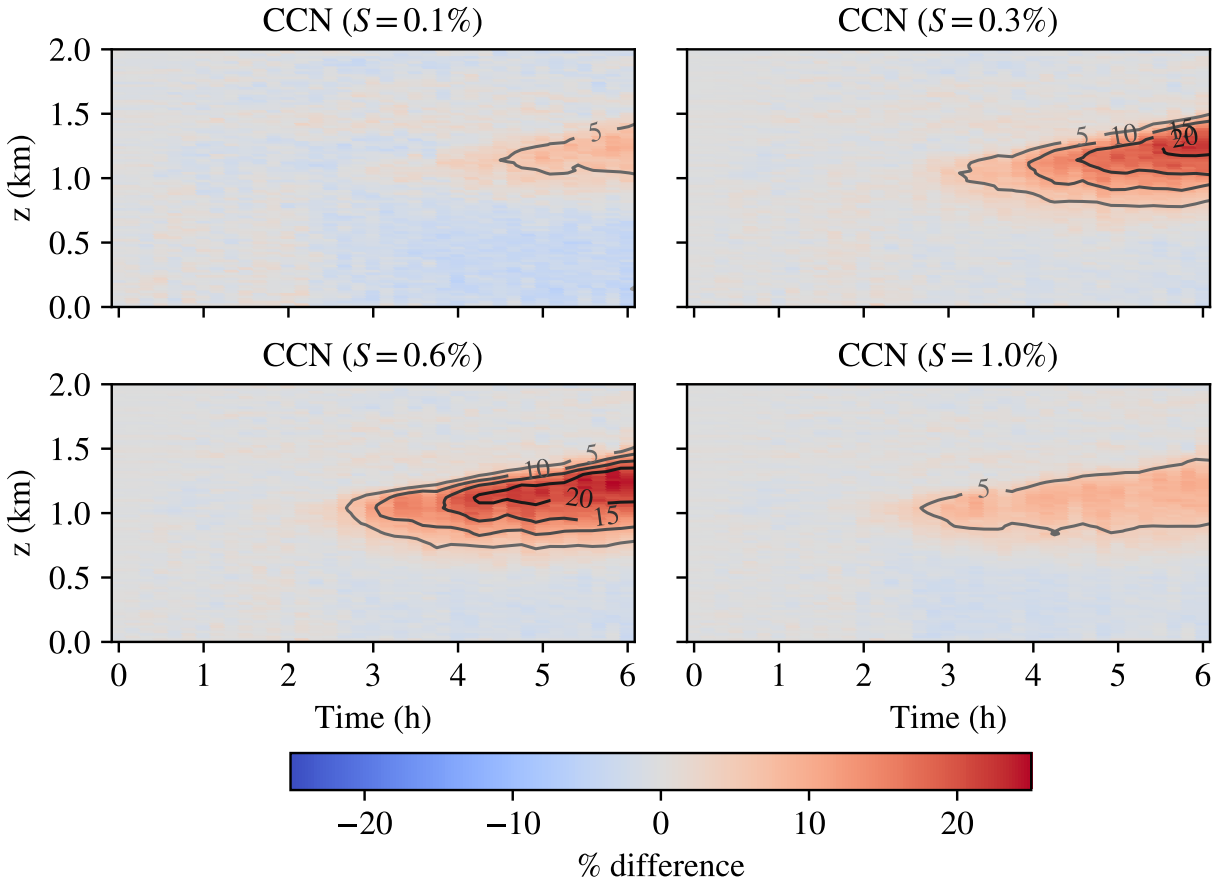


Figure 5.20: Time-height plots for the percent difference between CCN concentrations in the uniform base case and scenario 2 for each supersaturation level. Red indicates an increase in CCN relative to the base case while blue indicates a decrease. Isopleths indicate lines of constant percent difference in increments of 5%.

Figure 5.21 displays time-height plots for percent difference in CCN concentrations at each supersaturation level between scenario 3 and the uniform base case. Compared with scenarios 1 and 2, the trend of increasing CCN concentrations is much more vertically and temporally varied, particularly for  $S = 0.3\%$  and  $S = 0.6\%$  where an increase in CCN concentrations begins in the upper PBL at  $t = 2$  h, extends downward throughout the vertical extent of the PBL by  $t = 3$  h, and moves back upwards towards the mid to upper PBL beginning at  $t = 4$  h.

For  $S = 0.1\%$ , CCN concentrations increase by up to 20% in the upper boundary layer by  $t = 5.5$  h. Beginning around  $t = 5$  h, CCN concentrations decrease by up to 5% in the lowest 300 m of the domain. At  $S = 0.3\%$ , CCN concentrations increase by up to 25% in the upper PBL beginning at  $t = 5$  h. This is the highest magnitude CCN concentration percent difference observed for any supersaturation and across any emissions scenario. For  $S = 0.6\%$ , CCN concentrations increase by 10–15%, indicating a notable drop in

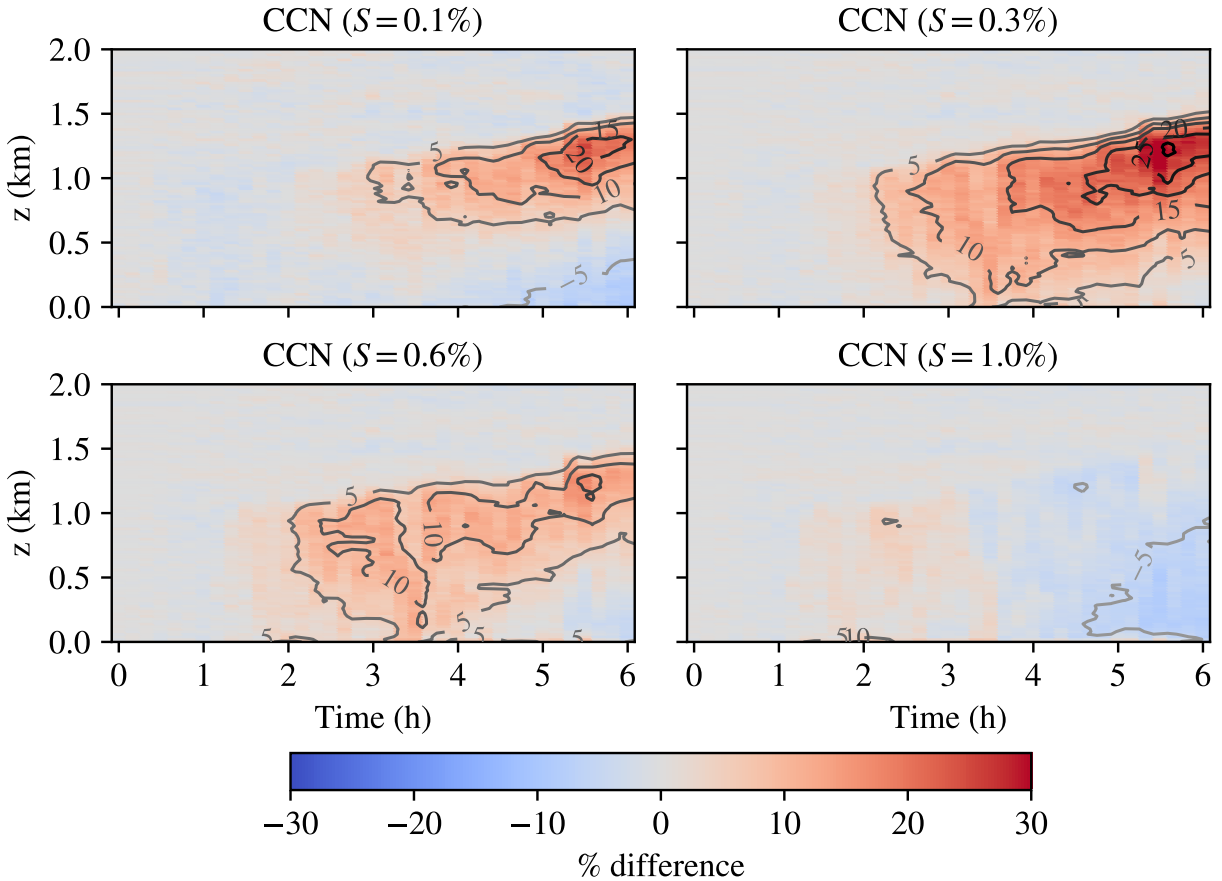


Figure 5.21: Time-height plots for the percent difference between CCN concentrations in the uniform base case and scenario 3 for each supersaturation level. Red indicates an increase in CCN relative to the base case while blue indicates a decrease. Isopleths indicate lines of constant percent difference in increments of 5%.

the magnitude of elevated CCN concentrations when compared to scenario 2 results for  $S = 0.6\%$  shown in Figure 5.20. At  $S = 1.0\%$ , we find a slight reduction in CCN concentrations by up to 5% that starts near the surface at  $t \sim 4.5$  h and extends throughout the lower to middle PBL by  $t = 6$  h.

### 5.2.6 Influence of ammonia on aerosol composition and CCN activity

We have shown that the composition of the aerosol population varies considerably with emissions spatial heterogeneity. Specifically, nitrate and ammonium are found to substantially increase as emissions  $SH$  increases. Changes in the relative abundance of these species alters the hygroscopic properties of the aerosol resulting in an increased concentration of CCN at low supersaturations.

Sulfate and nitrate are both anions with charge -2 and -1, respectively, while ammonium is a cation with charge +1. In turn, ammonium plays an important role in neutralizing both sulfate and nitrate. Due

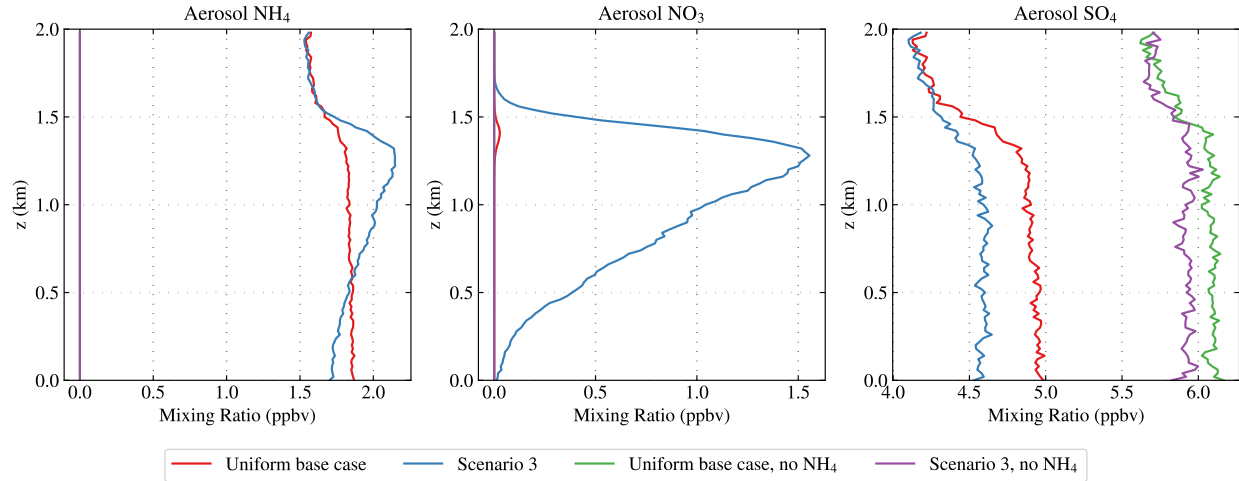


Figure 5.22: Vertical profiles ( $t = 6$  h) for ammonium, nitrate, and sulfate comparing uniform base case and scenario 3 both with and without ammonium.

to the extremely low volatility of  $\text{H}_2\text{SO}_4$ , it rapidly partitions into the aerosol phase where it dissociates into  $\text{SO}_4^{2-}$ . In turn, available ammonium will first neutralize sulfate by forming ammonium sulfate. Any remaining ammonium in excess of what is required to neutralized the sulfate, referred to as free ammonium, will bind to nitrate and thus form ammonium nitrate. Crucially, the abundance of free ammonium determines the concentration of nitrate in the aerosol phase; if no free ammonium is available then no nitrate will enter the aerosol, whereas the presence of free ammonium allows a one-to-one molar ratio of nitrate to ammonium in the form of ammonium nitrate.

Here, we run two additional modified simulations for the uniform base case and scenario 3 in which the concentration of total ammonium ( $\text{NH}_3, \text{gas} + \text{NH}_4, \text{aerosol}$ ) is set to zero. Emissions of  $\text{NH}_3$  are also set to zero to ensure that total ammonium remains zero throughout each simulation. These additional simulations help to isolate the impact of emissions spatial heterogeneity on aerosol composition and CCN activity in the absence of ammonium.

Figure 5.22 shows vertical profiles at  $t = 6$  h for aerosol ammonium, nitrate, and sulfate concentrations in ppbv for four simulation runs: the uniform base case and scenario 3 as shown in previous sections and the same scenarios but without any ammonium present. Simulations with ammonium show that the uniform base case has slightly more ammonium in the lowest 500 m of the PBL, while scenario 3 has higher concentrations in excess of 2 ppbv in the middle to upper PBL. As a consistency check, the same scenarios without ammonium (uniform base case in green, scenario 3 in purple) indicate zero ammonium throughout

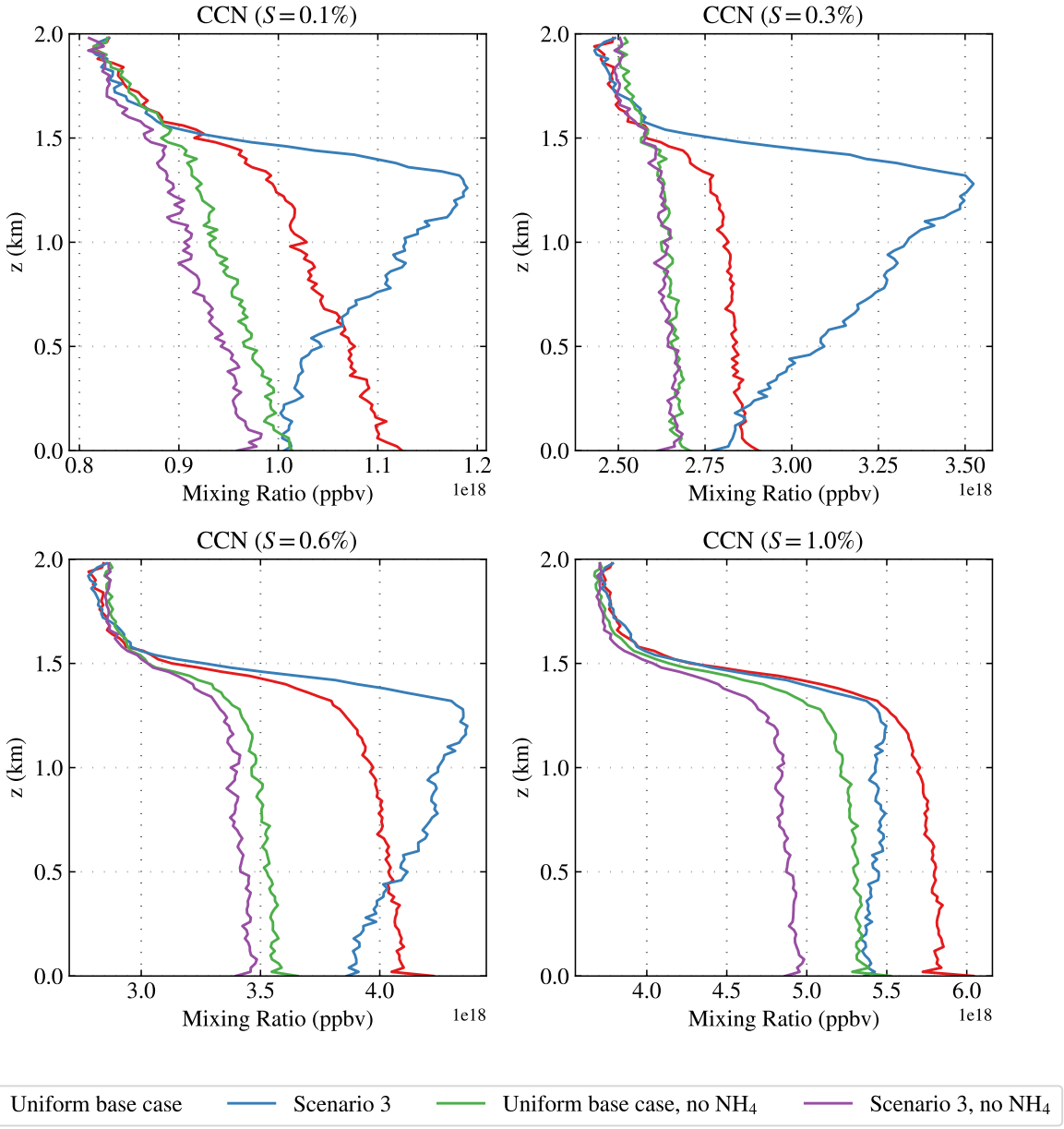


Figure 5.23: Vertical profiles ( $t = 6$  h) for CCN concentrations at supersaturations  $S = 0.1, 0.3, 0.6, 1.0\%$  for the uniform base case and scenario 3 with and without ammonium.

the entire domain. We find that simulations without ammonium contain no nitrate, which is consistent with previous discussion of the availability of free ammonium in order to allow nitrate to enter the aerosol phase. Without ammonium present, sulfate concentrations increase for both the uniform base case (4.9 ppbv to 6.1 ppbv) and scenario 3 (4.6 ppbv to 5.9 ppbv).

note that the CCN mixing ratios are large (1e18) since these are number concentrations.. need to modify

mentions of concentration values! Figure 5.23 shows vertical profiles of CCN concentrations at  $t = 6$  h for

each supersaturation level ( $S = 0.1, 0.3, 0.6, 1.0\%$ ) for both the uniform base case and emissions scenario 3 with and without ammonium. We find that in the absence of ammonium, concentrations of CCN at each supersaturation level agree closely across the uniform base case and scenario 3. For  $S = 0.1\%$ , we find that CCN concentrations in scenario 3 (no ammonium) are a constant factor of 0.02 ppbv less than in the uniform base case (no ammonium). At  $S = 0.3\%$ , CCN concentrations across both scenarios are virtually identical to within random variability. For  $S = 0.6\%$ , the no-ammonium scenario 3 has a relatively constant factor of 0.1 ppbv less CCN than the no-ammonium uniform base case. We find a similar relationship for  $S = 1.0\%$  with a constant factor of 0.5 ppbv fewer CCN in the ammonium-free scenario 3 case.

I think it would be helpful here to include profiles of total number concentration  $\zeta$  50 nm (could also do this elsewhere). My thinking is that coagulation is probably reducing the total number of particles in the high heterogeneity case and this leads to the lower CCN conc. I think this is somewhat counteracted by the increased hygroscopicity of particles in the set of scenarios with ammonium/nitrate present in the aerosol.

### 5.3 Implications

Non-linear coupling between emissions  $SH$  and CCN activity, mediated by the presence of nitrate and contingent on the availability of free ammonium to allow partitioning of nitrate into the aerosol phase.

# Chapter 6

## Conclusions

### 6.1 Study limitations and future work

#### Some rough draft ideas

- In this study, all emissions are released at the ground level. This is a simplification as some emission sources such as stack emissions from industrial sources are emitted at some height above the surface. Because the atmospheric stability often differs between the surface level and the planetary boundary layer, one may expect the shape and structure of the plume to differ if emissions are released directly into the boundary layer. For example, consider a nocturnal boundary layer/surface layer. If the emissions are released directly into the surface layer capped by a strong nocturnal inversion then emissions in the surface layer will be trapped and concentrations will be very high. If emissions are released from a plume above the surface layer, the absence of vertical mixing will lead to large concentration gradients between the region near the emissions plume and the surrounding ambient conditions.
- This thesis investigates the impact of emissions spatial heterogeneity on ccn activity, however one may wish to extend this analysis to include aerosol optical properties which govern their radiative effects.
- Through the use of particle-resolved modeling in a large-eddy simulation framework, this thesis establishes a benchmark for high resolution representation of aerosol processes in the boundary layer. A natural extension would be to conduct simulations with similar setups but instead use coarser-resolved treatments for the aerosols (e.g., modal or sectional representations) as well as the transport and turbulence treatment (e.g., use of Reynolds Averaged Navier Stokes modeling). This would allow intercomparison with the high-resolution results presented in this thesis and quantify structural

uncertainties in desired quantities (such as CCN activity or aerosol optical properties) introduced by the use of coarser-resolved modeling treatments.

- Here we chose spatial and temporal discretization apriori, mainly on the basis of what is feasible given our computational resources. A limitation of this approach is that we are uncertain whether we are adequately resolving all spatial and temporal scales at which gas phase and aerosol chemical reactions occur. Future work should quantitatively determine the necessary spatial and temporal scales for resolving relevant atmospheric chemistry reactions via metrics such as the damkohler number.

# References

- Albrecht, Bruce A. (Sept. 1989). "Aerosols, Cloud Microphysics, and Fractional Cloudiness". In: *Science* 245.4923. Publisher: American Association for the Advancement of Science, pp. 1227–1230. DOI: [10.1126/science.245.4923.1227](https://doi.org/10.1126/science.245.4923.1227).
- Auger, Ludovic and Bernard Legras (Apr. 2007). "Chemical segregation by heterogeneous emissions". en. In: *Atmospheric Environment* 41.11, pp. 2303–2318. DOI: [10.1016/j.atmosenv.2006.11.032](https://doi.org/10.1016/j.atmosenv.2006.11.032).
- Brock, Charles A. et al. (Apr. 2016). "Aerosol optical properties in the southeastern United States in summer &ndash; Part 2: Sensitivity of aerosol optical depth to relative humidity and aerosol parameters". English. In: *Atmospheric Chemistry and Physics* 16.8. Publisher: Copernicus GmbH, pp. 5009–5019. DOI: [10.5194/acp-16-5009-2016](https://doi.org/10.5194/acp-16-5009-2016).
- Bruine, Marco de et al. (Dec. 2019). "Explicit aerosol–cloud interactions in the Dutch Atmospheric Large-Eddy Simulation model DALES4.1-M7". English. In: *Geoscientific Model Development* 12.12. Publisher: Copernicus GmbH, pp. 5177–5196. DOI: [10.5194/gmd-12-5177-2019](https://doi.org/10.5194/gmd-12-5177-2019).
- Cassiani, M. et al. (Jan. 2010). "Stochastic fields method for sub-grid scale emission heterogeneity in mesoscale atmospheric dispersion models". English. In: *Atmospheric Chemistry and Physics* 10.1. Publisher: Copernicus GmbH, pp. 267–277. DOI: [10.5194/acp-10-267-2010](https://doi.org/10.5194/acp-10-267-2010).
- Charlson, R. J. and M. J. Pilat (Dec. 1969). "Climate: The Influence of Aerosols". EN. In: *Journal of Applied Meteorology and Climatology* 8.6. Publisher: American Meteorological Society Section: Journal of Applied Meteorology and Climatology, pp. 1001–1002. DOI: [10.1175/1520-0450\(1969\)008<1001:CTIOA>2.0.CO;2](https://doi.org/10.1175/1520-0450(1969)008<1001:CTIOA>2.0.CO;2).
- Charlson, R. J., S. E. Schwartz, et al. (1992). "Climate Forcing by Anthropogenic Aerosols". In: *Science* 255.5043. Publisher: American Association for the Advancement of Science, pp. 423–430.
- Ching, Joseph et al. (2016). "A three-dimensional sectional representation of aerosol mixing state for simulating optical properties and cloud condensation nuclei". en. In: *Journal of Geophysical Research: Atmospheres* 121.10. \_eprint: <https://onlinelibrary.wiley.com/doi/pdf/10.1002/2015JD024323>, pp. 5912–5929. DOI: [10.1002/2015JD024323](https://doi.org/10.1002/2015JD024323).

- Cooper, Scott D. et al. (Mar. 1997). “Quantifying Spatial Heterogeneity in Streams”. In: *Journal of the North American Benthological Society* 16.1. Publisher: The University of Chicago Press, pp. 174–188. DOI: [10.2307/1468250](https://doi.org/10.2307/1468250).
- Crippa, Paola et al. (Jan. 2017). “The impact of resolution on meteorological, chemical and aerosol properties in regional simulations with WRF-Chem”. English. In: *Atmospheric Chemistry and Physics* 17.2. Publisher: Copernicus GmbH, pp. 1511–1528. DOI: [10.5194/acp-17-1511-2017](https://doi.org/10.5194/acp-17-1511-2017).
- Curtis, Jeffrey H., Nicole Riemer, and Matthew West (Nov. 2017). “A single-column particle-resolved model for simulating the vertical distribution of aerosol mixing state: WRF-PartMC-MOSAIC-SCM v1.0”. English. In: *Geoscientific Model Development* 10.11. Publisher: Copernicus GmbH, pp. 4057–4079. DOI: [10.5194/gmd-10-4057-2017](https://doi.org/10.5194/gmd-10-4057-2017).
- Damköhler, Gerhard (Apr. 1947). “The Effect of Turbulence on the Flame Velocity in Gas Mixtures”. en. In: *Zeitschrift fuer Elektrochemie und Angewandte Physikalische Chemie* 46.11. Number: NACA-TM-1112.
- Danckwerts, P. V. (July 1952). “The definition and measurement of some characteristics of mixtures”. en. In: *Applied Scientific Research, Section A* 3.4, pp. 279–296. DOI: [10.1007/BF03184936](https://doi.org/10.1007/BF03184936).
- Deardorff, James W. (Apr. 1970). “A numerical study of three-dimensional turbulent channel flow at large Reynolds numbers”. en. In: *Journal of Fluid Mechanics* 41.2, pp. 453–480. DOI: [10.1017/S0022112070000691](https://doi.org/10.1017/S0022112070000691).
- (June 1980). “Stratocumulus-capped mixed layers derived from a three-dimensional model”. In: *Boundary-Layer Meteorology* 18.4, pp. 495–527. DOI: [10.1007/BF00119502](https://doi.org/10.1007/BF00119502).
- Dlugi, R. et al. (Sept. 2014). “The balances of mixing ratios and segregation intensity: a case study from the field (ECHO 2003)”. English. In: *Atmospheric Chemistry and Physics* 14.18. Publisher: Copernicus GmbH, pp. 10333–10362. DOI: [10.5194/acp-14-10333-2014](https://doi.org/10.5194/acp-14-10333-2014).
- Dong, Pinliang (June 2000). “Lacunarity for Spatial Heterogeneity Measurement in GIS”. In: *Geographic Information Sciences* 6.1. Publisher: Taylor & Francis \_eprint: <https://doi.org/10.1080/1082400009480530>, pp. 20–26. DOI: [10.1080/1082400009480530](https://doi.org/10.1080/1082400009480530).
- Fan, Jiwen et al. (Nov. 2016). “Review of Aerosol–Cloud Interactions: Mechanisms, Significance, and Challenges”. EN. In: *Journal of the Atmospheric Sciences* 73.11. Publisher: American Meteorological Society Section: Journal of the Atmospheric Sciences, pp. 4221–4252. DOI: [10.1175/JAS-D-16-0037.1](https://doi.org/10.1175/JAS-D-16-0037.1).

- Fast, Jerome D., David M. Bell, et al. (Sept. 2022). “Using aircraft measurements to characterize subgrid-scale variability of aerosol properties near the Atmospheric Radiation Measurement Southern Great Plains site”. English. In: *Atmospheric Chemistry and Physics* 22.17. Publisher: Copernicus GmbH, pp. 11217–11238. DOI: [10.5194/acp-22-11217-2022](https://doi.org/10.5194/acp-22-11217-2022).
- Fast, Jerome D., Larry K. Berg, et al. (2019). “The Impact of Variable Land-Atmosphere Coupling on Convective Cloud Populations Observed During the 2016 HI-SCALE Field Campaign”. en. In: *Journal of Advances in Modeling Earth Systems* 11.8. \_eprint: <https://onlinelibrary.wiley.com/doi/pdf/10.1029/2019MS001727>, pp. 2629–2654. DOI: [10.1029/2019MS001727](https://doi.org/10.1029/2019MS001727).
- Fierce, Laura et al. (Sept. 2024). “Quantifying structural errors in cloud condensation nuclei activity from reduced representation of aerosol size distributions”. In: *Journal of Aerosol Science* 181, p. 106388. DOI: [10.1016/j.jaerosci.2024.106388](https://doi.org/10.1016/j.jaerosci.2024.106388).
- Forster, P. et al. (2021). “The Earth’s Energy Budget, Climate Feedbacks, and Climate Sensitivity”. In: *Climate Change 2021: The Physical Science Basis. Contribution of Working Group I to the Sixth Assessment Report of the Intergovernmental Panel on Climate Change*. Ed. by V. Masson-Delmotte et al. Cambridge, United Kingdom and New York, NY, USA: Cambridge University Press, pp. 923–1054. DOI: [10.1017/9781009157896.009](https://doi.org/10.1017/9781009157896.009).
- Galmarini, S., J.-F. Vinuesa, and A. Martilli (Jan. 2008). “Modeling the impact of sub-grid scale emission variability on upper-air concentration”. English. In: *Atmospheric Chemistry and Physics* 8.2. Publisher: Copernicus GmbH, pp. 141–158. DOI: [10.5194/acp-8-141-2008](https://doi.org/10.5194/acp-8-141-2008).
- Gillespie, Daniel T. (Oct. 1975). “An Exact Method for Numerically Simulating the Stochastic Coalescence Process in a Cloud”. EN. In: *Journal of the Atmospheric Sciences* 32.10. Publisher: American Meteorological Society Section: Journal of the Atmospheric Sciences, pp. 1977–1989. DOI: [10.1175/1520-0469\(1975\)032<1977:AEMFNS>2.0.CO;2](https://doi.org/10.1175/1520-0469(1975)032<1977:AEMFNS>2.0.CO;2).
- Gustafson Jr., William I., Yun Qian, and Jerome D. Fast (2011). “Downscaling aerosols and the impact of neglected subgrid processes on direct aerosol radiative forcing for a representative global climate model grid spacing”. en. In: *Journal of Geophysical Research: Atmospheres* 116.D13. \_eprint: <https://onlinelibrary.wiley.com/doi/pdf/10.1029/2010JD015480>. DOI: [10.1029/2010JD015480](https://doi.org/10.1029/2010JD015480).
- Karamchandani, Prakash, Krish Vijayaraghavan, and Greg Yarwood (Sept. 2011). “Sub-Grid Scale Plume Modeling”. en. In: *Atmosphere* 2.3. Number: 3 Publisher: Molecular Diversity Preservation International, pp. 389–406. DOI: [10.3390/atmos2030389](https://doi.org/10.3390/atmos2030389).

- Kim, S.-W., M. C. Barth, and M. Trainer (2016). “Impact of turbulent mixing on isoprene chemistry”. en. In: *Geophysical Research Letters* 43.14. \_eprint: <https://onlinelibrary.wiley.com/doi/pdf/10.1002/2016GL069752>, pp. 7701–7708. DOI: [10.1002/2016GL069752](https://doi.org/10.1002/2016GL069752).
- Köhler, Hilding (Jan. 1936). “The nucleus in and the growth of hygroscopic droplets”. en. In: *Transactions of the Faraday Society* 32.0. Publisher: The Royal Society of Chemistry, pp. 1152–1161. DOI: [10.1039/TF9363201152](https://doi.org/10.1039/TF9363201152).
- Kolmogorov, A. N. (1991). “The Local Structure of Turbulence in Incompressible Viscous Fluid for Very Large Reynolds Numbers”. In: *Proceedings: Mathematical and Physical Sciences* 434.1890. Publisher: Royal Society, pp. 9–13.
- Kotamarthi, V Rao and Yan Feng (2017). *LES and Atmospheric Chemistry/Aerosol Modeling?* en. Tysons, Virginia.
- Krol, Maarten C., M. Jeroen Molemaker, and Jordi Vilà Guerau de Arellano (2000). “Effects of turbulence and heterogeneous emissions on photochemically active species in the convective boundary layer”. en. In: *Journal of Geophysical Research: Atmospheres* 105.D5. \_eprint: <https://onlinelibrary.wiley.com/doi/pdf/10.1029/1999JD900958>, pp. 6871–6884. DOI: [10.1029/1999JD900958](https://doi.org/10.1029/1999JD900958).
- Lau, K.-M. and K.-M. Kim (2006). “Observational relationships between aerosol and Asian monsoon rainfall, and circulation”. en. In: *Geophysical Research Letters* 33.21. \_eprint: <https://onlinelibrary.wiley.com/doi/pdf/10.1029/2006GL027546>. DOI: [10.1029/2006GL027546](https://doi.org/10.1029/2006GL027546).
- Lee, Jungmin M., Yunyan Zhang, and Stephen A. Klein (Feb. 2019). “The Effect of Land Surface Heterogeneity and Background Wind on Shallow Cumulus Clouds and the Transition to Deeper Convection”. EN. In: *Journal of the Atmospheric Sciences* 76.2. Publisher: American Meteorological Society Section: Journal of the Atmospheric Sciences, pp. 401–419. DOI: [10.1175/JAS-D-18-0196.1](https://doi.org/10.1175/JAS-D-18-0196.1).
- Li, Cathy W. Y. et al. (Jan. 2021). “Error induced by neglecting subgrid chemical segregation due to inefficient turbulent mixing in regional chemical-transport models in urban environments”. English. In: *Atmospheric Chemistry and Physics* 21.1. Publisher: Copernicus GmbH, pp. 483–503. DOI: [10.5194/acp-21-483-2021](https://doi.org/10.5194/acp-21-483-2021).
- Li, Jing et al. (June 2022). “Scattering and absorbing aerosols in the climate system”. en. In: *Nature Reviews Earth & Environment* 3.6. Publisher: Nature Publishing Group, pp. 363–379. DOI: [10.1038/s43017-022-00296-7](https://doi.org/10.1038/s43017-022-00296-7).

- Lin, Guangxing et al. (2017). “Quantification of marine aerosol subgrid variability and its correlation with clouds based on high-resolution regional modeling”. en. In: *Journal of Geophysical Research: Atmospheres* 122.12. \_eprint: <https://onlinelibrary.wiley.com/doi/pdf/10.1002/2017JD026567>, pp. 6329–6346. DOI: [10.1002/2017JD026567](https://doi.org/10.1002/2017JD026567).
- Loke, Lynette H. L. and Ryan A. Chisholm (2022). “Measuring habitat complexity and spatial heterogeneity in ecology”. en. In: *Ecology Letters* 25.10. \_eprint: <https://onlinelibrary.wiley.com/doi/pdf/10.1111/ele.14084>, pp. 2269–2288. DOI: [10.1111/ele.14084](https://doi.org/10.1111/ele.14084).
- Mandelbrot, Benoit (1967). “How Long Is the Coast of Britain? Statistical Self-Similarity and Fractional Dimension”. In: *Science* 156.3775. Publisher: American Association for the Advancement of Science, pp. 636–638.
- Mandelbrot, Benoit B. (1983). *The fractal geometry of nature*. eng. Updated and augmented. New York: W.H. Freeman.
- Mann, G. W. et al. (May 2012). “Intercomparison of modal and sectional aerosol microphysics representations within the same 3-D global chemical transport model”. English. In: *Atmospheric Chemistry and Physics* 12.10. Publisher: Copernicus GmbH, pp. 4449–4476. DOI: [10.5194/acp-12-4449-2012](https://doi.org/10.5194/acp-12-4449-2012).
- Molemaker, M. Jeroen and Jordi Vilà-Guerau de Arellano (Feb. 1998). “Control of Chemical Reactions by Convective Turbulence in the Boundary Layer”. EN. In: *Journal of the Atmospheric Sciences* 55.4. Publisher: American Meteorological Society Section: Journal of the Atmospheric Sciences, pp. 568–579. DOI: [10.1175/1520-0469\(1998\)055<0568:COCRBC>2.0.CO;2](https://doi.org/10.1175/1520-0469(1998)055<0568:COCRBC>2.0.CO;2).
- Ouwersloot, H. G. et al. (Oct. 2011). “On the segregation of chemical species in a clear boundary layer over heterogeneous land surfaces”. English. In: *Atmospheric Chemistry and Physics* 11.20. Publisher: Copernicus GmbH, pp. 10681–10704. DOI: [10.5194/acp-11-10681-2011](https://doi.org/10.5194/acp-11-10681-2011).
- Petters, M. D. and S. M. Kreidenweis (Apr. 2007). “A single parameter representation of hygroscopic growth and cloud condensation nucleus activity”. English. In: *Atmospheric Chemistry and Physics* 7.8. Publisher: Copernicus GmbH, pp. 1961–1971. DOI: [10.5194/acp-7-1961-2007](https://doi.org/10.5194/acp-7-1961-2007).
- Pierce, J. R. et al. (May 2009). “Parameterization of the effect of sub-grid scale aerosol dynamics on aerosol number emission rates”. In: *Journal of Aerosol Science* 40.5, pp. 385–393. DOI: [10.1016/j.jaerosci.2008.11.009](https://doi.org/10.1016/j.jaerosci.2008.11.009).

- Plexida, Sofia G. et al. (Feb. 2014). “Selecting landscape metrics as indicators of spatial heterogeneity—A comparison among Greek landscapes”. In: *International Journal of Applied Earth Observation and Geoinformation* 26, pp. 26–35. DOI: [10.1016/j.jag.2013.05.001](https://doi.org/10.1016/j.jag.2013.05.001).
- Pugh, T. a. M. et al. (May 2011). “The influence of small-scale variations in isoprene concentrations on atmospheric chemistry over a tropical rainforest”. English. In: *Atmospheric Chemistry and Physics* 11.9. Publisher: Copernicus GmbH, pp. 4121–4134. DOI: [10.5194/acp-11-4121-2011](https://doi.org/10.5194/acp-11-4121-2011).
- Qian, Y., W. I. Jr Gustafson, and J. D. Fast (July 2010). “An investigation of the sub-grid variability of trace gases and aerosols for global climate modeling”. English. In: *Atmospheric Chemistry and Physics* 10.14. Publisher: Copernicus GmbH, pp. 6917–6946. DOI: [10.5194/acp-10-6917-2010](https://doi.org/10.5194/acp-10-6917-2010).
- Ramnarine, Emily et al. (May 2019). “Effects of near-source coagulation of biomass burning aerosols on global predictions of aerosol size distributions and implications for aerosol radiative effects”. English. In: *Atmospheric Chemistry and Physics* 19.9, pp. 6561–6577. DOI: [10.5194/acp-19-6561-2019](https://doi.org/10.5194/acp-19-6561-2019).
- Riemer, N., A. P. Ault, et al. (2019). “Aerosol Mixing State: Measurements, Modeling, and Impacts”. en. In: *Reviews of Geophysics* 57.2. \_eprint: <https://onlinelibrary.wiley.com/doi/pdf/10.1029/2018RG000615>, pp. 187–249. DOI: [10.1029/2018RG000615](https://doi.org/10.1029/2018RG000615).
- Riemer, N. and M. West (Nov. 2013). “Quantifying aerosol mixing state with entropy and diversity measures”. English. In: *Atmospheric Chemistry and Physics* 13.22. Publisher: Copernicus GmbH, pp. 11423–11439. DOI: [10.5194/acp-13-11423-2013](https://doi.org/10.5194/acp-13-11423-2013).
- Riemer, N., M. West, et al. (2009). “Simulating the evolution of soot mixing state with a particle-resolved aerosol model”. en. In: *Journal of Geophysical Research: Atmospheres* 114.D9. \_eprint: <https://onlinelibrary.wiley.com/doi/10.1029/2008JD011073>. DOI: [10.1029/2008JD011073](https://doi.org/10.1029/2008JD011073).
- Sakamoto, Kimiko M. et al. (June 2016). “The evolution of biomass-burning aerosol size distributions due to coagulation: dependence on fire and meteorological details and parameterization”. English. In: *Atmospheric Chemistry and Physics* 16.12. Publisher: Copernicus GmbH, pp. 7709–7724. DOI: [10.5194/acp-16-7709-2016](https://doi.org/10.5194/acp-16-7709-2016).
- Schumann, Ulrich (Jan. 1989). “Large-eddy simulation of turbulent diffusion with chemical reactions in the convective boundary layer”. en. In: *Atmospheric Environment* (1967) 23.8, pp. 1713–1727. DOI: [10.1016/0004-6981\(89\)90056-5](https://doi.org/10.1016/0004-6981(89)90056-5).
- Seinfeld, J and S Pandis (1998). *Atmospheric Chemistry and Physics: From Air Pollution to Climate Change*.

- Shu, Hua et al. (July 2019). "Quantifying the spatial heterogeneity of points". In: *International Journal of Geographical Information Science* 33.7. Publisher: Taylor & Francis .eprint: <https://doi.org/10.1080/13658816.2019.1577432>, pp. 1355–1376. DOI: [10.1080/13658816.2019.1577432](https://doi.org/10.1080/13658816.2019.1577432).
- Skamarock, C. et al. (2008). "A Description of the Advanced Research WRF Version 3". en. In: DOI: [10.5065/D68S4MVH](https://doi.org/10.5065/D68S4MVH).
- Smagorinsky, J. (Mar. 1963). "GENERAL CIRCULATION EXPERIMENTS WITH THE PRIMITIVE EQUATIONS: I. THE BASIC EXPERIMENT". EN. In: *Monthly Weather Review* 91.3. Publisher: American Meteorological Society Section: Monthly Weather Review, pp. 99–164. DOI: [10.1175/1520-0493\(1963\)091<0099:GCEWTP>2.3.CO;2](https://doi.org/10.1175/1520-0493(1963)091<0099:GCEWTP>2.3.CO;2).
- Stoll, Rob et al. (Dec. 2020). "Large-Eddy Simulation of the Atmospheric Boundary Layer". en. In: *Boundary-Layer Meteorology* 177.2, pp. 541–581. DOI: [10.1007/s10546-020-00556-3](https://doi.org/10.1007/s10546-020-00556-3).
- Sykes, R. I., D. S. Henn, et al. (Oct. 1992). "Large-eddy simulation of a turbulent reacting plume". en. In: *Atmospheric Environment. Part A. General Topics* 26.14, pp. 2565–2574. DOI: [10.1016/0960-1686\(92\)90109-X](https://doi.org/10.1016/0960-1686(92)90109-X).
- Sykes, R. I., S. F. Parker, et al. (July 1994). "Turbulent Mixing with Chemical Reaction in the Planetary Boundary Layer". EN. In: *Journal of Applied Meteorology and Climatology* 33.7. Publisher: American Meteorological Society Section: Journal of Applied Meteorology and Climatology, pp. 825–834. DOI: [10.1175/1520-0450\(1994\)033<0825:TMWCRI>2.0.CO;2](https://doi.org/10.1175/1520-0450(1994)033<0825:TMWCRI>2.0.CO;2).
- Thiffeault, Jean-Luc (Jan. 2012). "Using multiscale norms to quantify mixing and transport". en. In: *Nonlinearity* 25.2, R1. DOI: [10.1088/0951-7715/25/2/R1](https://doi.org/10.1088/0951-7715/25/2/R1).
- Tian, Jingjing et al. (2022). "How Does Land Cover and Its Heterogeneity Length Scales Affect the Formation of Summertime Shallow Cumulus Clouds in Observations From the US Southern Great Plains?" en. In: *Geophysical Research Letters* 49.7. .eprint: <https://onlinelibrary.wiley.com/doi/pdf/10.1029/2021GL097070>, e2021GL097070. DOI: [10.1029/2021GL097070](https://doi.org/10.1029/2021GL097070).
- Tonttila, Juha et al. (Jan. 2017). "UCLALES-SALSA v1.0: a large-eddy model with interactive sectional microphysics for aerosol, clouds and precipitation". English. In: *Geoscientific Model Development* 10.1. Publisher: Copernicus GmbH, pp. 169–188. DOI: [10.5194/gmd-10-169-2017](https://doi.org/10.5194/gmd-10-169-2017).
- Twomey, S. (July 1977). "The Influence of Pollution on the Shortwave Albedo of Clouds". EN. In: *Journal of the Atmospheric Sciences* 34.7. Publisher: American Meteorological Society Section: Journal of the

Atmospheric Sciences, pp. 1149–1152. DOI: [10.1175/1520-0469\(1977\)034<1149:TIOPOT>2.0.CO;2](https://doi.org/10.1175/1520-0469(1977)034<1149:TIOPOT>2.0.CO;2).

Vinuesa, Jean-François and Jordi Vilá-Guerau De Arellano (Dec. 2003). “Fluxes and (co-)variances of reacting scalars in the convective boundary layer”. In: *Tellus B: Chemical and Physical Meteorology* 55.4. Publisher: Taylor & Francis .eprint: <https://doi.org/10.3402/tellusb.v55i4.16382>, pp. 935–949. DOI: [10.3402/tellusb.v55i4.16382](https://doi.org/10.3402/tellusb.v55i4.16382).

Wang, Yuting, Guy P. Brasseur, and Tao Wang (Feb. 2022). “Segregation of Atmospheric Oxidants in Turbulent Urban Environments”. en. In: *Atmosphere* 13.2. Number: 2 Publisher: Multidisciplinary Digital Publishing Institute, p. 315. DOI: [10.3390/atmos13020315](https://doi.org/10.3390/atmos13020315).

Wang, Yuting, Yong-Feng Ma, Domingo Muñoz-Esparza, Jianing Dai, et al. (May 2023). “Coupled mesoscale–microscale modeling of air quality in a polluted city using WRF-LES-Chem”. English. In: *Atmospheric Chemistry and Physics* 23.10. Publisher: Copernicus GmbH, pp. 5905–5927. DOI: [10.5194/acp-23-5905-2023](https://doi.org/10.5194/acp-23-5905-2023).

Wang, Yuting, Yong-Feng Ma, Domingo Muñoz-Esparza, Cathy W. Y. Li, et al. (Mar. 2021). “The impact of inhomogeneous emissions and topography on ozone photochemistry in the vicinity of Hong Kong Island”. English. In: *Atmospheric Chemistry and Physics* 21.5. Publisher: Copernicus GmbH, pp. 3531–3553. DOI: [10.5194/acp-21-3531-2021](https://doi.org/10.5194/acp-21-3531-2021).

Weigum, Natalie, Nick Schutgens, and Philip Stier (Nov. 2016). “Effect of aerosol subgrid variability on aerosol optical depth and cloud condensation nuclei: implications for global aerosol modelling”. English. In: *Atmospheric Chemistry and Physics* 16.21. Publisher: Copernicus GmbH, pp. 13619–13639. DOI: [10.5194/acp-16-13619-2016](https://doi.org/10.5194/acp-16-13619-2016).

Zaveri, Rahul A., James C. Barnard, et al. (2010). “Particle-resolved simulation of aerosol size, composition, mixing state, and the associated optical and cloud condensation nuclei activation properties in an evolving urban plume”. en. In: *Journal of Geophysical Research: Atmospheres* 115.D17. .eprint: <https://onlinelibrary.wiley.com/doi/pdf/10.1029/2009JD013616>. DOI: [10.1029/2009JD013616](https://doi.org/10.1029/2009JD013616).

Zaveri, Rahul A., Richard C. Easter, et al. (2008). “Model for Simulating Aerosol Interactions and Chemistry (MOSAIC)”. en. In: *Journal of Geophysical Research: Atmospheres* 113.D13. .eprint: <https://onlinelibrary.wiley.com/doi/10.1029/2007JD008782>. DOI: [10.1029/2007JD008782](https://doi.org/10.1029/2007JD008782).

Zaveri, Rahul A. and Leonard K. Peters (1999). “A new lumped structure photochemical mechanism for large-scale applications”. en. In: *Journal of Geophysical Research: Atmospheres* 104.D23. .eprint:

<https://onlinelibrary.wiley.com/doi/pdf/10.1029/1999JD900876>, pp. 30387–30415. DOI: [10 . 1029 / 1999JD900876](https://doi.org/10.1029/1999JD900876).

Zhong, Jian, Xiao-Ming Cai, and William James Bloss (May 2015). “Modelling the dispersion and transport of reactive pollutants in a deep urban street canyon: Using large-eddy simulation”. en. In: *Environmental Pollution* 200, pp. 42–52. DOI: [10 . 1016 / j . envpol . 2015 . 02 . 009](https://doi.org/10.1016/j.envpol.2015.02.009).

— (May 2017). “Large eddy simulation of reactive pollutants in a deep urban street canyon: Coupling dynamics with O<sub>3</sub>-NO<sub>x</sub>-VOC chemistry”. en. In: *Environmental Pollution* 224, pp. 171–184. DOI: [10 . 1016 / j . envpol . 2017 . 01 . 076](https://doi.org/10.1016/j.envpol.2017.01.076).

Zhu, Yifang et al. (Sept. 2002). “Study of ultrafine particles near a major highway with heavy-duty diesel traffic”. In: *Atmospheric Environment* 36.27, pp. 4323–4335. DOI: [10 . 1016 / S1352-2310 \(02\) 00354-0](https://doi.org/10.1016/S1352-2310(02)00354-0).